Development of Surface Plasmon Resonance Instrument for Sensing and Other Applications

THESIS

Submitted in partial fulfillment

of the requirement for the degree of

Doctor of Philosophy

by

Ashutosh Joshi

Under the supervision of

Prof. Raj Kumar Gupta

BIRLA INSTITUTE OF TECHNOLOGY AND SCIENCE - PILANI

2023

BIRLA INSTITUTE OF TECHNOLOGY AND SCIENCE - PILANI

Certificate

This is to certify that the thesis entitled,

"*Development of Surface Plasmon Resonance Instrument for Sensing and Other Applications*"

submitted by Ashutosh Joshi ID No. 2017PHXF0035P for award of Ph.D. Degree of the Institute, embodies original work done by him under my supervision.

Supervisor

Prof. Raj Kumar Gupta

BITS Pilani, Pilani Campus

Date: 20 June 2023

Abstract

Sensors are ubiquitous in most of the technological devices. The field of medical diagnostics and point-of-care devices relies on efficient biosensors and bio-analysis devices. There is an enormous amount of research and development in these fields. An optical phenomenon like surface plasmon resonance (SPR) offers a label-free measurement with very high sensitivity and resolution. Essentially using the SPR technology, a minuscule change in refractive index (RI) due to molecular interaction is measured with great accuracy. These characteristics have made the SPR phenomenon very popular and promising in the development of a variety of sensors, including bio-sensors, chemical sensors, and gas sensors.

The commercially available SPR instruments are sensitive, but they are very costly and limited, with a small angular scan range, very high maintenance cost, high-end local infrastructure, complex operation, and analysis. We developed a low-cost, sensitive, and portable instrument with support from DST India. A laboratory prototype was developed by our group in the first phase of the project (2010-2013). Later, with support from DST, India (2017-2019), we developed the equipment ready for commercialization. A multidimensional improvement in hardware and software was incorporated such that it can be transported anywhere in India and abroad for user-friendly SPR-related applications. The instrument was demonstrated before the Scientific Committee of DST-India at IIT-Delhi in 2018. Then as a part of the validation, we transported the equipment to Bangalore via a courier. The equipment was installed in a local reading table of a laboratory at Raman Research Institute, and a set of experiments were performed. We obtained a satisfactory report from the scientists from RRI and some other places. A website (www.sprsensors.org) is designed to share the latest version of our equipment in the scientific arena.

The instrument was built by adopting a novel optomechanical scanning system. The instrument is capable of both modes of operation, e.g., static and dynamic. It is completely computer controlled with minimal experimental alteration from the user's side. We have developed a robust & user-friendly hardware control, data acquisition, and post-experiment data analysis software using the software programs viz. LabVIEW (for control and data acquisition) and

MATLAB (for analysis). The development of the SPR system was used in various traditional sensing applications and some non-traditional applications like measurement of the refractive index of ultrathin films, modulation of SPR responses due to perturbation induced by external electromagnetic waves in organic molecules, and optical switching in liquid crystal molecules.

The sensing of the organic volatile solvents, e.g., acetone and ethanol, was demonstrated with the self-assembled nanoribbons of triphenylene-based discotic liquid crystal (TP) molecules. The π-electrons of the TP molecules facilitate the π-stacking interaction of the molecules leading to the formation of one-dimensional nanowires. The lateral cohesive force causes the nanowires to assemble into nanoribbons. flat nanoribbons undergo a morphological transformation due to the incorporation of silver nanoparticles (SNP) into the matrix of TP molecules. The SNP induces a chiral twisting of the nanoribbons, and therefore, flat nanoribbons transform into a helical nanoribbon structure. The global chiral structure exhibited by the composition of achiral constituents is due to the creation of topological defects like disclination and dislocation. These defects can lead to geometrical frustration in the nanoribbons, which relaxes with the formation of twisted helical nanoribbons. A minor change in the morphology of the supramolecular assembly can have a remarkable effect on the physicochemical properties of the nanoribbons. Our research using the developed SPR sensing system indicates that even a minor change in the geometry of aliphatic chains on the surface of nanoribbons can be employed for sensing organic solvents such as acetone and ethanol. The sensing of the organic solvents due to twisted helical nanoribbons was much better compared to flat nanoribbons.

Further research deals with the fabrication of a susceptible layered structure of organic liquid crystal molecules (4-octyl-4-biphenylcarbonitrile (8CB)). The effect of polarization of the external electromagnetic (EM) wave on the SPR response from the layered structure was observed. The layered structure was formed by depositing a self-assembled monolayer (SAM) of mercaptoundecanoic acid (MUA) followed by a single layer of Langmuir-Schaefer (LS) film of 8CB molecules. The SAM of MUA was found to be non-responsive in the change in resonance angle (RA) due to the change in polarization of the external EM wave. However, it provides a soft-surface platform for the monolayer of 8CB molecules, which gets perturbed locally due to the incidence of the external EM wave. Henceforth, an oscillatory modulation

of the change in RA was observed from the layered structure (Gold/MUA/8CB) due to the change in the polarization angle of the external EM wave with respect to the plane of incidence. The morphological studies during and after the deposition were also performed using FESEM and AFM.

A photoactive ultrathin film of novel H-shaped liquid crystal molecules (HLC) showed a potential for good optical switching under the influence of ultraviolet (UV) EM radiation as monitored using our SPR system. The synthesized HLC molecules consist of azo-groups and nitro-groups. The azo-group can be isomerized (trans-cis transformation) by irradiating them with ultraviolet (UV) light, while the nitro-group provides sufficient amphiphilicity to the HLC to form a stable Langmuir monolayer (LM) at the air-water interface. A single layer of Langmuir-Blodgett (LB) film of HLC was deposited on the SPR chip. The azo-groups of the HLC molecules in the LB film were excited by UV irradiation which leads to morphological changes due to trans-cis transformation. Such morphological change can lead to a minuscule change in the RI of the LB film, which was measured using the developed SPR instrument. The systematic changes in the RA of the LB film of HLC were observed as a function of the intensity of the UV irradiation. The switch-on and switch-off intensity were also measured, which may suggest their applications in optical switches or waveguides.

This thesis discusses the development of an efficient, low-cost, yet sensitive SPR device for traditional sensing applications and some non-traditional measurements. The developed instrument is capable of almost all types of sensing applications, including bio-analysis. There is an enormous future scope in the field. Among the various important developments, some of the advanced modifications of the instrument were attempted by us. The future scope of the equipment in terms of its development, viz. electrochemical SPR (ESPR), SPR imaging through Fluorescence (SPRIF), and a NanoSPR (miniaturized standalone system), are discussed.

Acknowledgements

It gives me immense pleasure in presenting my work in the form of this thesis.

I would like to express my sincere gratitude to Prof. Raj Kumar Gupta for his kind supervision with such precious research work in my thesis till its successful completion. It was an extreme pleasure to get an opportunity to work with such an impactable idea as my research work objective for my thesis. His close supervision provides me a great support for new innovations.

I sincerely acknowledge the crucial guidance of my Doctoral Advisory Committee members Prof. Karunesh K. Gupta (Associate Professor, Department of Electrical & Electronics Engineering, BITS-Pilani, Pilani) and Prof. V. Manjuladevi (Professor and Convener - Departmental Research Committee, Department of Physics, BITS-Pilani, Pilani) for providing invaluable and constructive assistance during this research work and for reviewing the research work. I am extremely grateful to Prof. Anshuman Dalvi (Ex-HOD, Physics) for his direct and indirect support in my research. I am also thankful to Prof. Rakesh Chaubisa (HOD, Physics) for his valuable support. I express thanks to all the faculty members of the department for their valuable support.

Sincerely, I acknowledge Prof. Souvik Bhattacharyya (Vice Chancellor) and Prof. Sudhirkumar Barai (Director) for providing me with a valuable opportunity to execute such supreme research work at BITS-Pilani. I am also thankful to Prof. M.B Srinivas (Dean) and Prof. Shamik Chakraborty (Associate Dean), Academic Graduate Studies and Research Division, BITS Pilani, for the administrative and official support. I also thank the department of science and technology, India (DST-India, Project # IDP/SEN/06/2015), for supporting my fellowship and funding the research work.

An earnest sense of gratitude is extended to Dr. Jamil Akhatar (Ex.- Scientist, CEERI-Pilani), Prof. Ajay Agarwal (IIT-Jodhpur), and Prof. Somaditya Sen (Associate Professor, IIT-Indore).

Although my BITS family is not limited to only a few members, some of them support me at every moment, regardless of the time. I would like to express my special thanks to Ms.

Punam Tiwary, Mr. Sandip Ruidas, Mr. Abhishek Gautam, Ms. Kanchan Gautam, and Mr. Om Prakash Saini.

A few words can't be enough for the support from the family members. I am incredibly grateful to my parents (Dr. Shyam Sundar Joshi & Manorama Joshi), who supported me unconditionally at each and every step of my life. Thank you for blessing and teaching me everything to explore the best in my life.

I extend my acknowledgment to Dr. Keerti Choudhary, Dr. Monika Poonia, Dr. Parul Taneja, Mr. Shivaraja SJ, Ms. Shweta Mishra, Mr. Amrit Kumar, Mr. Akash Gayakwad, Mr. Mudit Sahai, Ms. Preeti, Mr. Samarth, and Ms. Ms. Parsoon (Teammates from Surface Science Laboratory and Liquid Crystal Laboratory) and other research scholars of BITS Pilani. I am thankful to the office staff (Mr. Shrikant Sharma, Mr. Rajiv Gaur, Mr. Kundan Singh, and Mr. Tarun Kumar Sharma) of the physics department for their kind support.

Thanks to the following people for their quick and kind support every time needed: Mr. Bheem Singh and Mr. Om Prakash Saini (Mechanical workshop), Mr. Suresh Saini, Ms. Pushpa Saini, and Mr. Nandlal Saini (Department of chemistry), Mr. Tarachand Saini, Mr. Navin Kumar Rana (Department of pharmacy), Mr. Vijendra, Mr. Rajendra, Mr. Sudhanand, Mr. Rajpal (BITS-Security staff) and BITS-Institute canteen staff.

- Ashutosh Joshi

Contents

List of Figures

List of Tables

Abbreviations

8CB	4-octyl-4-biphenylcarbonitrile
A/W	Air water interface
AFM	Atomic force microscopy
AIS	Angular Interrogation SPR
BAM	Brewster angle microscopy
CCD	Charge Coupled Device
DAQ	Data Acquisition
DLC	Discotic Liquid Crystal
EM	Electromagnetic
ESPR	Electrochemical SPR
FDTD	Finite Difference Time Domain
FESEM	Field emission scanning electron microscopy
FWHM	Full Width Half Minima
GUI	Graphical User Interface
HLC	H-type Liquid Crystal Molecule
HPB	Hydrophobic
HPL	Hydrophilic
IA	Incidence Angle
IDE	Interdigitated Electrode
KR	Kretschmann-Reather
LDR	Light Dependent Resistance
LOD	Limit of Detection

LS	Langmuir-Schaefer
MAX	Maximum signal
MIN	Minimum signal
MUA	Mercaptoundecanoic acid
NR	Normalized Response
OM	Optical Microscopy
PMMA	Polymethyl Methacrylate
QPD	Quadrant Photo Diode
R.I.	Reflected Intensity
RA	Resonance Angle
RH	Relative Humidity
RI	Refractive Index
RIU	Refractive Index Unit
RTD	Resistance Temperature Detector
SAM	Self Assembled Monolayer
SNP	Silver Nanoparticle
SNR	Signal to Noise Ratio
SP	Surface Plasmon
SPP	Surface Plasmon Polariton
SPR	Surface Plasmon Resonance
SPRIF	SPR Imaging through Fluorescence
TIR	Total Internal Reflection
TM	Transverse Magnetic
TP	Triphenylene-based discotic liquid crystal
UV	Ultraviolet
WIS	Wavelength Interrogation SPR

Symbols

S	Signal
N	Noise
F	Full width hlf minima
Q	Quality factor
A_m	Area per molecule
ΔD	Standard Deviation
E_A	Activation energy
T	Threshold value
k_y	Projected wave vector of incident EM wave
k_P	Wave vector of SPP wave
n	Refractive Index
Π	Surface pressure
Π_t	Target surface pressure
ϵ_m	Dielectric constant of metallic layer
ϵ_d	Dielectric constant of dielectric material
λ	Wavelength of EM wave
λ_R	Wavelength of EM wave at surface plasmon resonance
θ	Incident angle
θ_R	Resonance angle
θ_P	Polarization angle
$\Delta\theta_R$	Change in resonance angle
ω	Angular frequency

Dedicated to ***Dear Aanjaneya****, My* ***Sweet Family, Respected Teachers*** *and My* ***Beloved*** *Country* ***India****.*

Chapter 1

Introduction

1.1 Introduction

The Surface Plasmon Polaritons (SPPs) are transverse magnetic (TM) waves which appear due to the charge density oscillation at the metal-dielectric interface. SPPs can be excited by a polarized light wave incident onto the metallic layer (e.g., gold film) via a coupling high refractive index medium (e.g., glass prism). The SPP wave can establish a resonance with the incident electromagnetic wave (EM) wherein a maximum energy transfer can take place from the incident EM wave to the SPP wave. Such an optical condition is known as surface plasmon resonance (SPR) [1]. Thus, SPR is the collective oscillation of conduction band electrons which are in resonance with the oscillating electric field of the incident light, which will produce energetic plasmonic electrons through non-radiative excitation [2].

When the metal surface is illuminated with the p-polarized EM wave of a specific wavelength incident at a specific angle via a coupling medium, the projected wave vector of the incident EM wave matches with the wave vector of the SPP wave. This creates the SPR condition wherein the reflected intensity from the metal-dielectric interface goes to a minimum.

In 1902, Surface Plasmons (SPs) were observed as a narrow dark band in the polychromatic electromagnetic spectrum of diffracted light from a metallic grating [3]. In 1958, a large intensity drop was found in the reflected electromagnetic spectrum of a thin metal film deposited on a substrate [4]. In 1968, Otto explained such loss in reflectivity. The loss in intensity is due to the coherent oscillation of surface plasmons [5]. In 1968, Kretschmann and Reather demonstrated another easier configuration to excite the SPs by an attenuated total reflection approach. Towards the end of the 1970s, Kretschmann demonstrated material characterization using the SPR configuration [6]. Then in 1983, the first SPR biosensor was developed successfully [7].

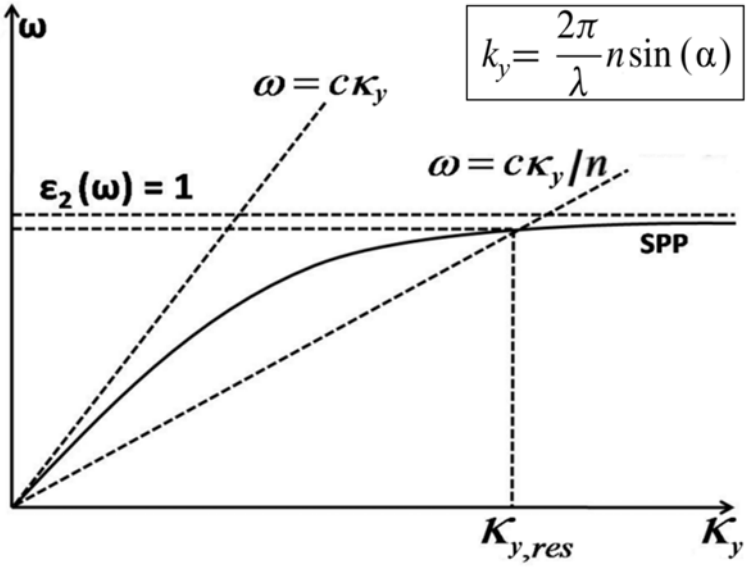

FIGURE 1.1: Dispersion relation of EM waves.

From the dispersion relations of incident EM waves in vacuum and SPP waves at the metal-dielectric interface (Fig. 1.1), it is clear that the non-trivial solution does not exist. Therefore, the SPR condition cannot be achieved in the vacuum/air medium. In order to create the non-trivial solution wherein both the dispersion curves intersect, it is essential to decrease the slope of the dispersion curve of the incident EM wave. This is possible only if the EM wave travels through a coupling medium with a refractive index (RI) greater than 1. It is thus suggested that in order to establish SPR, it is essential to allow the incident wave to

travel from a high refractive index coupling medium before striking the metal surface for the generation of SPP waves.

Let's consider an interface of two different media having the refractive indices $n_2 < n_1$, as shown in Fig 1.2. If θ is greater than the critical angle, the EM wave will undergo a total internal reflection (TIR). The evanescent wave in medium 2 can excite the SPP wave in an optically coupled metallic layer.

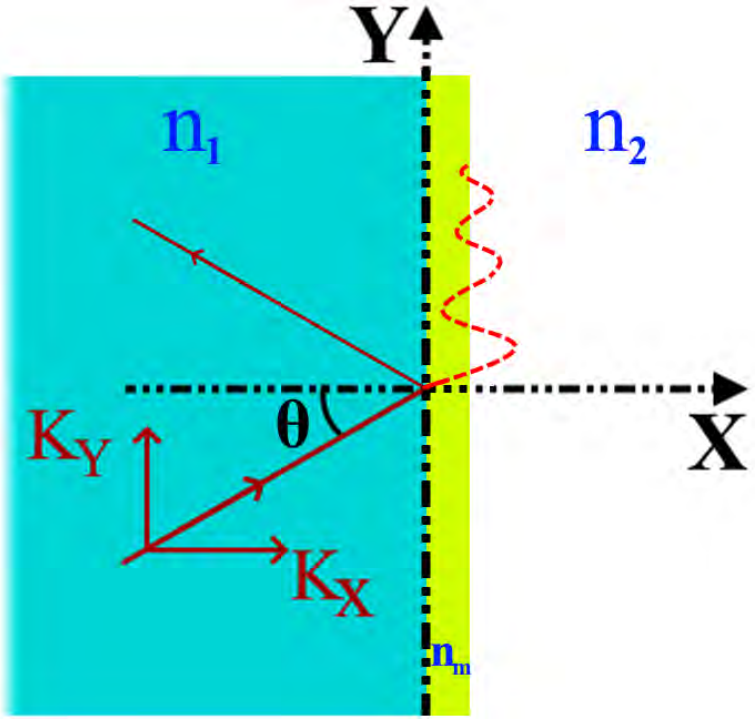

FIGURE 1.2: Refraction of light at the interface of two materials with refractive indices n_1 and n_2.

The y component of the wave vector for the plasmonic wave is

$$k_P = \frac{2\pi}{\lambda}\sqrt{\frac{\epsilon_d \epsilon_m}{\epsilon_d + \epsilon_m}} \tag{1.1}$$

where ϵ_d and ϵ_m are the dielectric constants of medium 2, and metal respectively.

Similarly, the y component of the wave vector for the incident EM wave is

$$k_y = \frac{2\pi}{\lambda} n sin\theta \tag{1.2}$$

At the resonance,

$$k_P = k_y \tag{1.3}$$

k_P depends on the dielectric constant of the metallic layer ϵ_m and its surrounding medium ϵ_d. A minute change in the refractive index of the metal's surrounding medium can perturb the wave-matching condition leading to a change in resonance condition [1]. The wave-matching condition of SPR can be obtained either by changing the wavelength (λ) or by changing the angle of incidence (θ). Accordingly, the SPR configuration can be specified in two different sections as follow:

1) Wavelength Interrogation SPR Sensor

2) Angular Interrogation SPR Sensor

1.1.1 Wavelength Interrogation SPR (WIS) sensor

A polychromatic EM wave source is used to illuminate the active area of the sensing chip (metal-dielectric interface) via the coupling prism at an angle greater than the critical angle of the glass prism. The minimum intensity corresponding to a specific wavelength (known as resonance wavelength λ_R) is recorded from the spectrum. A small change in the RI of the dielectric media surrounding the sensing layer can be observed in terms of shifts in the λ_R [8]. The WIS configuration is easy to realize. However, it is less portable and expensive due to the integration with a spectrometer.

1.1.2 Angular interrogation SPR (AIS) sensor

The active area of the sensing chip (metal-dielectric interface) via the coupling prism is illuminated with a focused monochromatic EM wave source . The reflected intensity at various incident angles is recorded to get a minimum in the reflected intensity. The intensity dip indicates the resonance, for which the corresponding incident angle is the SPR angle (θ_R). Any minute adsorption on the sensing surface causes changes in RI which in turn shifts the resonance angle (θ_R), as shown in Fig 1.3. The maximum resolution in the WIS configuration is 0.1 nm which can't be enhanced with the current state of the art [9]. In the AIS configuration, the resolution is in μ°, which can be improved more by using a lower step size motor or with some additional mechanical components. Due to higher sensitivity and resolution, a minute change in RI is reflected as a major shift in RA. The resolution of AIS (μRIU) is generally higher than the WIS (mRIU).

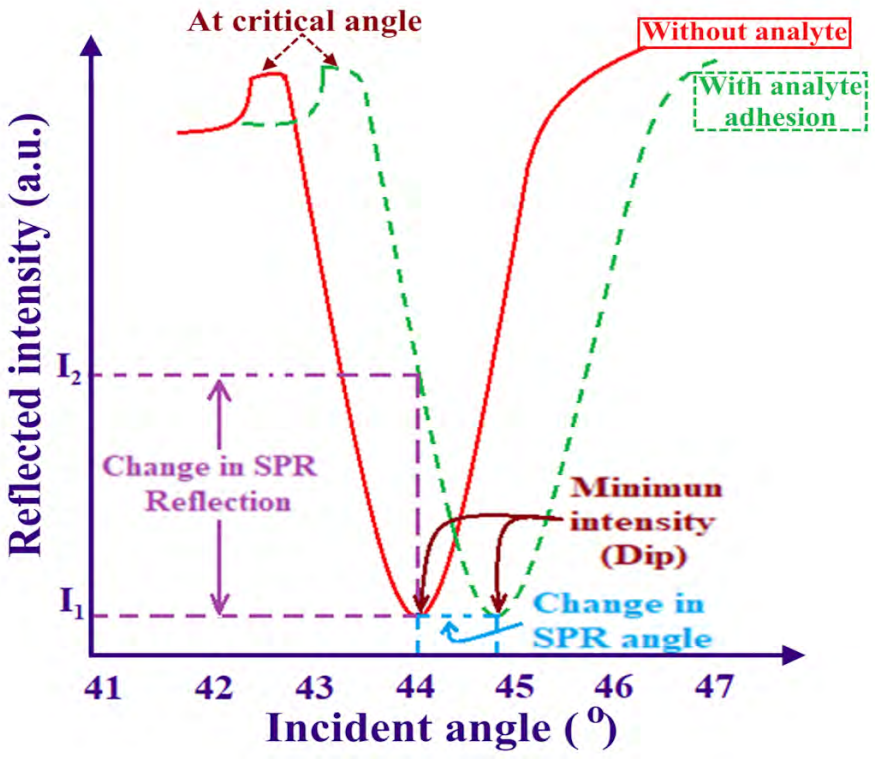

FIGURE 1.3: Schematic representation of the shift in SPR angle with respect to the change in RI of the dielectric medium.

Based on the optical setup, the angular interrogation can be classified into two configurations: (a) Otto SPR setup (Fig. 1.4(a)) and (b) Kretschmann-Reather (KR) SPR setup (Fig. 1.4(b)). In the KR configuration, the metal-dielectric layer is optically coupled with each other, and analytes have to flow on the free surface of the thin metallic film coupled with the coupled dielectric material [10]. In the Otto configuration, a gap of ∼100 - 200 nm is maintained between the metal film and the coupling prism. The analyte molecules must flow through the gap between the metal and dielectric media [11].

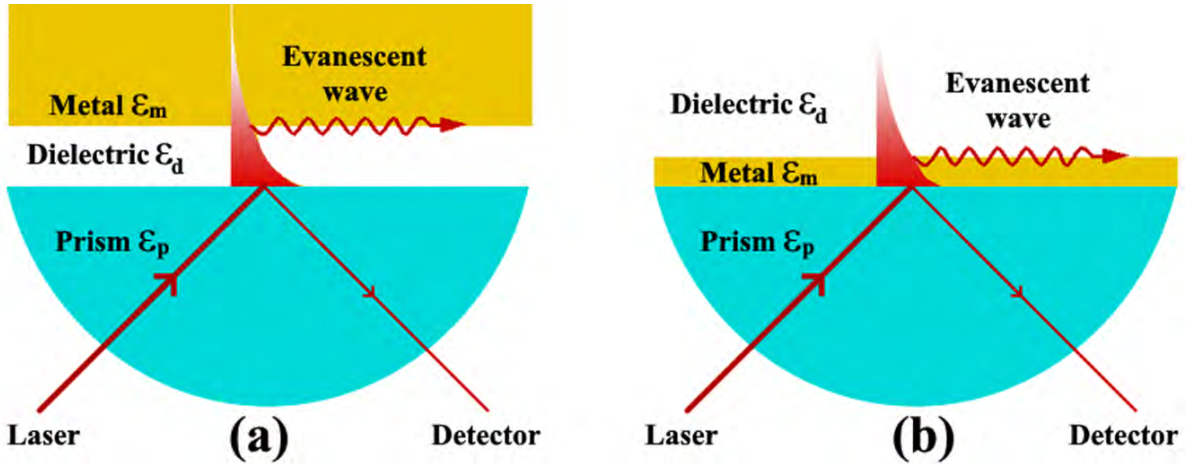

FIGURE 1.4: Schematic view of angular interrogation SPR sensor (a) Otto configuration (b) KR configuration.

The otto configuration is one of the most sensitive SPR configurations, but it needs a very complex setup. The KR configuration can show a balance performance on behalf of the setup cost and sensitivity.

Generally, the AIS system involves a goniometric setup [12, 13] or the double prism setup [14], which needs a more optomechanical driver system either in the sensing assembly or in the incident and detector assembly simultaneously. This makes the overall system not only costlier but also bulkier and complex in operation.

The schematic of the SPR spectrum obtained from KR based AIS system is shown in Fig. 1.5. The quality of the SPR chip can be analyzed using some parameters, viz. intensity of the signal (S), noise in the signal (N), and full-width half minima (FWHM). Here, S is the difference of intensity between the maximum (Max) and minimum (Min) values of the curve,

which is also known as the characteristic value of the SPR depth (Fig. 1.5). The N is the undesired fluctuation in the response signal. For a good SPR sensor, the characteristic curve should be sharp with a high value of S near the resonance value. Thus, the performance of the sensor is directly dependent on the value of S, while the value of F should be low. The value of noise (N) should be as low as possible as compared to the value of the signal (S). Thus, the well-defined term Signal-to-Noise Ratio (SNR) is used to relate the quality of the sensor's response in terms of the ratio of the output signal with respect to the noise received in the signal. It is defined as an estimation of the robustness of the preferred signal (S) relative to background noise (N). The higher value of SNR indicates a better quality of the signal [15–22]. The crucial parameter for an SPR sensor is the quality factor (Q) which is defined as the ratio of intensity (S) and the FWHM (F).

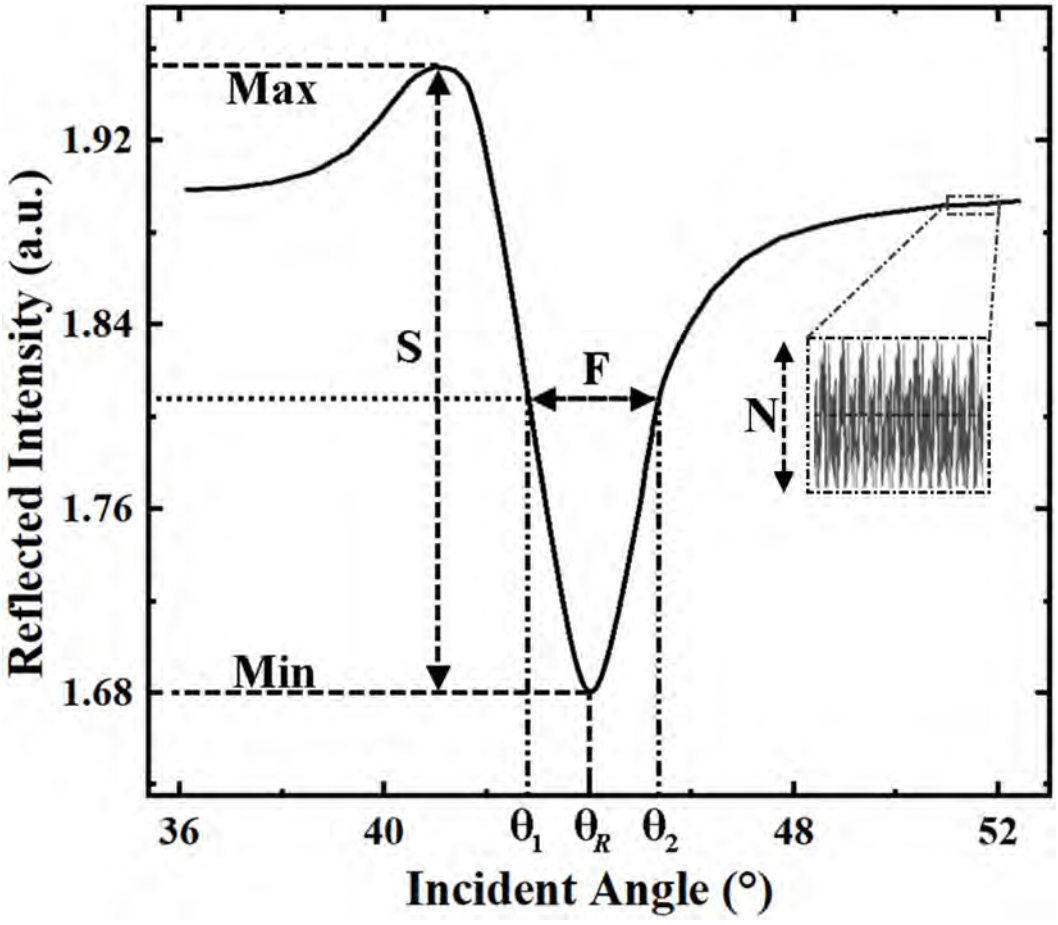

FIGURE 1.5: The schematic representation of the characteristic SPR curve obtained from AIS of KR configuration.

The analyte adsorption on the sensing chip can be analyzed either by static approach (shift in SPR angle ($\Delta\theta_R$)) or dynamic approach (real-time observation of change in intensity at the SPR angle (Kinetics)). High values of Q and SNR assist better sensitivity even for a minute change in surrounding dielectric media. Thus, the best resolution of the SPR sensor can be acquired by optimization of the setup parameters to enhance the SNR and Q values.

The p-polarized light illuminates the metal-dielectric interface and initiates an evanescent wave field into the thin metal film. This evanescent wave can excite the SPP waves. The resonance for the given interface can be achieved by altering the angle of incidence in the KR configuration. The minute change on the metal surface produces a significant shift in SPR angle, which can be observed precisely using an electro-optical transducer viz. light dependent resistor (LDR), photoresistor, phototransistor, photoresistor, photomultiplier, photodiode, charged couple device (CCD), etc. The value of the resonance angle depends on the refractive index of the surrounding media near the metal surface. The details of the instrumentation for our developed setup are discussed in the next chapter.

A specific target material (analyte) can be captured using some immobilized capturing agents (ligands). Ligands have some receptors which can bind the specific analytes in a mobile state flowing along a flow cell. Thus, the sensitivity and selectivity can be enhanced by functionalizing the surface of the sensor chip with some appropriate ligands. This process causes a change in the refractive index due to the adsorption of the analytes, which can lead to a change in intensity counts of the reflected light at the SPR angle. The schematic view of the SPR setup for the real-time measurement is shown in Fig. 1.6. The dynamic change in reflected intensity is denoted by the kinetics or sensorgram. The molecular association and dissociation coefficients can be identified via the rate of change in the SPR signal. Fig. 1.7 shows a complete cycle of molecular interaction kinetics schematically. The analysis of kinetic parameters is discussed in Fig. 1.7.

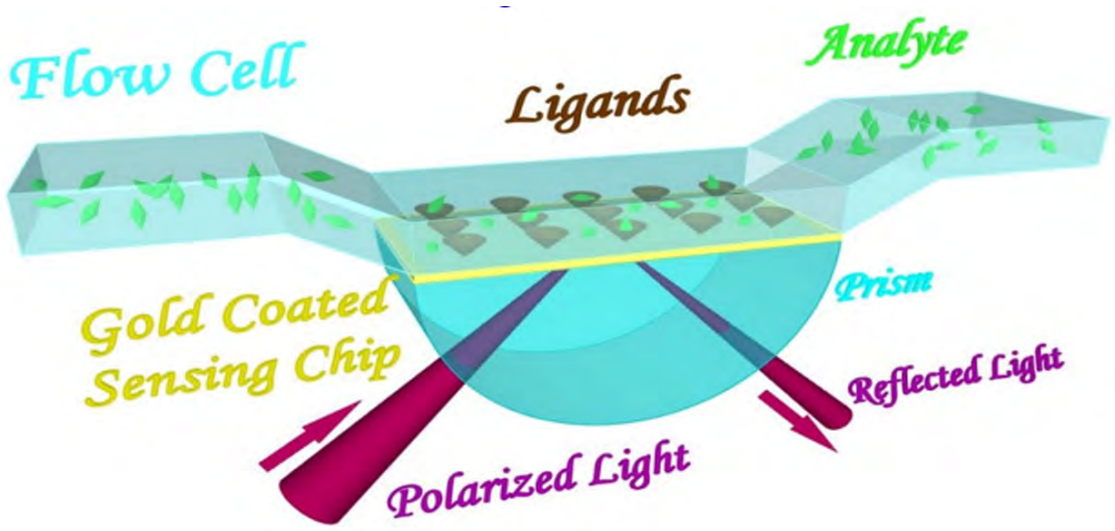

FIGURE 1.6: The schematic view of the SPR setup for the real-time measurement.

In the flow channel, the interaction of the analytes with the ligands can be observed as the change in the SPR angle (static approach) or intensity (dynamic approach) at the resonance condition. The approaches are relevant to the change in refractive index, which is directly proportional to the change in mass with either physical or chemical binding of analytes with the ligands. Thus, the nature of the molecular interaction can be observed in terms of the SPR signal.

The schematic of a kinetic curve is shown in Fig. 1.7. Initially, no analytes-ligand interaction appears, and all the ligands are free to capture the analyte molecules. In this condition, the SPR response (R.I.) follows a constant and continuous signal which is defined as the Baseline. With the flow of analyte molecules, the analyte ligands interaction increases. Thus, the SPR signal starts to increase monotonically with the increase in molecular binding, either physically or chemically. This phase is known as the Association. The adsorption or absorption depends on the nature of the analyte and ligand. For a high concentration of analyte, there is no free ligand remaining to capture the analyte molecule. Thus, the signal reaches a saturation state.

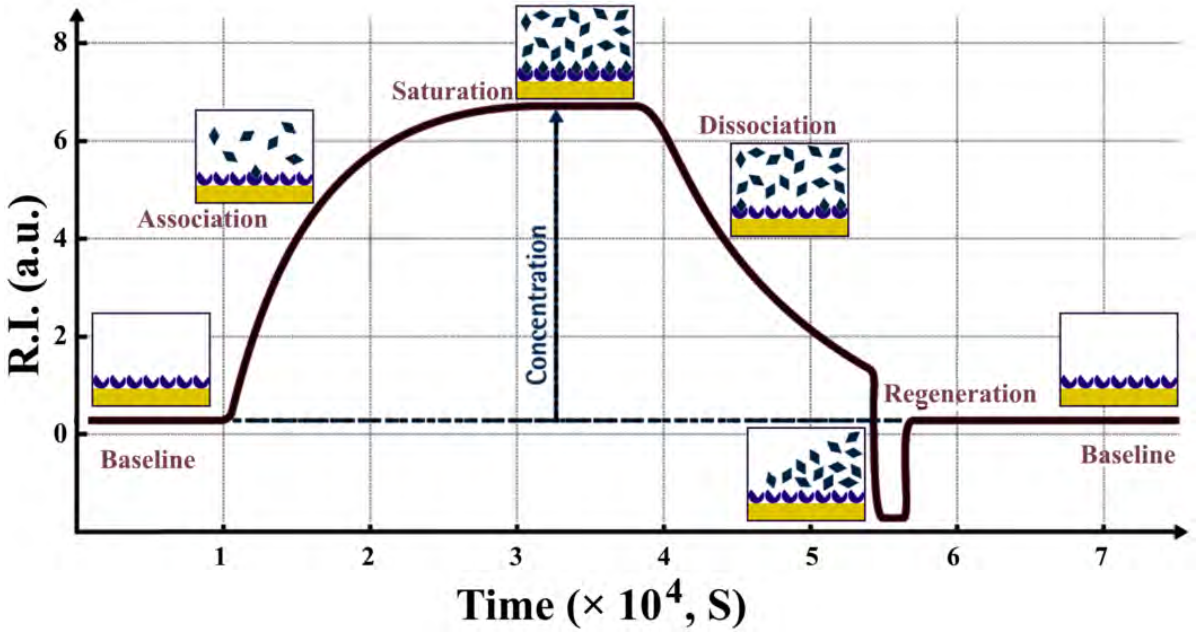

FIGURE 1.7: The schematic representation of the kinetics for molecular interaction.

Some buffer solution is used to desorb the analyte from the ligands to reuse the sensing chip. The kinetics signal goes down with the increase in desorption. This process is known as Dissociation. After the detachment, the signal reaches its initial intensity (baseline). Sometimes due to some surface modification in the layers of ligands, the response signal drops below the baseline. However, it may regenerate after some time, and the signal comes back to the baseline. The process is known as Regeneration.

This research describes the development of an advanced SPR instrument and a few of its applications relevant to traditional sensing applications. The instrument was employed to demonstrate some other applications, such as the measurement of birefringence in ultrathin film and optical switch.

1.2 Instrumentation

Some details of commercially available SPR instruments are mentioned below:

TABLE 1.1: Details of commercially available SPR instruments

S.No.	Equipment, Manufacturer	Specifications	
1.	BIORAD PROTEON XPR36 SYSTEM, UCONN HEALTH	Response uniformity	$<$ 2% CV
		Refractive index range	1.33-1.37
		Dynamic range	1-40000 Response unit
		Baseline noise	$<$1 RU, 1-20000 RU
		Baseline drift	$<$1 RU/min at 15-40 °C
		operating temperature	15-40 °C
		Autosampler temperature	2-35 °C
		sample configuration	72x1.5 ml vials or 2x 96-well microplates
		CCD	12 bit digital camera
		Acquisition rate	3Hz (3 images/sec)
		weight	85Kg
		Dimensions	95x58x50cm^3
		Light source	690nm
		Incident range of imaging	40-76°
		resolution	1 μm
		operating temperature	15-40 °C
		Dimensions	300x575x360mm^3

2.	SPRm 200, Biosensing Instrument	weight	50.8 Kg
		sample configuration	1-1500 μL
		Baseline noise	$<$ 0.6 RU RMS (0.1 m° RMS)
		Baseline drift	3 RU/hr (0.5 m°/hr) (when ambient drifts $<$ 1 °C/hr)
3.	BI-4500, Biosensing Instrument	Light source	670 nm
		Incident range	40-47° gas, 67-81° liq
		Detection speed	4ms
		Baseline noise	$<$ 0.06 RU RMS (0.01 mDeg RMS)
		Baseline drift	0.30 RU/hr (0.05 mDeg/hr) (when ambient drifts $<$ 1°C/hr)
		Operating temperature	6°C to 50°C
		Weight	40.8 Kg
		Dimensions	355×250×515mm^3
4.	Pioneer SPR, Octet® SF3 , Sartirius	Refractive index range	1.33-1.40
		Baseline noise	$<$ 0.1 RU - $<$ 0.3 RU

5.	Reichert4SPR, Reichert	Light source Refractive index range	780 nm <1×10-7 RIU, 1.33-1.40
6.	Coleparmer	Baseline noise Acquisition rate	<0.1 mdeg/rms < 1 μsec/point
7.	Portable P4SPR, Affinité Instruments	Sample configuration Weight Dimensions	550 μL 17 kg 78×57.5×36 cm^3
8.	SPRm200, Quantum Design	Baseline noise Baseline drift Operating temperature Sample configuration Weight Dimensions	< 0.6 TRU/RMS 3ru/hr (0.5mdeg/hr) 15-40 °C 1500 μL 50.8 Kg 690×330×340 mm^3

1.3 Applications of SPR from the literature survey

Some latest and most advanced sensing applications of SPR are included here in the tabular format collected from various literature as below:

TABLE 1.2: Applications of SPR sensor from the literature survey

Nature of application	Details of the research work	Limit of detection (LOD)	Reference
Food quality & safety	• Domoic acid (DA) was detected in shellfish e.g. mussels, oysters and cockles in inhibition format of the SPR sensor.	1 μg/g	[23]
	• Steroid hormone, progesterone was detected in milk using inhibition format. The progesterone derivatives were immobilized onto the gold surface of the SPR.	3.6 ng/mL	[24]
	• Detection of contaminants, 4-nonylphenol in shellfish using the monoclonal specific antibodies and inhibition detection format in the SPR sensor.	2 ng/g	[25]
	• Detection of Escherichia coli O157-H7 based on immunoassay sensing protocol using SPR sensor.	10^4 cells/mL	[26]
	• Staphylococcal enterotoxin B (SEB) was detected in milk and mushroom samples using the antibody of SEB immobilized onto the gold surface of the SPR sensor.	1 ng/mL	[27, 28]

	• Deoxynivalenol was detected in wheat using the SPR sensor. Deoxynivalenol conjugated with casein was immobilized onto the gold surface and the detection was done in inhibition format.	2.5 ng/mL	[29]
	• Peanut allergens were detected using the immobilized specific antibody on the gold surface of an SPR sensor.	700 ng/mL	[30]
	• The adulterants, non-milk proteins in dairy products, are detected employing polyclonal specific antibodies using a SPR sensor.	200ppb	[31]
Environmental monitoring	• The carcinogenic and environmental pollutant, benzo[a]pyrene was detected using the SPR sensor employing the indirect inhibition immunoassay format.	10 ppt	[32]
	• Detection of dichlorodiphenyltrichloroethane (DDT) in water using monoclonal antibodies specific to DDT and its derivatives immobilized over the gold surface of the SPR sensor.	15 pg/mL	[33]
	• Detection of Cu2+ ions using a polymer composite of squarylium dye deposited on the gold surface of an SPR instrument.	1pM	[34]
	• The explosive material and environmental pollutant, trinitrotoluene (TNT) was detected by monitoring the immunoreaction between trinitrophenol-bovine serum (TNP-BSA) conjugate and anti-TNP antibody using SPR sensor.	60 ppt	[35]

	• Detection of pesticide, 2,4-dichlorophenoxyacetic acid (2,4-D) using the indirect inhibition immunoassay by monitoring the interaction between anti-2,4-D antibody and concanavalin A-2,4-D conjugate using SPR sensor.	3 ppb	[36]
	• Detection of organophosphate pesticide chlorpyrifos and carbaryl using pesticide-sensitive SPR sensor.	1 ng/mL for carbaryl & 50 pg/mL for chlorpyrifos	[37–39]
	• Detection of heavy metals e.g. Cd, Zn and Ni using a protein metallothinein.	100ng/mL	[40]
	• The markers for cardiac muscle injury, myoglobin, and cardiac troponin I were detected using the antigen specific antibodies employing the SPR sensor.	2.9 ng/mL for myoglobin & 1.4 ng/mL for troponin	[41]
	• The pancreatic cancer marker, carbohydrate antigen (CA 19-9) was detected by a specific antibody against CA 19-9 using an SPR sensor.	410 U/mL	[42]

Biomedical	• Detection of pregnancy markers, human chorionic gonadotropin hormone (hCG) was performed by wavelength modulated SPR sensor with DNA-directed antibody immobilization method.	0.5 ng/mL	[43]
	• Vascular endothelial growth factor protein (VEGF) can have a role in the lung, breast, and colorectal cancers. VEGF was detected using SPR imaging by forming a microarray of the RNA.	1 pM	[44]
	• The prostate cancer marker, prostate - specific antigen (PSA) was detected using the monoclonal antibodies against PSA employing the SPR sensor.	0.15 ng/mL	[45]

1.4 Research gap

The field of SPR is very vibrant due to its versatile applications in various fields of science and technology. The label-free measurements and their sensitivity toward specific analytes have made it one of the largely sought techniques in the field of sensing. The SPR-based equipment is available commercially. However, there are only a few manufacturers, and hence the market is limited by their monopoly. The users are utilizing the features of the equipment as limited by the manufacturers.

For the development of next-generation SPR-based devices, it is essential to explore a multi-dimensional aspect of the measurements. There are some research and development in the field for addressing multi-analytes through multichannel SPR system, electrochemical SPR, and SPR imaging, however, the field is in a nascent stage. Extensive research and development are required for the next generation of SPR devices by adopting strategically the new concepts of sensing. Additionally, the functional layer deposited over the active area of the transducer plays a crucial role in establishing ligands-analytes interaction and thereby enhancing the efficiency and reliability of the sensor. The general practice of immobilization of ligands over the active area is the sequential deposition of several layers. This, in turn, increases the thickness of the ligands. Due to the large thickness, often the transducer does not perceive the physical changes due to the adsorption of analytes. In the case of SPR-based sensors, the extent of the plasmonic field in the dielectric medium (possessing analytes) is ∼100-300 nm. Therefore, if the effective thickness of ligands is beyond this range, it reduces the efficiency of the sensors due to the non-perceptibility of the analytes. There are some reports wherein, the sensing performance of a functional layer consisting of a single layer of molecules is reported to be superior compared to that of a thicker film. Therefore, strategically we deposited an ultrathin film of EM wave active materials on the sensing area of the SPR device and performed several traditional and non-traditional measurements.

In this thesis, we report the development of a very high-resolution, excellent sensitivity, portable, and low-cost SPR instrument. We demonstrated the capability of the SPR phenomenon for efficient sensing and beyond by observing EM wave polarization dependencies

on SPR response and the birefringence of ultrathin films. This R&D demonstrates the great potential of the SPR phenomenon for the next generation of devices, such as optical switches.

1.5 Objective

- Development of SPR instrument along with standalone software.
- Sensing application of SPR using self-assembled nanoribbons of discotic liquid crystal molecules.
- Surface plasmon resonance for the measurement of the polarization of EM wave-dependent sensitivity from an ultrasensitive layered structure.
- Surface plasmon resonance for optical switching application using ultrathin film of photoactive liquid crystal molecules.
- Some future development of the SPR instrument for versatile applications.

1.6 Research methodology

(a) Optical setup for allowing the monochromatic incident light to get reflected from the metal surface via the coupling prism. A suitable coupled electrical and mechanical module will be designed to achieve the resonance condition and monitor it as a function of time.

(b) SPR chip: The SPR sensing chip will be obtained by sputtering chromium ($\sim 3nm$) followed by gold ($\sim 50nm$) over BK7 glass plate. The gold surface will be functionalized with organic/nano-material ligands to yield a specific sensing active surface.

(c) Flow cells will be designed and fabricated for gas sensing and bio-sensing application. Suitable amendments in the SPR setup will be done accordingly.

The detailed methodology is discussed in the relevant chapters.

Chapter 2

Development of SPR instrument along with standalone software

This chapter discusses the instrumentation of the SPR device by adopting the novel optomechanical scanning process. The SPR instrument has a wide variety of applications in various fields of academia and industries. The commercially available SPR instruments are sensitive, however, they are very costly and complex in operation. There are several limitations to such equipment e.g., the limited angular range of scan, very high maintenance cost, high-end local infrastructure, complex operation, and analysis. We developed a low-cost, sensitive, and portable instrument with support from DST India. A laboratory prototype was developed by our group in the first phase of the project (2010-2013). Later, with the support from DST, India (2017-2019), we developed the equipment ready for commercialization. A multidimensional improvement in hardware and software was incorporated such that it can be transported anywhere in India and abroad for user-friendly SPR-related applications.

TABLE 2.1: Comparison of our SPR sensor with traditional SPR technologies.

S.No.	Comparison Parameters	Available SPR Equipments	Our Developed SPR Sensor
1	Cost	$\sim$ 1 crore	$\sim$ 5 lakhs
2	Weight	$\sim$ 100 Kg	$\sim$ 5 Kg
3	Sensitivity	$\sim$ 3 μRIU	$\sim$ 1.92 μRIU
4	Analyte requirement	$\sim$ 10 mL	$\sim$ 100 μL
5	Feedback mechanism	No	Yes
6	Field portability	No	Yes
7	Scan range	$< 10^{\circ}$	55°

Firstly, the instrument has been demonstrated before the Scientific Committee of DST-India at IIT-Delhi in 2018. Then as a part of the validation, we transported the equipment to Bangalore via a courier. The equipment was installed on a local reading table of a laboratory at Raman Research Institute and a set of experiments was performed. We obtained a satisfactory report from the scientists from RRI and some other places. A website (https://www.sprsensors.org) has been designed. This chapter contains details about the development based on hardware and the software of the SPR instrument "OptroniX20".

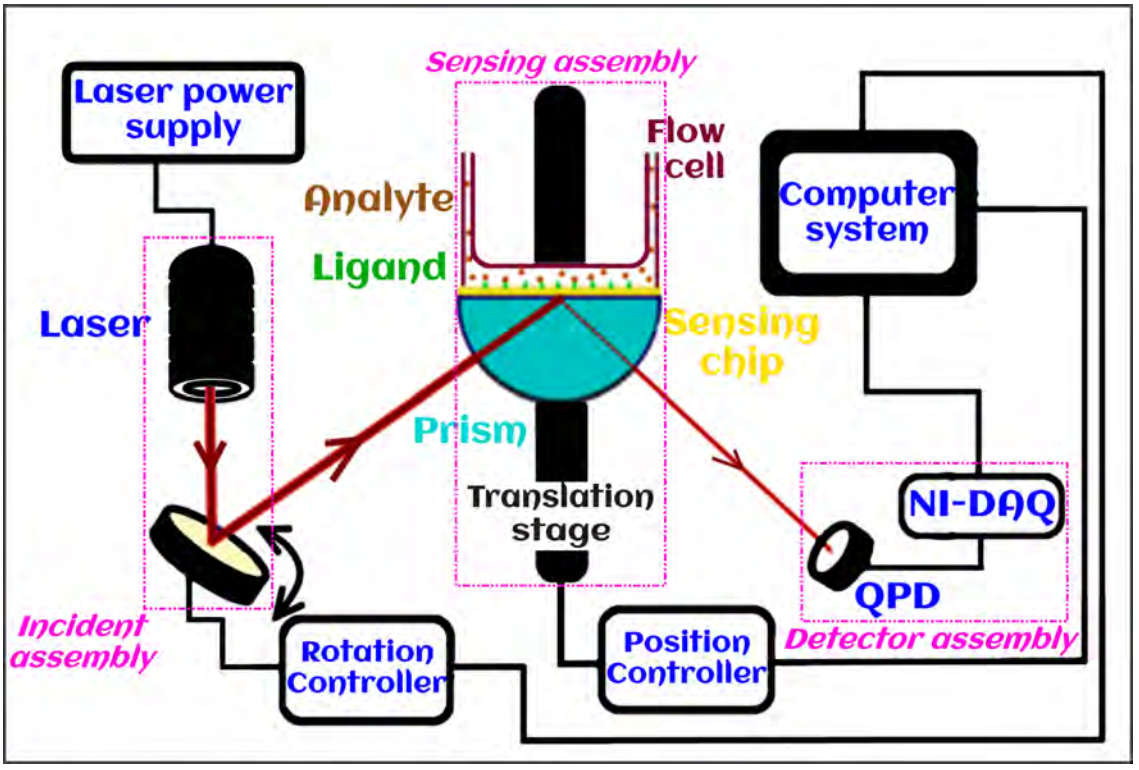

FIGURE 2.1: The schematic diagram of our Kretschmann configuration angular interrogation SPR sensor.

2.1 Major Components

2.1.1 Laser

In the Kretschmann configuration, the surface plasmon polariton (SPP) waves can be excited at the gold/dielectric interface using a monochromatic source of electromagnetic (EM) wave in TM mode using a laser. The SPR is detected by observing the minimum in the reflected intensity at a given angle of incidence. It is therefore very essential to use a stable source of EM waves in this configuration. The stability should be in terms of intensity as well as the wavelength of the laser source. In our setup, we used a 5 mW laser of wavelength 635 nm procured from Newport, USA (Fig. 2.2). The lasers with different power and wavelengths were tested.

FIGURE 2.2: Diode laser module.

The stability of a laser primarily depends on its optics and the power supply. The power supply of the laser used in our setup has 5VDC, 3A output. The stability of the measurement using a laser can be addressed by subtraction of the reference beam from the signal beam. This can be obtained by splitting and channelizing the input beam. This requires extra beam splitters, mirrors, optical component holders, beam collector units, data communicators, etc. All these units have complex alignment which increases the cost and the complexity of the overall system. But the stable input lacing system reduces the complexity with better and stable output and hence improves the portability and reliability of the instrument. Therefore, we have reduced the complexity of the final equipment by choosing a high-quality laser that can suitably fulfill all the criteria.

The stability of the system can be further improved by using a constant voltage transformer (CVT). CVT can be used whenever there is a large fluctuation in input power. However, the present power supply of the laser has an inbuilt robust circuit for the reduction of noise due to any such fluctuation.

The laser beam width and the focus can be adjusted by rotating a lens at the front head of the laser mold using a metallic spanner wrench which moves the encapsulated convex lens with respect to the laser diode. For the mechanical coupling of the laser with the other optoelectronic components, a 3D printed plastic (ABS/PLA) holder was designed to the needful specifications (Fig. 2.3).

FIGURE 2.3: 3D printed plastic holder for laser.

The wavelength and the power of the laser beam were measured for about 8 hours using an optical power meter (ILX power/wave meter). To collect the data from the power meter, a LabVIEW-based GUI software was developed.

The average power and the wavelength of the output beam observed were (4.020 ± 0.002) mW and (637.15 ± 0.1) nm, respectively (Fig. 2.4).

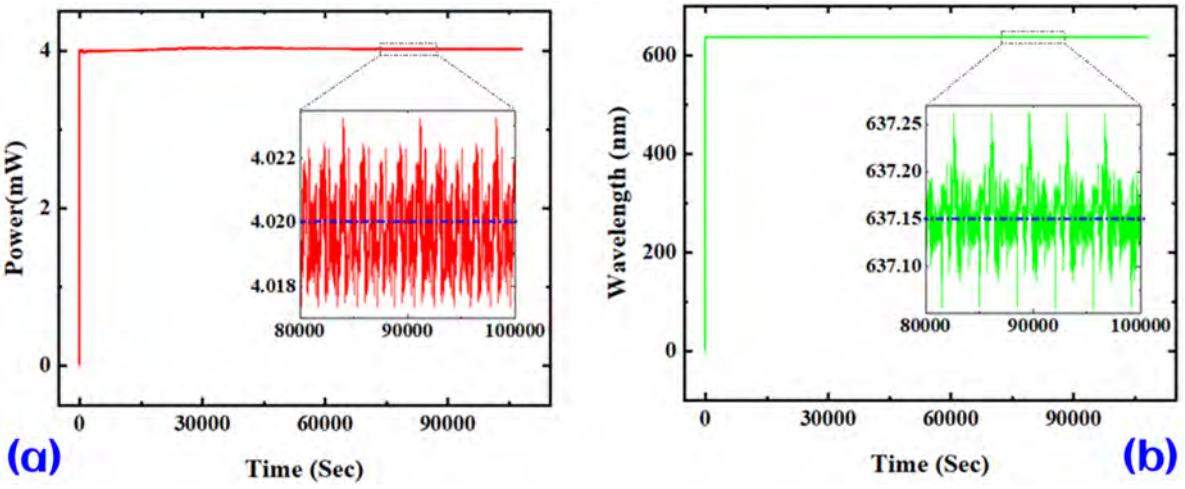

FIGURE 2.4: Power and wavelength stability plot for the laser diode. The insets show zoomed data. The dashed horizontal line represents the average.

It can be observed from the graph (Fig. 2.4) that the laser shows very good stability at the moment it is switched on. However, we have allowed a stability time for the laser to be 15 minutes before performing the experiments.

2.1.2 Mirror

In the angular interrogation Kretschmann configuration [6, 46], the SPR spectrum is generated by changing the angle of incidence and simultaneously measuring reflected intensity. The change in incident angle by direct rotation of the laser is impractical as it can limit the range of angle of incidence to a few degrees and can cause loose/break the electric connections between the controller and the laser diode unit. Thus, instead of changing the angle by direct rotation of the laser, the laser beam can be precisely deflected by a mirror-motor arrangement. Here a silver polished mirror is attached to the shaft of a motor, which can rotate the mirror to reflect the incident beam at a particular angle.

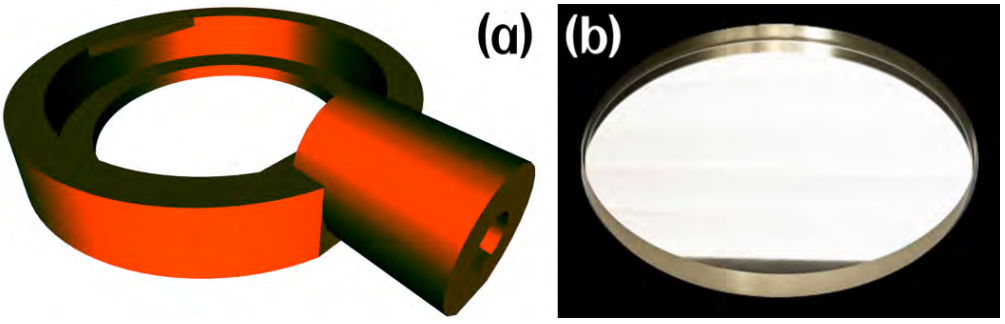

FIGURE 2.5: (a) Holder for the mirror. (b) Mirror.

A circular flat glass mirror (Fig. 2.5(b)) of diameter 2 cm and thickness of 1 mm with 500 nm thick sputtered silver coating was used. It provides 98% reflectivity for the visible spectrum wavelength range from 400 nm to 700 nm.

For holding the circular mirror, a suitable mirror holder (Fig. 2.5(a)) was designed and printed using a 3D printer. Additionally, the holder acts as the mechanical connecting bridge between the mirror and the motor.

The surface of the mirror was cleaned gently using ethanol and isopropanol to remove microscopic dust particles and any other organic impurities. Such cleaning is important for the reduction of stray scattering from the mirror surface.

The stability of the reflected beam of laser from the mirror was studied by recording the power and wavelength using the power/wavelength meter (Fig. 2.6).

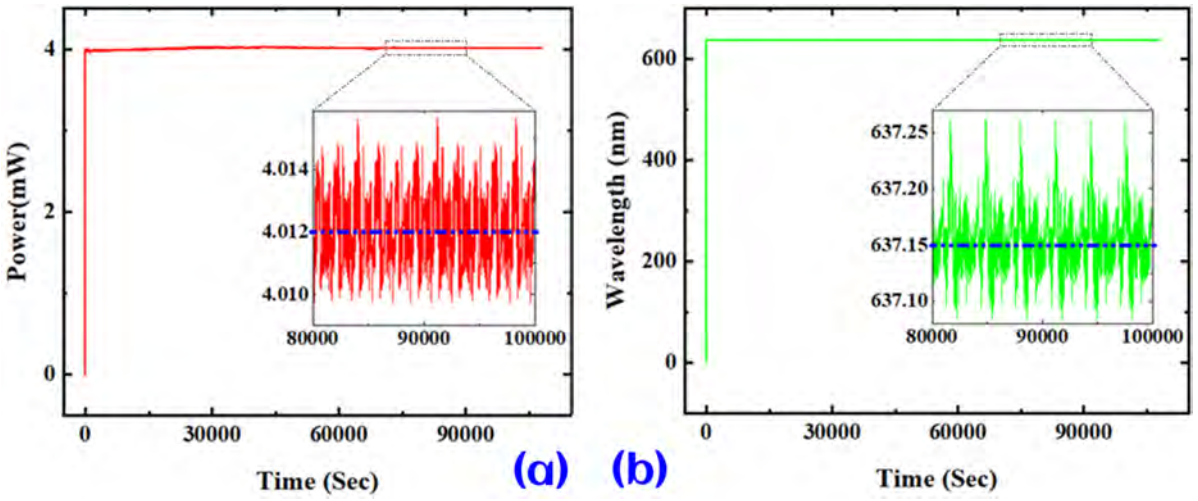

FIGURE 2.6: Power and wavelength stability plot for the laser beam reflected from the mirror. The insets show zoomed data. The dashed horizontal line represents the average.

The average power and the wavelength of the output beam observed were (4.012 ± 0.002) mW and (637.15 ± 0.1) nm respectively. This indicates that the reflected beam is very stable in terms of its power and wavelength.

2.1.3 Piezomotor with encoder

For a high-resolution SPR instrument, the angle of the incident beam should be changed either continuously or with a very small step size. The use of a goniometer ensures a continuous change in the angle of incidence along with a simultaneous track of the reflected beam. However, the goniometric arrangement can increase not only the cost of the equipment but also increases the bulkiness of the instrument. Therefore, the angle of incidence in the present case was changed stepwise using a high-resolution piezo motor (shown in Fig. 2.7(a)). A Piezo

motor is a small rotary motor that provides an adequate torque to rotate the mirror with a very high resolution of 1.2 micro-radian. The piezo motor was controlled using computer programming.

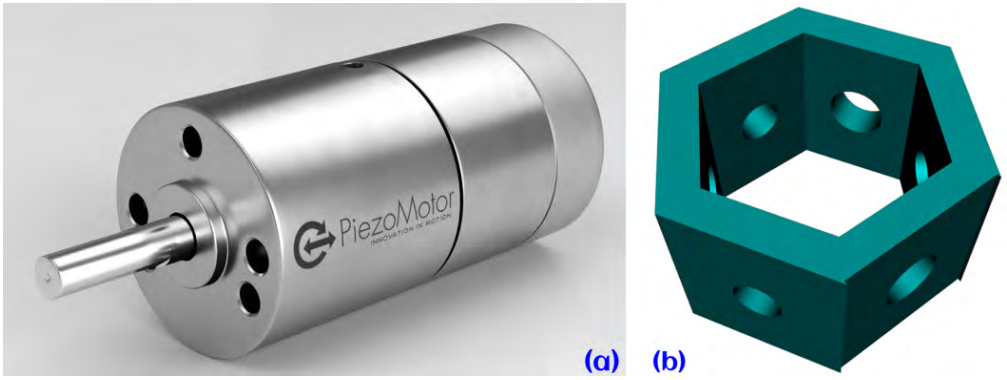

FIGURE 2.7: (a) Piezo motor (b) 3D printed holder for the piezo motor.

2.1.4 Prism

In order to generate surface plasmon waves, the EM wave should travel from a medium with R.I. $>$ 1 before getting incident on the metal surface. Therefore, a glass prism of a given refractive index can be utilized. Here, we used a semi-cylindrical glass prism (BK7, R.I. = 1.51) is shown in Fig. 2.8. The length, width, and radius of the prism were 2.5 cm, 2 cm, and 1 cm, respectively.

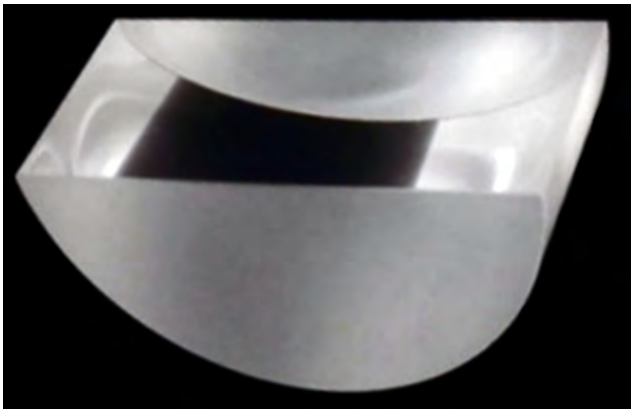

FIGURE 2.8: Semi-cylindrical BK7 glass prism.

In order to have a precise measurement of the angle of incidence, the laser beam is directed at the center of the semi-cylindrical prism. This arrangement ensures no deviation of the laser beam due to the refraction at the prism-air interface. This will avoid errors in the calculation of the angle of incidence which can be measured directly from the piezo motor counts. The advantage of the use of the semi-cylindrical prism in the SPR system can be seen in Fig. 2.9.

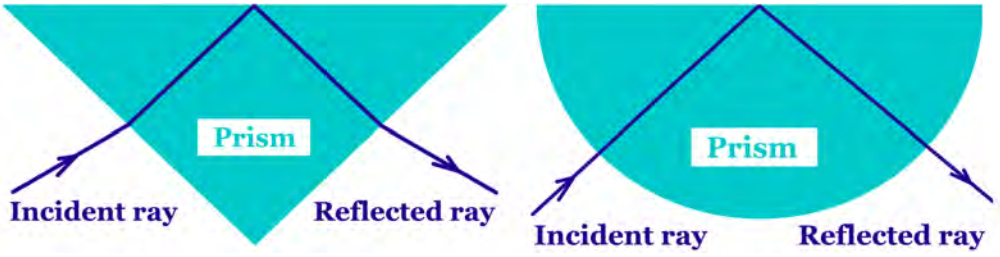

FIGURE 2.9: Schematic showing the use of a semi-cylindrical prism as compared to that of a triangular prism.

2.1.5 Sensing chip

The sensing chips consist of layered structures deposited onto glass substrates having the same refractive index as that of the coupling prism. The SPR chips are made up of BK7 glass (RI=1.51) plates coated with a thin layer of 50 nm thick gold film. Gold has poor adhesion on the BK7 glass. Thus, to improve the adhesion, a thin layer of chromium or titanium was deposited on the substrate. This enhances the stability of the sensing chip against desorption and the chip can be utilized several times.

Various shapes and sizes of the sensing chip can be chosen as per the requirement. We have used the $20x20x0.3mm^3$ size of the BK7 glass plates for the fabrication of the SPR chips.

The use of gold film for SPR chips has several practical advantages. The thin film of gold is chemically inactive [47]. Oxidation of gold is rare under normal atmospheric conditions. Even, the gold nanoparticles can be used as templates for the nucleation and growth of molecules [48]. Additionally, a good chemical affinity of gold towards the thiol group ensures the deposition of a self-assembled monolayer (SAM) during the functionalization of the SPR chip. In the standard protocol of specific functionalization of the SPR chip during sensing

application, it is often essential to deposit SAM during the immobilization of the ligands. The pure gold surface can chemically bind with -SH groups of thiol molecules to yield a very stable SAM.

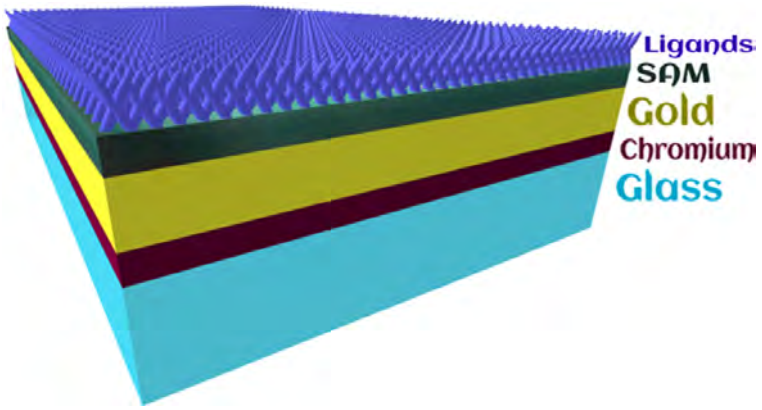

FIGURE 2.10: Schematic view of SPR sensing chip.

The gold film of a thickness of 50 nm on BK7 glass plates yields the best SPR sensorgram with the highest Q and SNR [49, 50]. The fact was verified via experiment and simulation approaches. Fig 2.10 shows the schematic view of the SPR sensing chip. The functionalization process includes the deposition of thin films of suitable materials via various techniques viz. self-assembly, Langmuir-Blodgett (LB) and Schafer (LS) techniques, spin coating, and drop-casting. Some of the techniques are discussed below:

2.1.5.1 Langmuir-Blodgett techniques

A stable mono-molecular thick film at the air-water interface is termed a Langmuir monolayer. The molecules in the Langmuir monolayer are constrained to move only on the two-dimensional (2D) surface provided by the smooth water surface. Hence, a Langmuir monolayer system can be considered a two-dimensional system. Such a 2D system has largely been studied by exploring a large number of organic molecules like fatty acids, cholesterol derivatives, proteins, polymers, and nanomaterials. The Langmuir monolayer of such materials exhibits a variety of surface phases e.g., gas, liquid expanded, liquid condensed, and solid phases. The surface

phases of the Langmuir monolayer are dependent on surface density, temperature, ion content of subphase, etc.

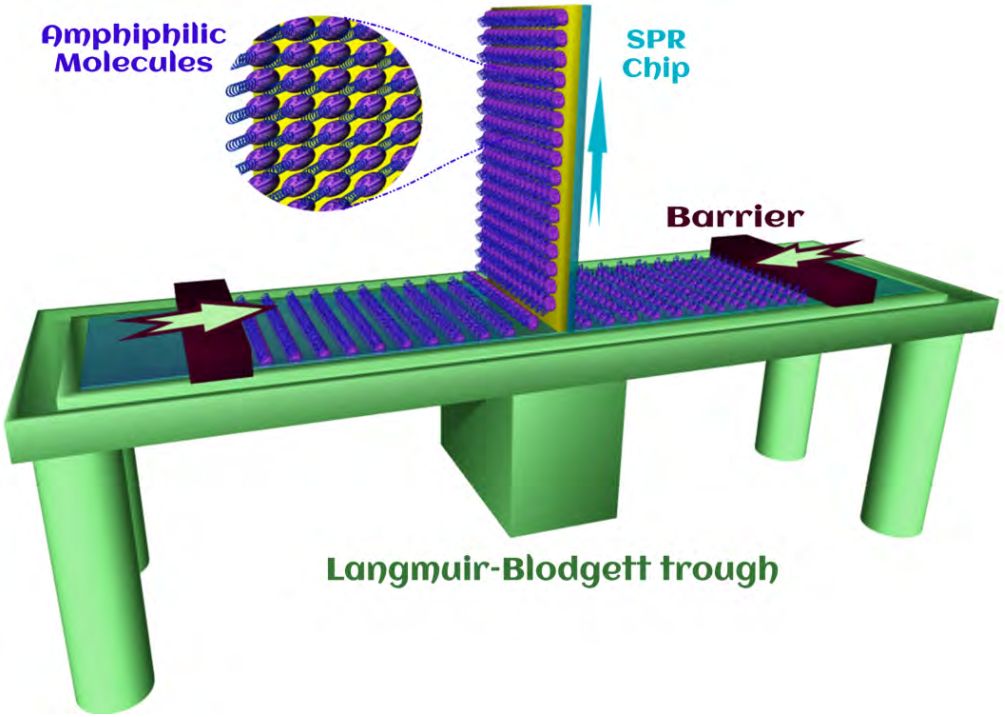

FIGURE 2.11: Langmuir – Blodgett (LB) film deposition.

The thermodynamics of such a 2D system can be studied by measuring the surface pressure (Π) – area per molecule (A_m) isotherms at different temperatures. The materials in a given surface phase can be transferred to solid substrates by vertically dipping the substrate in and out of the aqueous medium. This mechanism is popularly known as Langmuir-Blodgett (LB) technique. The LB deposition technique ensures the surface phase and the number of layers to be deposited.

The necessary requirement for the molecules to form a stable Langmuir monolayer at the air-water interface is its amphiphilicity. The amphiphilic molecule possesses two parts: hydrophilic (HPL) head group and hydrophobic (HPB) tail group. At the air-water interface, the HPL group of the amphiphilic molecule is anchored to the water medium whereas the HBP group stays away from the water medium. With the proper balance between the HPL and HPB part, a stable Langmuir monolayer at the air-water interface can be achieved. However, there

are pure HPB molecules e.g., polymers, carbon nanotubes, and graphene can also form a stable Langmuir monolayer at the A/W interface. The stability may be achieved due to entropic reasons. A schematic of the LB film deposition technique is shown in Fig 2.11. More details about the experiment using an LB trough can be found at [51, 52].

2.1.5.2 Self-Assembled Monolayer (SAM)

A self-assembled monolayer (SAM) is one molecule thick layer of material that assembles to a surface as a result of physical or chemical bonding during a deposition process. It is an easy and cost-effective solution to obtain a single layer of well-structured organic films at an air-solid interface. Some organic materials like organosilanes and organothiols show a very high potential to fabricate the SAM on substrates such as silicon (or glass) and gold, respectively [52].

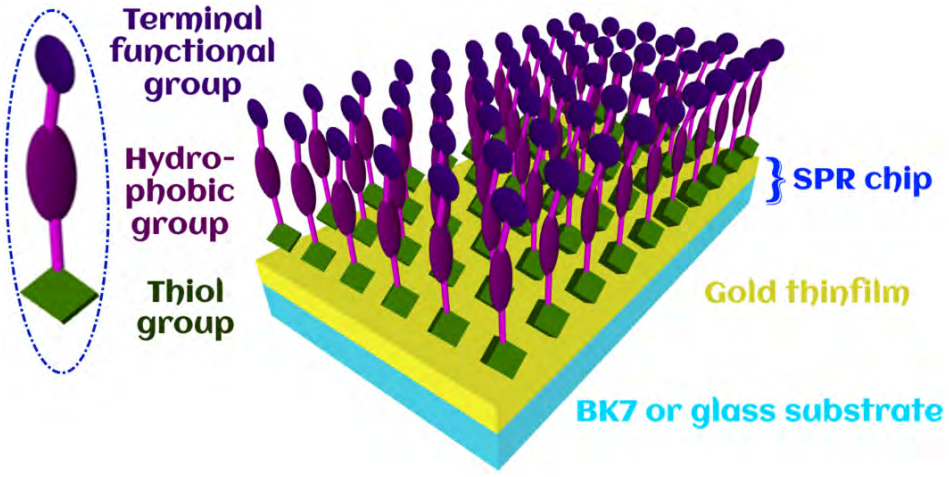

FIGURE 2.12: The schematic of SAM on SPR chip.

Due to the chemical bonding, the stability of ultrathin SAM is higher than the LB monolayer. The surface properties can be easily tailored by changing the functional end of the film-forming molecules. The schematic of the SAM deposited on the gold surface of the SPR chip is shown in Fig. 2.12.

Organosilanes and organothiols can form the SAM on a hydroxylated silicon surface and noble metals through the solvent route, respectively. The terminal groups may contain carboxyl

(–COOH), nitrile (–CN), hydroxy (–OH), amide ($–NH_2$), antigens or DNA. Hydrophobic groups may include some aliphatic chains or phenyl ring/s ($C_6H_5–$). Fig. 2.13 shows the schematic of the formation of SAM [52].

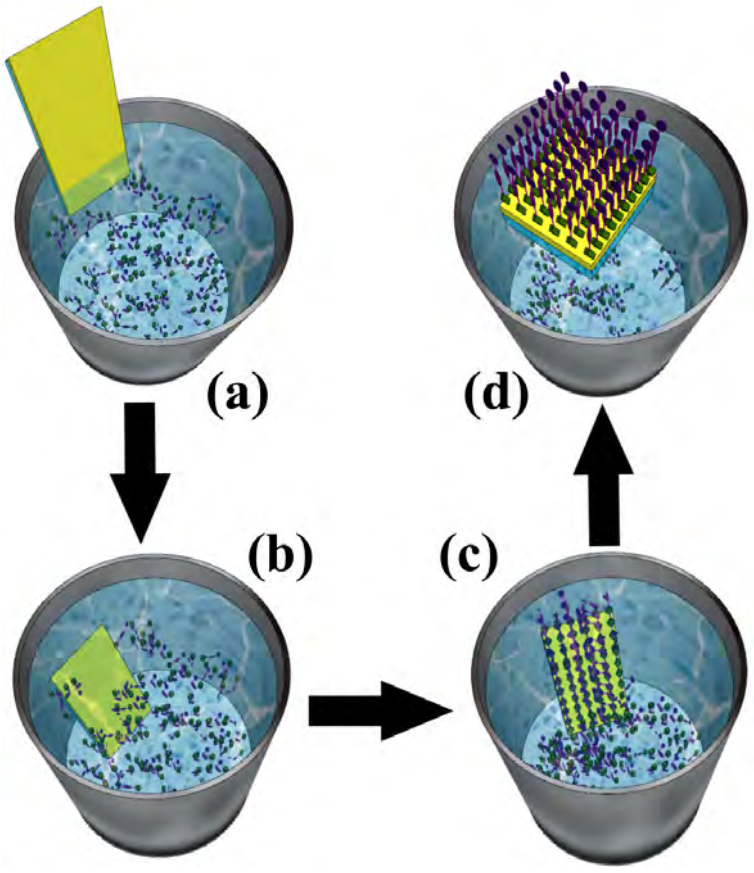

FIGURE 2.13: Schematic diagram of the formation of a self-assembled monolayer.

The formation of the SAM also depends on temperature, substrate, solvent, etc. A highly clean chip is immersed in the solution of SAM-forming molecules (a). Initially, the molecules start to absorb on the surface by quickly forming chemical bonds with the surface molecules (b). The adsorbed molecules rearrange to form a well-organized film (c),(d) [52, 53].

2.1.5.3 SPR sensing chip fabrication process

The substrate needs objective-driven treatments at different stages. The development of the sensing SPR chip is shown in Fig. 2.14.

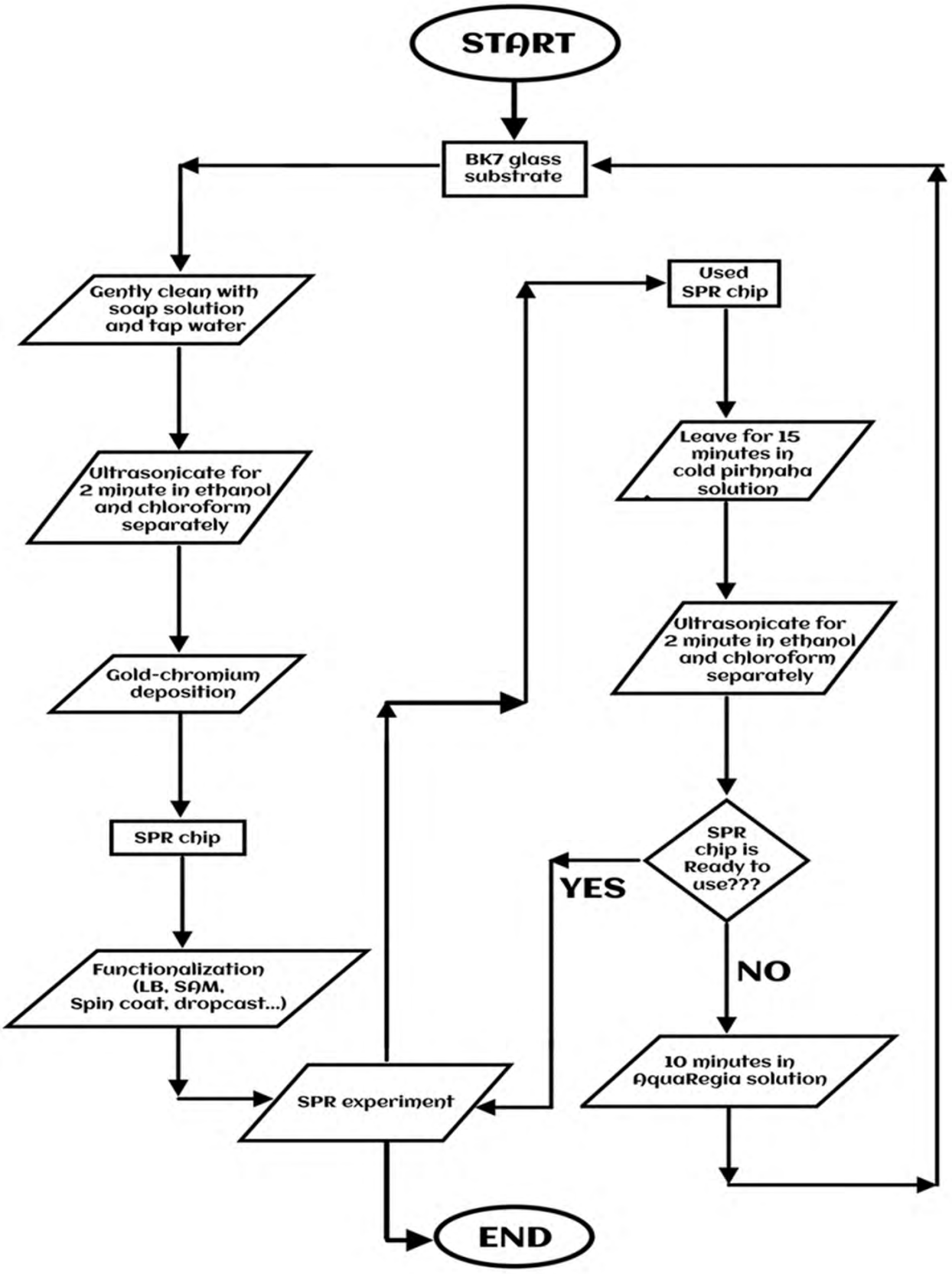

FIGURE 2.14: Flow chart of treatment of BK7 substrate and SPR sensing chips.

2.1.6 Quadrant Photodiode (QPD)

The SPR response can be collected in terms of the intensity of the reflected light. An optoelectronic array transducer has been used to convert optical signals into into electronic signals. These transducers are based on semiconductor technologies that can generate a current in an external circuit by the absorption of photons.

A variety of optoelectronic transducers i.e., photoresistors, photo-transistor, light-dependent resistors, etc. are available but the photodiode provides a quick response to light exposure. It is one of the fastest optoelectronic transducers with higher sensitivity [54]. Due to its linear current-voltage characteristics with very high SNR for the required range of wavelengths, it doesn't require any complex calibration. The low weight, compact design, and the requirement of the low biasing voltage of the photodiodes ensure easy installation in the electronic circuit.

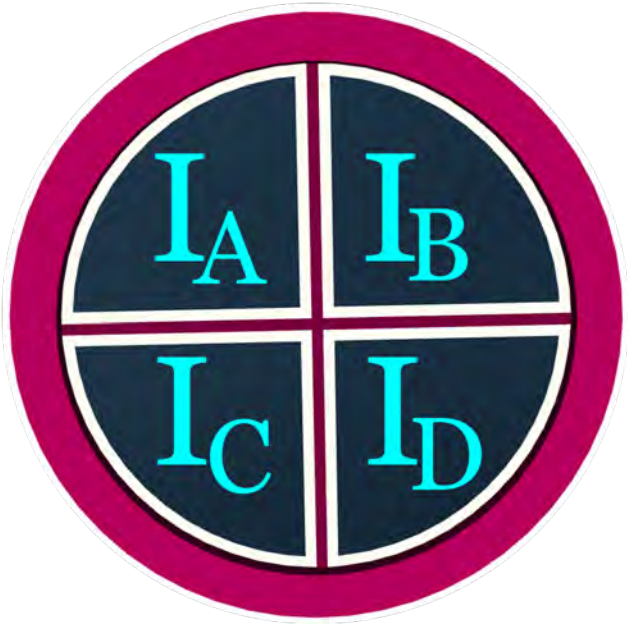

FIGURE 2.15: Front view of the Quadrant Photodiode (QPD).

We have used a segmented array photodiode with a circular active area consisting of four independent quadrants separated by a $\sim 10\mu$m gap (Fig. 2.15). To collect the independent signal from each of the quadrants, each section has one separate terminal and a common terminal as a ground, which was used to collect the output in terms of voltage.

2.1.7 Data Acquisition (DAQ) system

The DAQ system is used to collect and process data from the QPD unit. The physical parameters like temperature, pressure, humidity, current, wavelength, frequency, etc. can be read as analog signals using a DAQ which can be converted into digital signals along with some preprocessing. A variety of DAQ units are available but here we are using 64-bit USB-based DAQ (National Instruments, USB-6211).

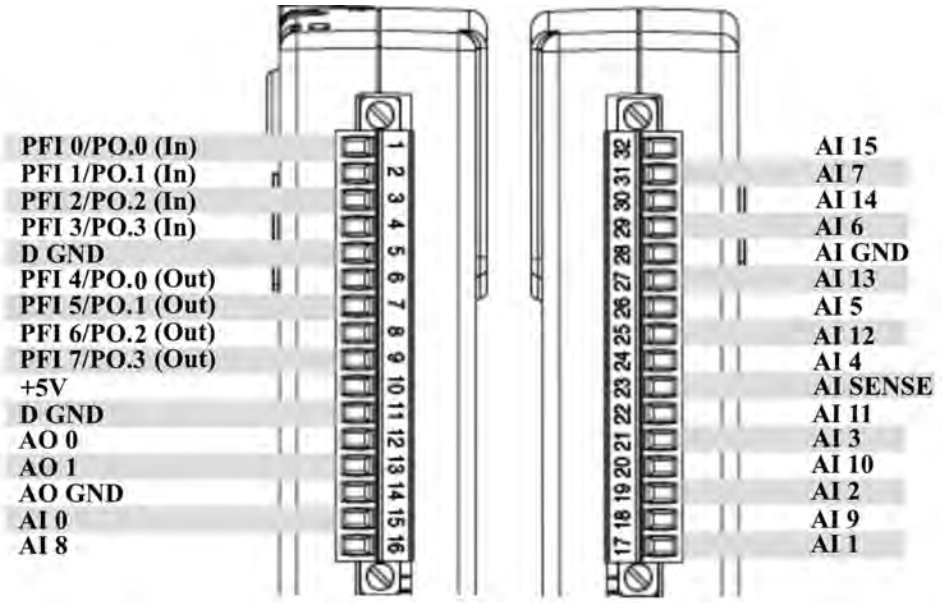

FIGURE 2.16: Pin diagram of Data Acquisition Unit.

The pin diagram of the DAQ unit is shown in Fig. 2.16. It is a multifunction data acquisition system that offers 16 Analog Inputs capable of 16-Bit transmission at the sampling rate of 250 kS/s, 2 analog outputs of 250 kS/s, 4 digital inputs, 4 digital outputs, and two 32-bit counters. It has an in-built amplifier system that facilitates fast-settling times at high scanning rates. The signal streaming technology that gives direct memory access such as the bidirectional rapid streaming of data across USB. The device is ideal for testing, control, and design applications including portable data logging, field monitoring, embedded OEM, in-vehicle data acquisition, etc.

2.1.8 Translation stage

Translation stages are used to move any Opto-electromechanical system which needs the precise movement of components. In the proposed optomechanical design, the prism assembly has to be translated vertically in coordination with the angle of incidence. We have used a linear translation stage capable of moving only along one axis. The image of the translation stage along with its controller is shown in Fig. 2.17.

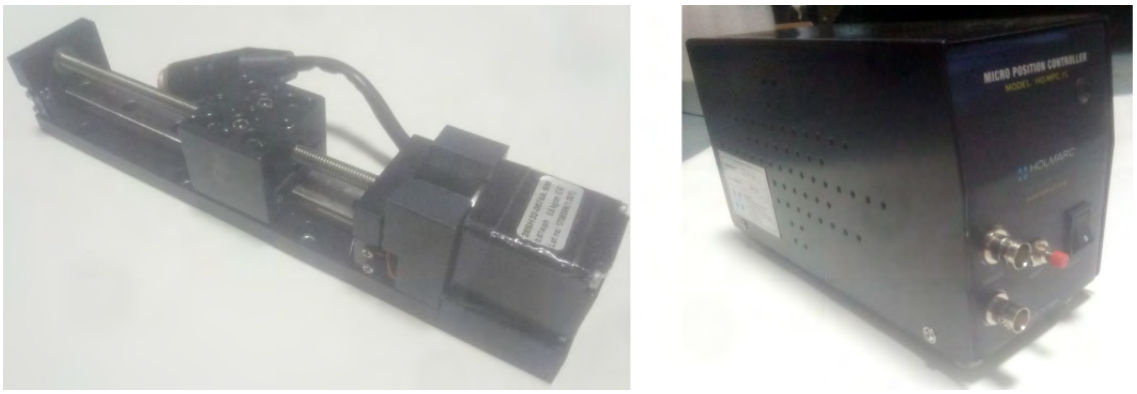

FIGURE 2.17: Translation stage and its controller.

To cover the range of angle of incidence from 35° to 85°, the previous version required two-axis translation stages each for linear motion in the horizontal and vertical directions. The full range of incidence was divided into parts of 5° to 10° for a single scan. Thus, it needed a lot of mechanical arrangements and time to perform a single scan. Even to get a full sensorgram, it needs a number of time-consuming post-scanning operations/calculations. This is simplified in the present setup by choosing a long-range uniaxial bidirectional translation stage. The stage is capable of traveling a distance of 10 cm. The translation stage is computer controlled.

Our SPR instrument has been designed with an optimized vertical axis linear translation stage with better resolution. The parameters have been optimized to cover its full incidence range of 35° to nearly 85° in a single scan which makes it suitable for sensing measurements in various ambient eg. gaseous and aqueous mediums without any further modification in optics.

2.1.9 Post system (Opto-mechanical components)

The optomechanical system needs the positioning of optical units such as prisms, lenses, reflectors, beam-splitters, filters, and diffractive elements in mechanical structures which allow the optical system to be constructed with high accuracy.

The post system includes a post, post holder, post holder base, and post collar. Posts are stainless steel rods with a precise specific diameter and length and have precise ground finishing on their surface. Generally, both ends of the post are made suitable for further connectivity with other optical post systems. These posts and holders are convenient units for holding various optical mounts for the optical component installation in a breadboard-based experimental setup. These post-mounting systems are preferable where the precise positioning of optical units is necessary with some easy arrangements for adjustable heights and angular positions.

2.1.10 Outer body

The SPR sensing unit is housed in a black color polymethyl methacrylate (PMMA)box. The dimensions of the sensing unit are 200×200×600 mm3. The black color reduces the entry of outside stray light. We have used the thickness of the PMMA sheet to be around 5 mm. Such a thick PMMA sheet reduces the thermal and air drift inside the sensor. The unit is built on a 200×200 mm^2 optical breadboard made from a 5 mm aluminum sheet. The entire sensing unit was found to be very stable against any mechanical/optical/thermal or air drifts. The controller unit includes some heavy electronic and electrical systems. The controller unit was enclosed using black anodized aluminum alloy sheets and some plastic material. The dimensions of the controller enclosure were ∼180×330×360 mm^3.

2.2 SPR Setup

The SPR instrument in Kretschmann configuration with angular interrogation method was developed in the laboratory. In the development of this equipment, the role of the goniometer has been removed and a unique feedback-driven optomechanical scanning system was adopted. The schematic of the SPR instrument is shown in Fig. 2.1. The photograph of the actual instrument is shown in Fig. 2.18. The whole setup has been divided into three sections:

1) Incident assembly (Laser, Mirror, and Piezomotor)

2) Sensing assembly (Translation stage, Sensing chip, and Prism)

3) Detector assembly (QPD detector, and DAQ unit)

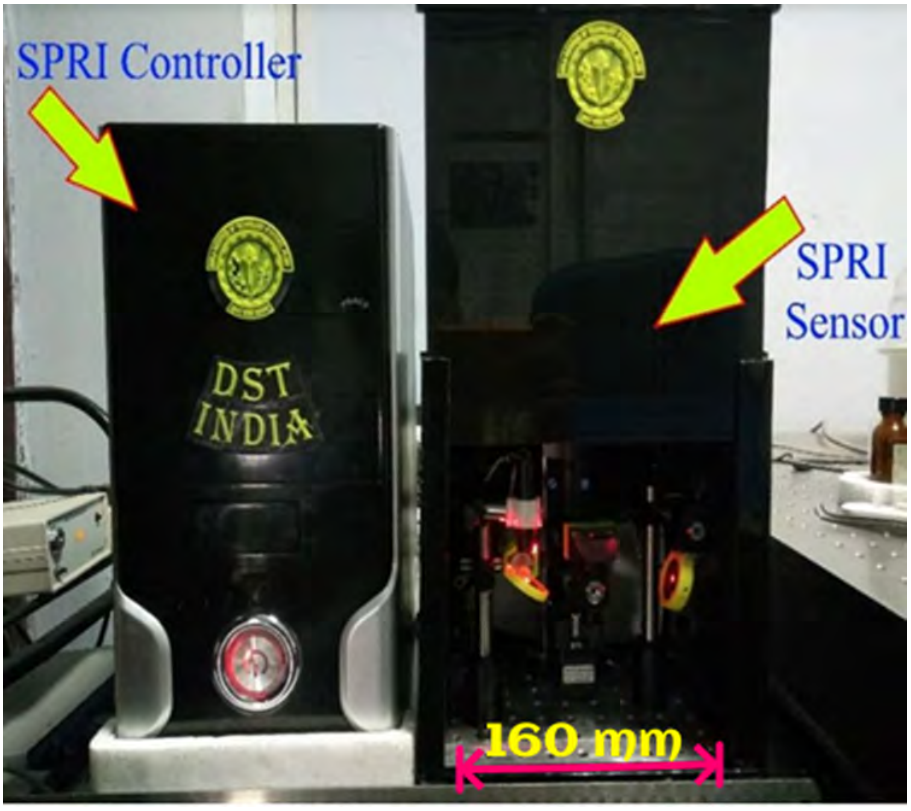

FIGURE 2.18: Actual image of our SPR sensor.

The diode laser is a very small and lightweight source of polarized light. The black anodized laser source is held by a 3D-printed laser mount which can be further connected with a post system.

The circular silver-coated mirror is attached to the piezomotor's shaft with the help of a 3D-printed mount. The assembly is called a mirror-piezomotor assembly (MPA). By using the post system, the laser source is adjusted just above the mirror in such a way that the laser beam can shine on the mirror's reflecting surface. The piezomotor provides the controlled rotation to the mirror to change the angle of the incident beam.

The sensing assembly contains a BK7 glass prism and a sensing chip which are mechanically mounted on a vertical translation stage. The translation stage provides the fine/precise vertical movements to the sensing chip and prism arrangement which helps to stabilize the beam spot position on the sensing chip.

A QPD is mounted to capture the reflected light intensity from the metal-dielectric interface and convert the captured light photons in terms of voltage signals which can be analyzed by the DAQ unit.

2.2.1 Novel Feedback Mechanism

Our SPR instrument is based on the Kretschmann configuration angular interrogation technique. Here, the angle of incidence is changed and the corresponding reflected intensity from the prism assembly is recorded.

The change in incident angle produces the lateral deflection (X) of the beam spot on the sensing chip (Fig. 2.19(b)). The change in reflected angle produces the deflection (Y) of the spot position at the detector unit (Fig. 2.19(b)). Therefore, the scanning mechanism without feedback suffers from the issues mentioned below:

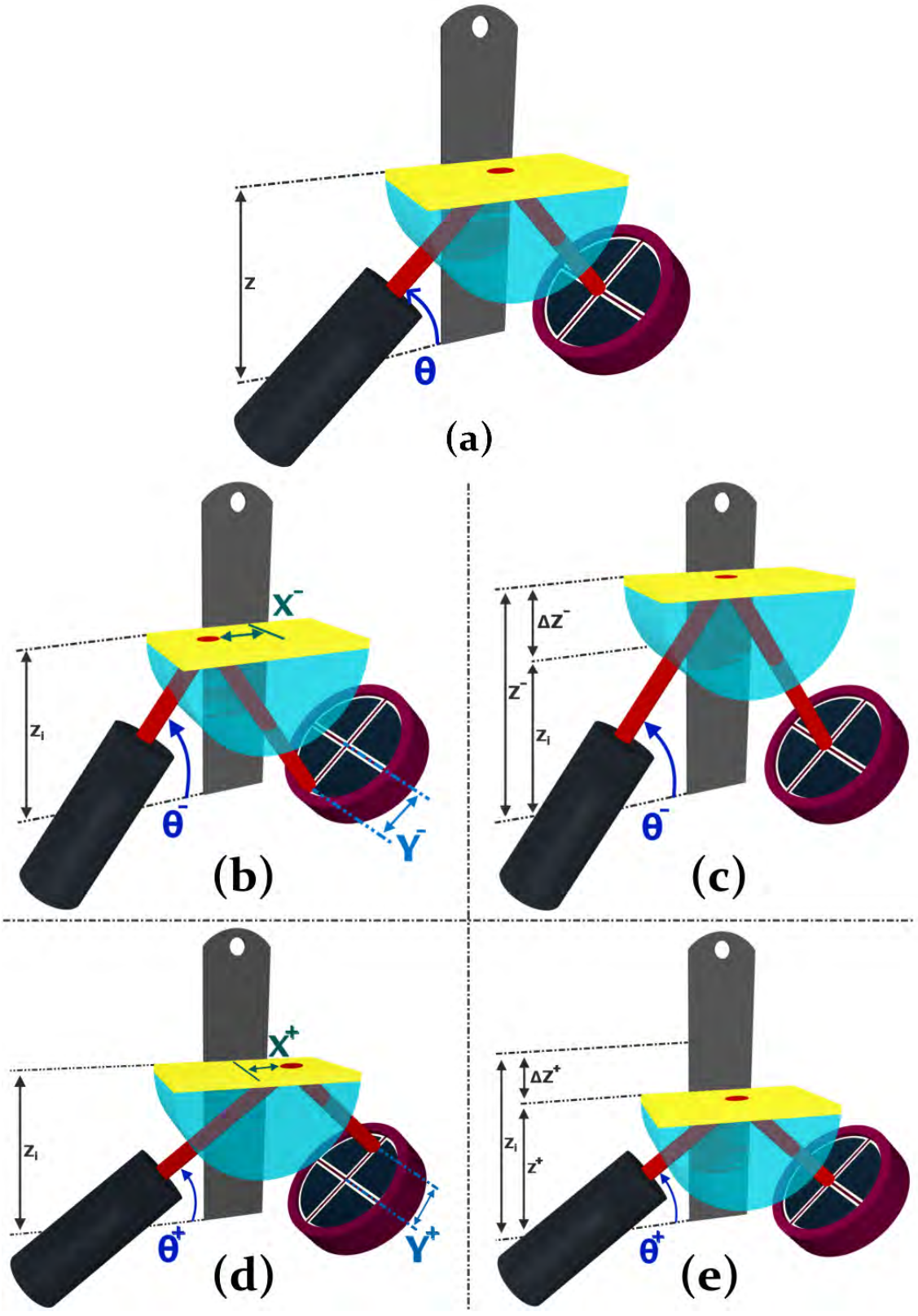

FIGURE 2.19: (a) shows the initial position of the spot at the sensing chip and the QPD. (b) shows the deflection of the beam spot for a lower angle scan (c) compensation for the lateral deflection at a lower angle. (d) shows the deflection of the beam spot for a higher angle scan (e) compensation for the lateral deflection at a higher angle.

1) The point of interrogation on the sensing chip shifts due to a change in incident angle.

2) For large-range scans, the spot moves out of the active area of the detector unit.

3) Either a bulkier optical setup is required or the SPR scan range is limited to $\sim 1-2^{\circ}$.

These technical issues create practical limitations to the utility of the equipment. In order to address these issues, a novel feedback mechanism was formulated and adopted in our SPR instrumentation.

In our SPR system, instead of a general-purpose photodetector, a position-sensitive photodetector in the form of a QPD is used. Each quadrant of the QPD acts as a separate photodiode and converts the number of photons falling on the active area in terms of voltages which are analyzed precisely with the help of the DAQ unit. The DAQ processes the difference in the total light intensity of two upper segments with the lower two segments of the QPD as shown in equation (2.1). The difference is defined as beam deflection (ΔD).

$$\Delta D = (I_A + I_B) - (I_C + I_D) \tag{2.1}$$

Where I_A, I_B, I_C, and I_D are the intensity recorded by the individual quadrants (Fig. 2.15).

The translation stage plays a significant role to compensate for the change in distance (X and Y). It is necessary to move the sensing chip either horizontally, vertically, or in a combination of both. The incorporation of horizontal translation is not suitable, as it needs more optical components which make the system larger and bulkier. An additional vertical translation is preferable which can move the sensing assembly vertically according to the value of ΔD. The direction of vertical motion e.g. up or down is dependent on the sign of ΔD.

For the lower angle scan, the spot travels a distance (X) towards the left at the sensing chip which causes the downward lateral motion (Y) of the reference spot on the active area of the QPD. This is shown in Fig. (2.19(b)). In this case, the ΔD is negative. Thus, to compensate for the -ΔD, the DAQ communicates with the translation controller unit to move the sensing assembly for a distance (ΔZ^{-}) in the upward direction.

For the higher angle scan, the spot travels a distance (X^+) towards the right at the sensing chip which causes the upward lateral motion (Y) of the spot at the active area of the QPD. This case is shown in Fig. (2.19(d)). Here, ΔD is positive. Thus, to compensate for the ΔD, the DAQ communicates with the translation controller unit to move the sensing assembly for a distance (ΔZ^+) in the downward direction which is shown in Fig. 2.19(e).

To make the observations more precise and accurate, the value of $|\Delta D|$ must be as small as possible. Thus, the SPR observations are taken only for the $|\Delta D|$ must be under the threshold value (T).

2.3 Development of GUI-based software

User-friendly GUI-based software is developed using LabVIEW software. It is designed to provide a quick response. Instead of time-consuming complicated processes, the hardware-software synchronization makes it capable to execute a full angular scan in gaseous media only in 6 to 10 minutes and approximately 20 minutes for a scan in aqueous media.

The small-size, portable software is installable and compatible with Microsoft Windows-based operating systems. The executable application software is designed with several features. It is capable of identifying the inappropriate SPR chip. It can inform about the hardware synchronization errors so that one can identify and resolve the issues easily. A software trigger for an emergency stop is also included in the software. To prevent the accidental loss of the experimental data, the software has an auto data saver function. A provision for privacy enhancement with password protection is also added. For the convenience of the user, some shortcut command keys are also integrated into the controller software (Fig. 2.20).

The front panel of the SPR controller software possesses four main tabs such as: for recording the SPR curve 'SPR curve', observing the real-time or dynamic response of the sensor 'Kinetics', to synchronize the position of the hardware system according to the application 'Positioner', and to configure the instrument for hardware-software synchronization.

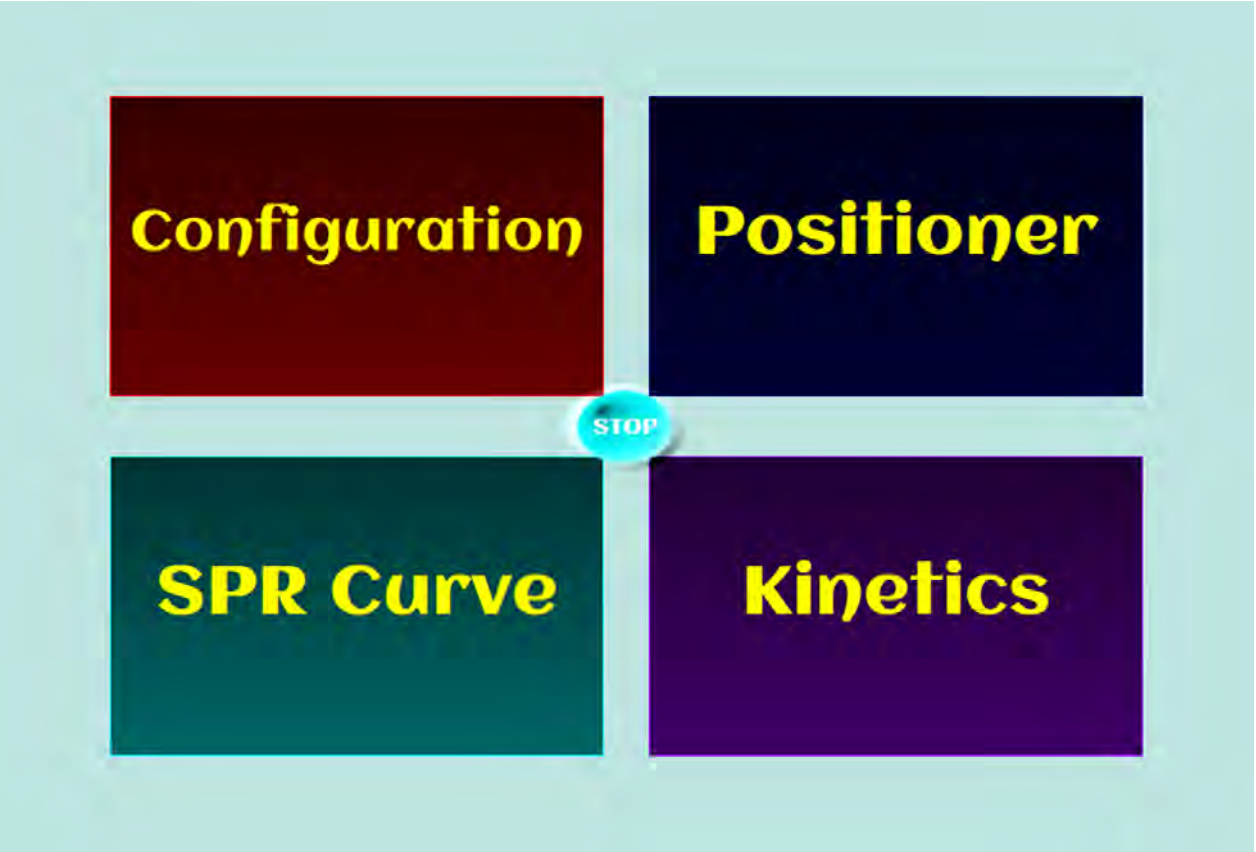

FIGURE 2.20: Front view of the controller software for our SPR sensor.

2.3.1 Configuration

The Configuration tab allows the fixing of COM-port for data communication, some commands to the laser optics, vertical translation, and the detector unit which are useful in the optical alignment for a given service mode. Fig. 2.21 shows the Configuration section.

2.3.2 Positioner

The 'Positioner' interface contains the numeric input to set the incident angle. It provides the automatic command to align the system at a specific incident angle. The interface is the pre-stage to observe the real-time measurements at a specific incident angle.

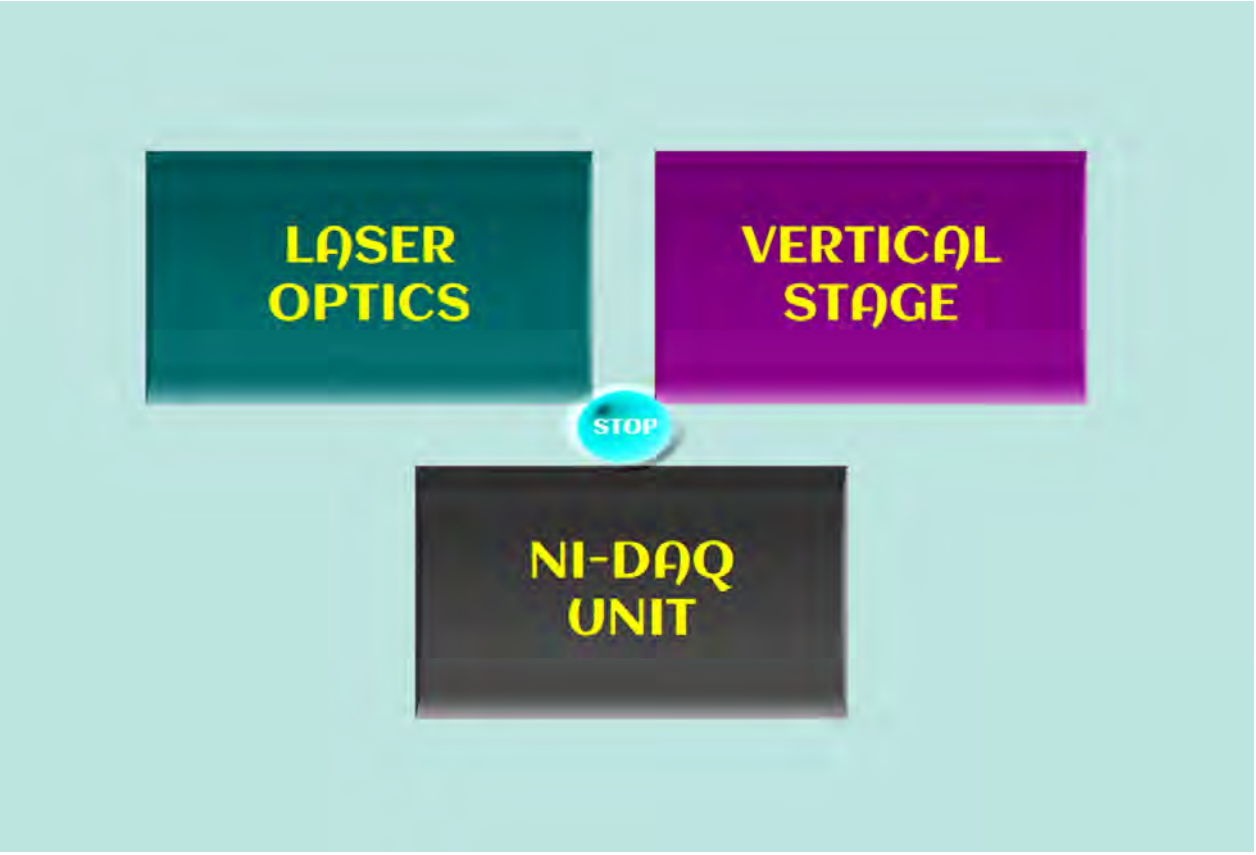

FIGURE 2.21: Configuration subsection of the controller software.

2.3.3 SPR curve

To obtain the SPR sensorgram, the interface incorporates synchronized controls for the piezomotor, translation stage, and detector system. The program code works in four steps. The three steps are calibration steps for the equipment and the last one stands for recording data. The interface for this subsection is shown in Fig. 2.22.

In the initial stage, the program initializes the hardware components to their default states. The angular scanning range can be decided between the lower limit 'L.L.' and the upper limit 'U.L.'. The 'Dirn' switch fixes the scanning direction. The 'PRST' button is to initialize the angular position of the incident beam either to 'L.L.' or to 'U.L.' according to the selected direction. The 'Reset Success' is the indicator for successful initialization of the angular position of the incident beam. The external/manual calibration in angular position (°) can be

provided by the 'PCali' numeric input. 'The 'NEXT' button is used to proceed towards the next step after the complete execution of the initial stage. The second stage automatically executes the light intensity calibration with the help of the QPD. 'Speed' is the numeric input for the translation stages speed while 'PNoS' and 'PFreq' stand for the number of steps and the frequency of the piezomotor. The next step can be processed by pushing the 'NEXT'.

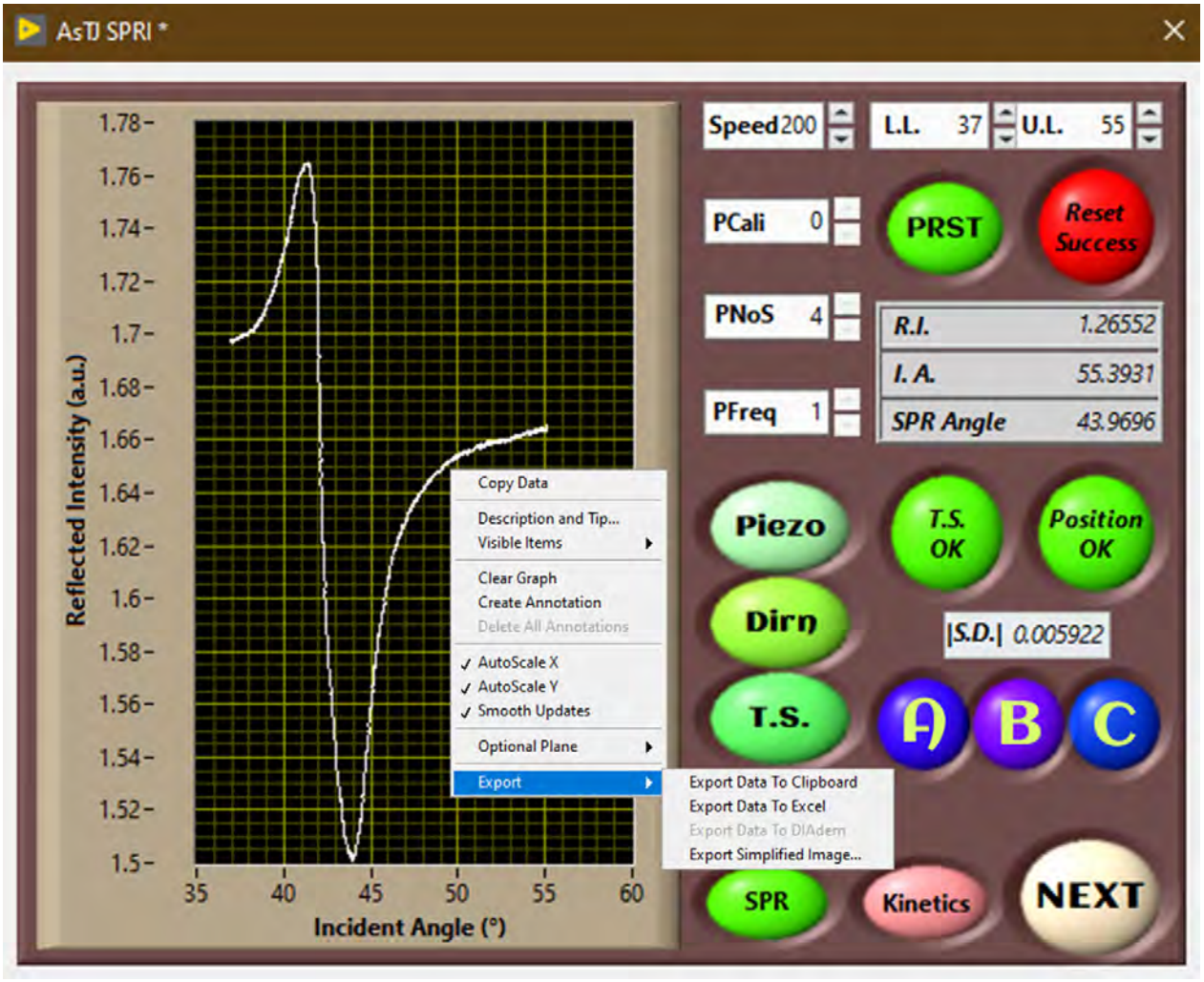

FIGURE 2.22: Subsection for the SPR curve measurement.

In the third stage, the program code switches to the translation stage to fix the beam spot at the specific position of the sensing chip. The 'T.S. OK' indicates the status of the hardware-software synchronization of the translation stage. To increase the accuracy and the precision of the observation, three accuracy indicators 'A' 'B' and 'C' are included but the highest

accuracy and precision can be ensured by the final indicator 'Position OK'. After fixation of the beam position, the equipment is ready for the observations, thus the 'NEXT' button is used to move to the SPR observations.

In the last stage, the SPR sensor-gram is recorded in a graph panel which shows the real-time observations for the SPR response. The same graph panel indicates the plot for reflected intensity (R.I.) with respect to the incident angle (I.A.) and time according to the selection of the 'SPR / Kinetics' button. '|S.D.|' indicates the accuracy of the feedback mechanism. An approximate SPR angle is indicated in the numeric indicator 'SPR angle'. The 'Piezo' and 'T.S.' are the optional controls that can be used to hold the piezomotor and the translation stage at a particular position, if necessary. The right-click on the graph panel provides the option to export the data as an excel file, clipboard, or image. Fig. 2.22 shows the GUI-based coding interface for the controller software.

Some part of the coding window in the developer mode of the controller software is shown in Fig. 2.23.

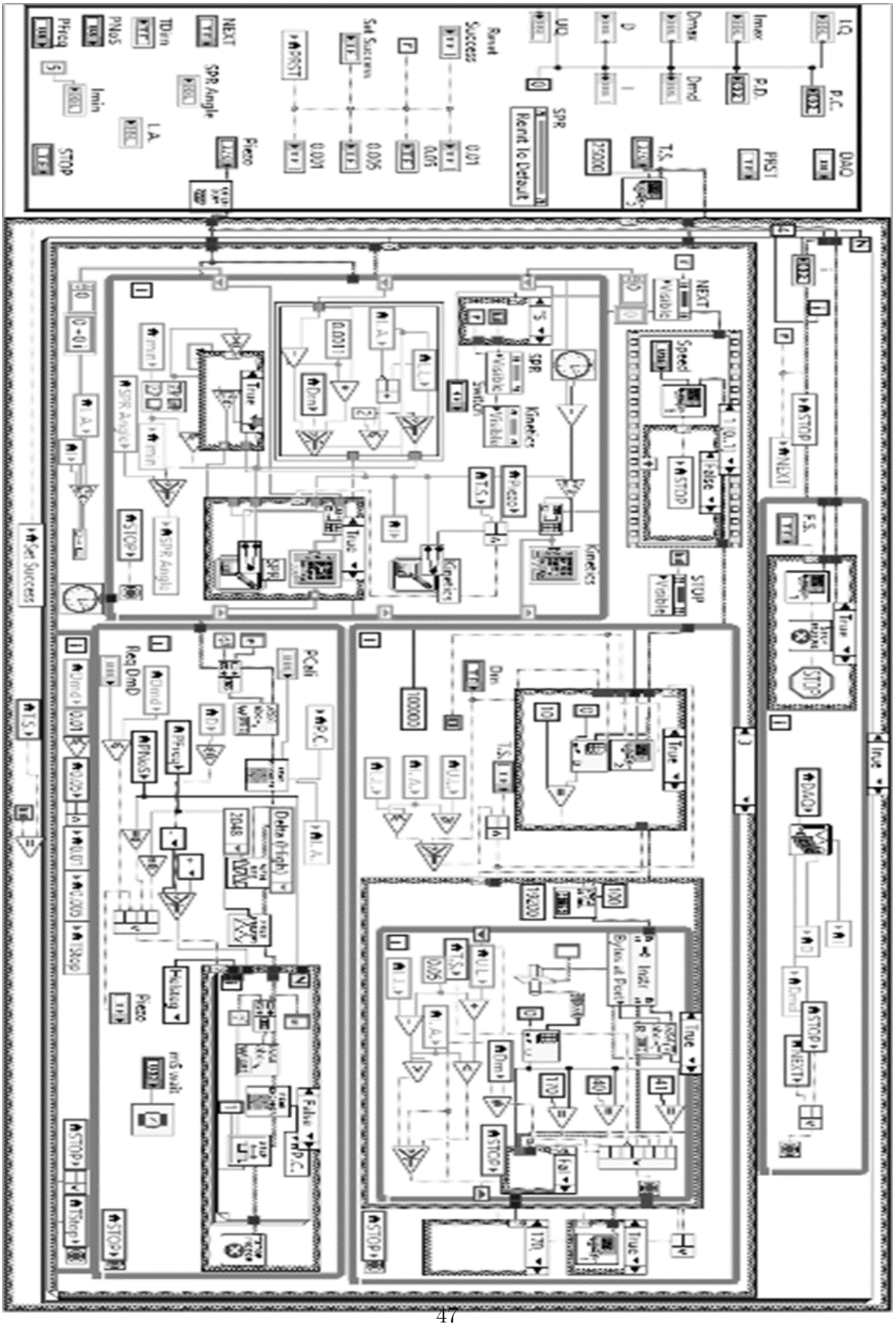

FIGURE 2.23: GUI-based LabVIEW back panel for the controller software.

2.3.4 Kinetics

The real-time measurement of SPR response at a given response angle can be obtained using the Kinetics section. The interface for the kinetics is shown in Fig. 2.24. The graph panel shows the response change in the SPR signal with respect to time. To observe the kinetics using the SPR equipment, first, the value of the SPR angle is obtained using the SPR angle section. Then the positioner tab synchronizes the hardware for the desired position. The kinetic tab is used to observe the dynamic changes in SPR response. The data can be exported with a right-click option.

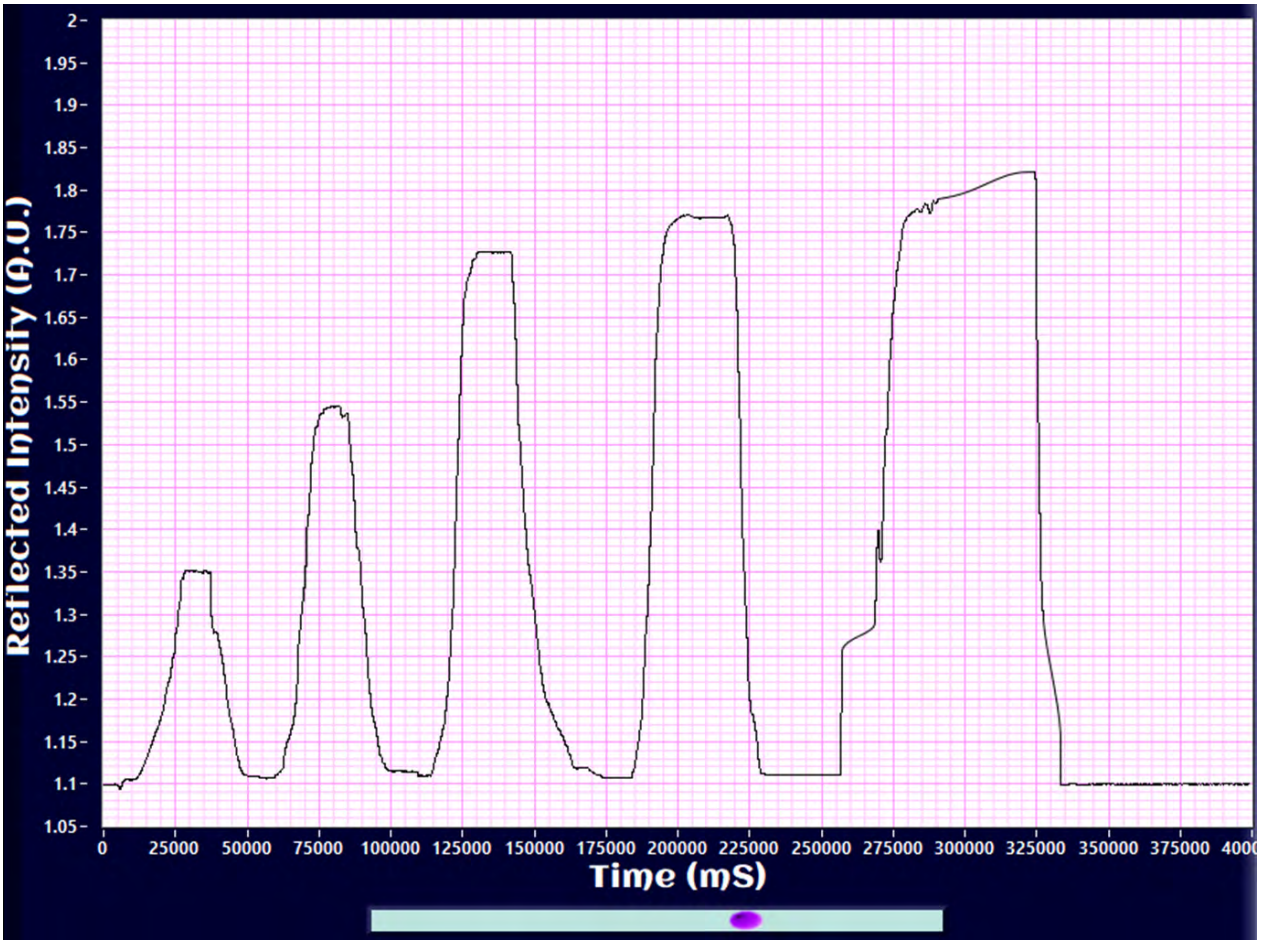

FIGURE 2.24: Kinetics interface for the SPR equipment.

2.4 SPR chip optimization

The development of an instrument needs a lot of parameters to be optimized to deliver a satisfactory performance. The performance of the SPR instrument depends on various parameters like the resolution, stability, software–hardware synchronization, noise reduction techniques, etc. Except for these, the sensing chip plays a crucial role in achieving enhanced SPR sensitivity. The SPR chip can be functionalized with a suitable material (ligands) to enhance its sensing performance. There are several ways to functionalize the SPR chip. However, due to the immobilization of bio-ligands, the thickness of the dielectric layer over the SPR chip increases, and thereby, the perceptibility of the plasmonic field reduces drastically. It can be addressed to some extent by the deposition of a single layer (ultrathin film) of ligands on the SPR chip for sensing applications. It is noteworthy that materials to be deposited in the form of the ultrathin film should be judiciously chosen such that molecular-specific interactions are prioritized during sensing applications.

The SPR phenomenon is largely depends on the metallic layer deposited on the BK7 glass plate. The SPR is very sensitive to the thickness and the nature of the metal for the generation of SPP waves. The quality of the SPR chip should be optimized with respect to the material and its thickness. In the case of localized SPR including these parameters, the optimization can be done with respect to the local structures in the metallic layer.

Such optimizations can be executed either by experimental approaches or/and by simulation techniques. The experimental procedures are costlier and time-consuming. Thus, the easy and cost-effective way of optimization is to simulate the experimental processes and obtain the best-optimized parameters for a high-performing SPR-based sensing device. The optimized parameters thus can be adopted in the actual experiments.

The Kretschmann SPR configuration can be simulated by using Fresnel's equation. Various simulation software packages viz. MATLAB, python, etc., can be used to simulate the reflected light intensity from the sequential combination of BK7, gold, and air/water with respect to the change in incident angle and the thickness of various layers of the SPR chip very precisely.

An additional layer of ligands has also been integrated with the simulation model. The reflection from the two interfaces, air/water-gold and gold-BK7, is modeled theoretically using Fresnel's equation [46, 55, 56]. The final Fresnel's equation of reflectance R_p for the p-polarized light is given by:

$$R_p = \mid r_p^2 \mid \tag{2.2}$$

where r_p is the reflection coefficient for p-polarized wave.

$$r_p = \frac{(M_{11} + M_{12}q_4)q_1 - (M_{21} + M_{22}q_4)}{(M_{11} + M_{12}q_4)q_1 + (M_{21} + M_{22}q_4)} \tag{2.3}$$

$$M_{ij} = (\prod_{k=2}^{3} M_k)_{ij} \tag{2.4}$$

For the k^{th} layer,

$$M_k = \begin{bmatrix} cos\beta_k & -isin\beta_k/q_k \\ -iq_k sin\beta_k & cos\beta_k \end{bmatrix} \tag{2.5}$$

Here,

$$q_k = (\mu_k/\widetilde{\varepsilon}_k)^{1/2} cos\theta_k \cong \frac{(\widetilde{\varepsilon}_k - n_1^2 sin^2\theta_1)^{1/2}}{\widetilde{\varepsilon}_k} \tag{2.6}$$

$$\beta_k = d_k \frac{2\pi}{\lambda} (\widetilde{\varepsilon}_k - n_1^2 sin^2\theta_1)^{1/2} \tag{2.7}$$

where, the relative permeability $\mu_k \cong 1$, θ_1 and θ_k are the angle of incidence at the interface of media 1 - 2 and (k-1)-k, n_1 is the real part of refractive index of the medium 1, $\widetilde{\varepsilon}_k$ and d_k are the complex dielectric constant and thickness of k^{th} layer, respectively [46, 55, 56].

The value of the refractive index can be calculated using a MATLAB program which is based on Fresnel's equation. The GUI-based MATLAB simulation program was developed wherein reflection from a 4-layered sequential structure of BK7 – gold – ligands – air/water was modeled. For the determination of the RI of the dielectric film deposited on the gold surface, the simulation using Fresnel's relations was used. One such SPR curve for the gold/air interface is shown in Fig. 2.25. The SPR response from the code in air and water medium is shown in Fig. 2.26.

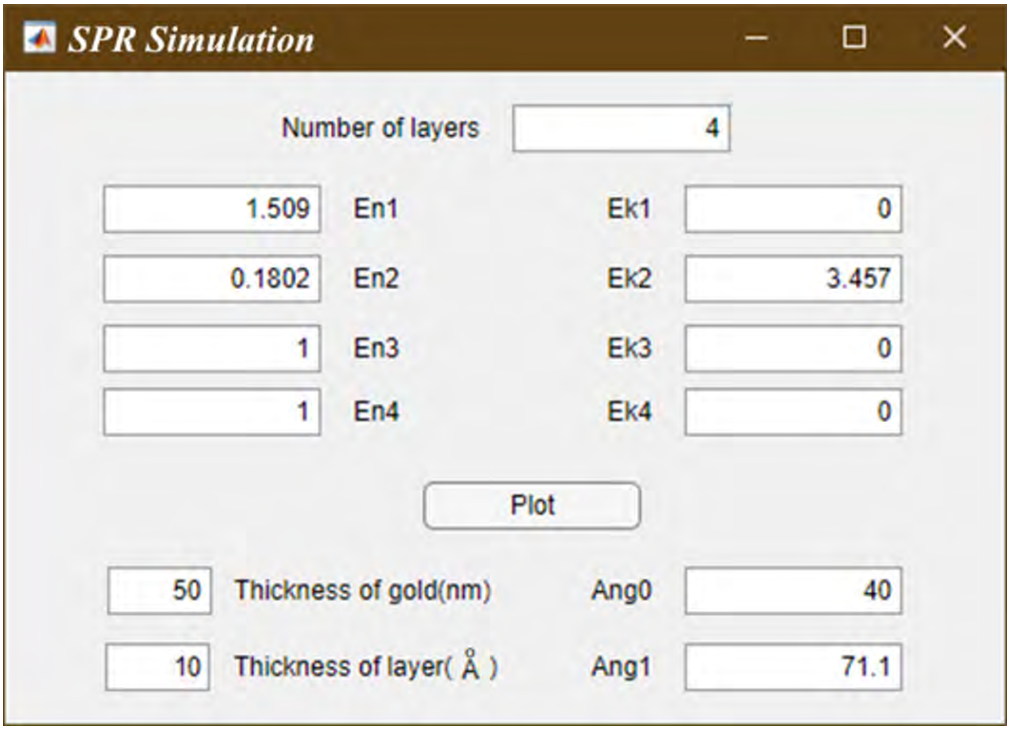

FIGURE 2.25: MATLAB SPR simulation program for refractive index calculation. Here, En_i and Ek_i are real and imaginary parts of RI for the i^{th} layer.

The mapping of the surface plasmon field over the sensing chip is essential to estimate the extent of the field, which is useful for the functionalization of the chip using suitable materials.

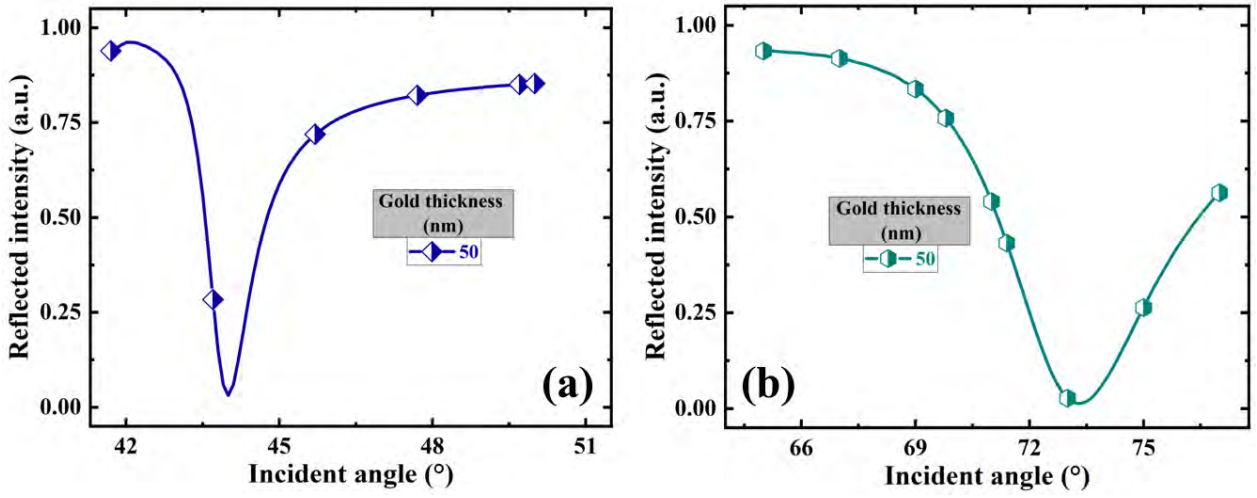

FIGURE 2.26: SPR simulation response in (a) air (b) water medium.

In bio-sensors, a stack of layers like self-assembled monolayer, passive layer, and active layers should be deposited. Often, plasmonic fields in such a stack of layers decay exponentially, which degrades the sensitivity and hence the sensing performance. The plasmonic field over the SPR chip can be simulated precisely using the Finite-Difference Time-Domain (FDTD) approach.

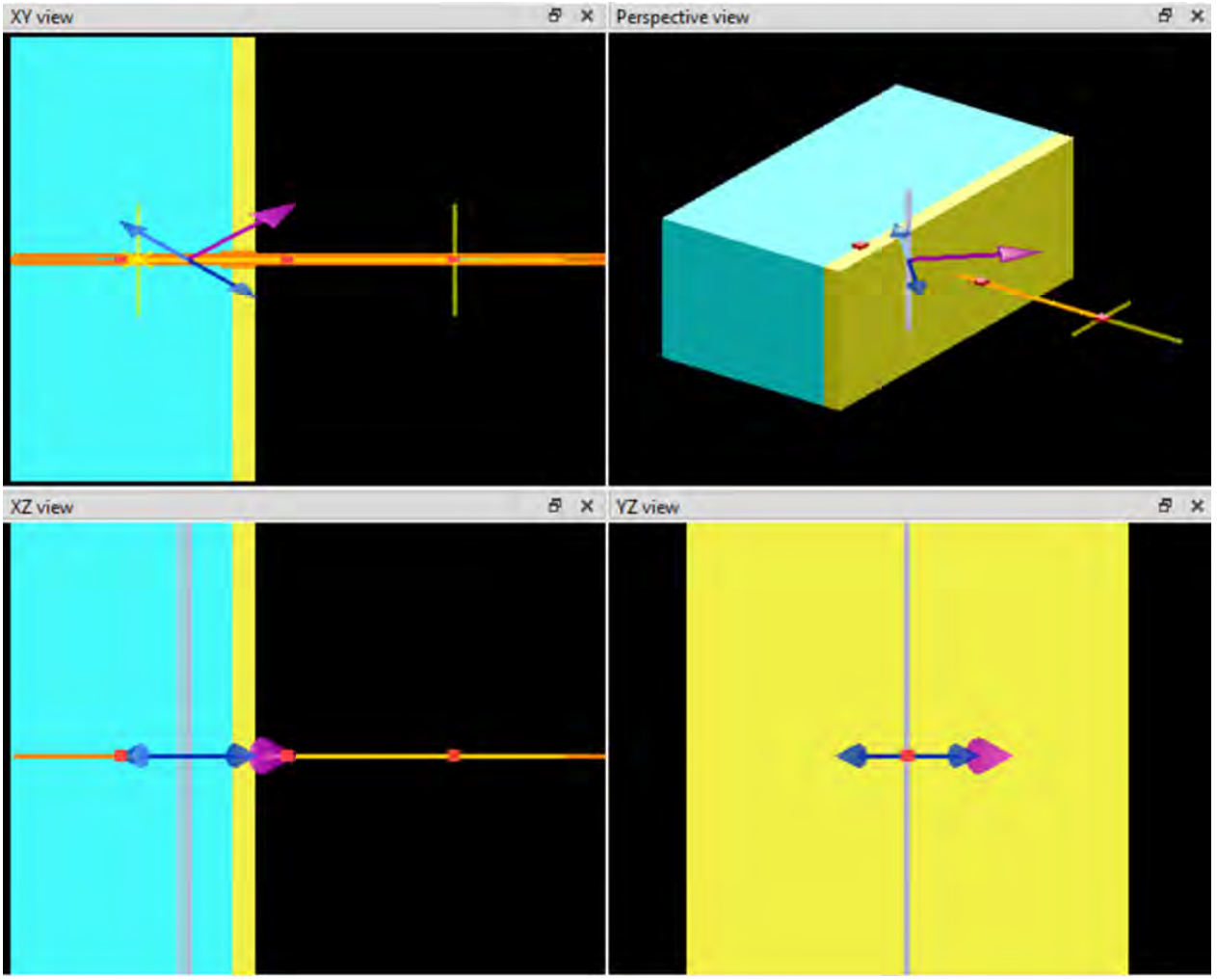

FIGURE 2.27: FDTD simulation setup for Kretschmann configuration of SPR phenomenon.

FDTD is a powerful approach for modeling nano-scale optical devices with extremely high accuracy. It solves Maxwell's equations on a mesh and computes electric field (E), and magnetic field (H) at grid points spaced Δx, Δy, and Δz apart, with E and H interlaced in all three spatial dimensions. The FDTD includes the effects of scattering, transmission, reflection, absorption, etc. The maximum task size for FDTD is limited only by the extent of

the computing power available. These time domain simulations were executed with Ansys Lumerical FDTD Simulation software which provides an easy GUI to create simulation profiles in 2D and 3D views.

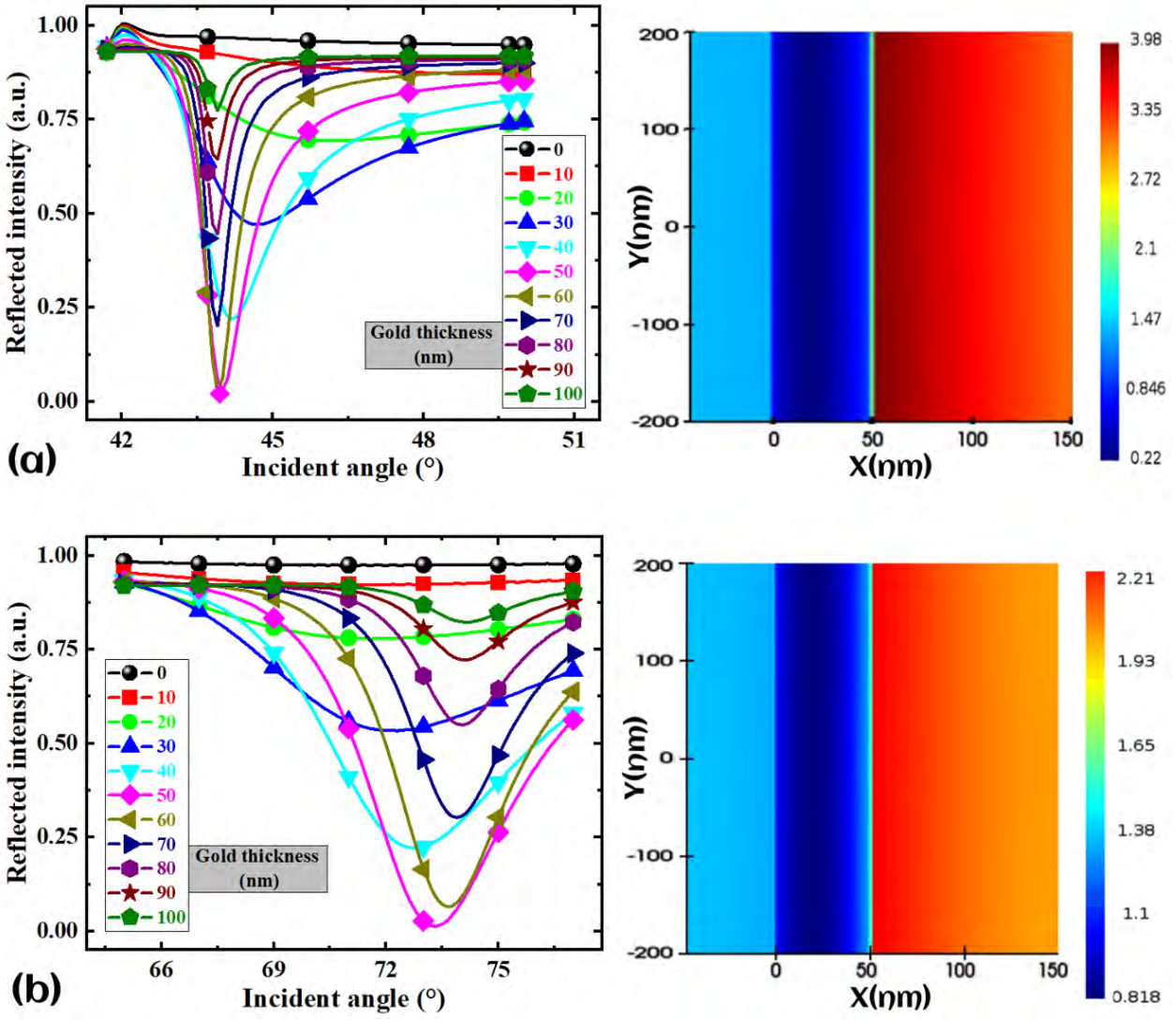

FIGURE 2.28: SPR responses obtained from the simulation for various thicknesses of gold for (a) air as a sensing medium and (b) water as a sensing medium.

The FDTD simulation model is shown in Fig. 2.27. A laser source of 635 nm wavelength was used to illuminate the metal-dielectric interface and to excite the surface plasmon polaritons (SPP). The p-polarized electromagnetic (EM) wave was propagated in the X - direction. The FDTD boundaries were used to interconnect the simulation region and outer space with some boundary conditions. The mesh region of 5 nm was used to refine the results. Transmission

and reflection monitors were used to collect the optical power transmitted and reflected from the metal-dielectric interface. The thickness of the gold layer varied in the X - direction.

Fig. 2.28(a) and (b) show the SPR curves for various thicknesses of the gold layer in air and water medium. It is observed that the highest value of Q has been found for the gold thickness of 50 nm. For this, the value of SNR is also maximum.

2.5 Calibration of the instrument

The SPR spectrum for the gold-air interface was recorded using the instrument. This is shown in Fig. 2.29(a). The resonance minimum was obtained at 44.86°. This is consistent with the reports in the literature [12,13]. The instrument was used to perform measurements in an aqueous medium. The reference curve for pure water medium shows the resonance at 70.23° shown in Fig. 2.29(b). This is also consistent with the literature [57, 58].

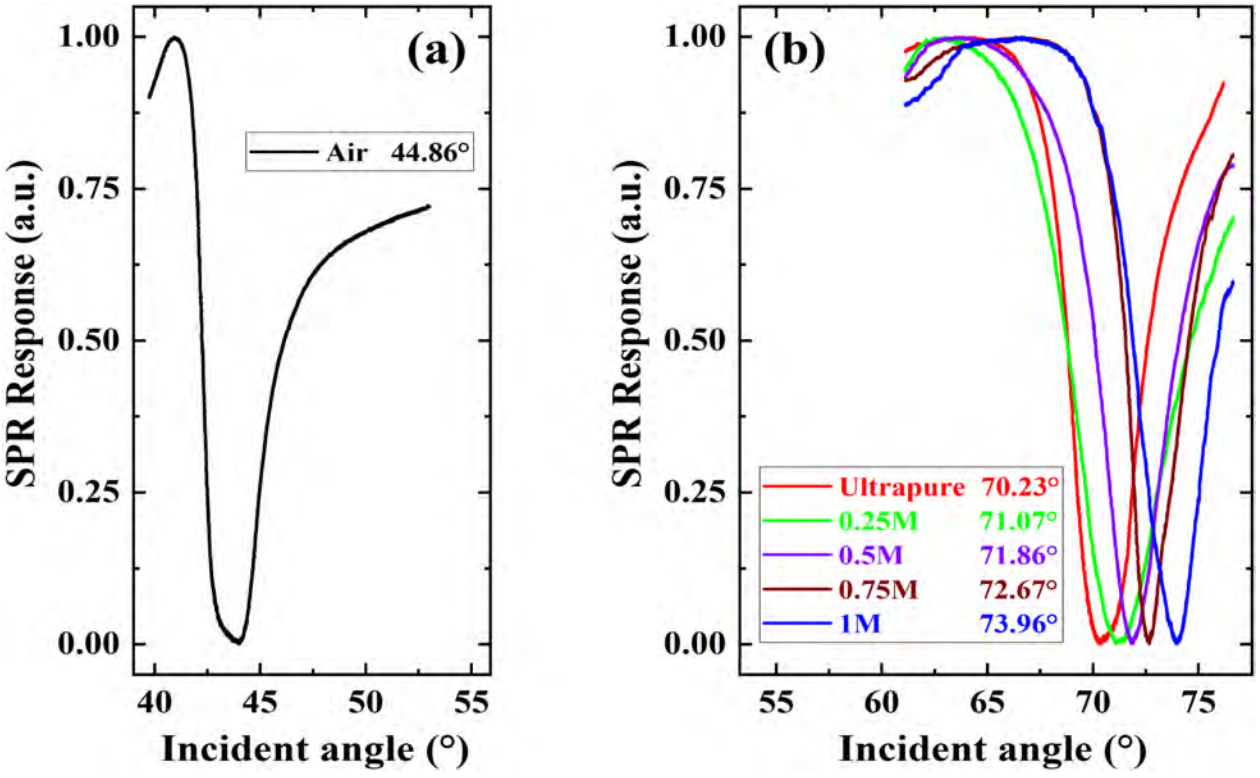

FIGURE 2.29: SPR spectrum for the (a) gold-air interface and (b) gold with various concentrations of glucose in ultrapure water.

The instrument was calibrated using an aqueous solution of glucose prepared by dissolving glucose in ultrapure ion-free water (Millipore). The SPR spectrum for different concentrations of the glucose solution is shown in Fig. 2.29(b). We obtained a systematic linear shift in the resonance angle (RA) with the change in the concentration (Fig. 2.30(a)). The refractive indices of the glucose solutions at different concentrations were obtained from standard literature [59, 60].

TABLE 2.2: calibration responses for various concentrations of D-glucose.

S.No.	Concentration(M)	RI of the glucose solution	Resonance angle(°)
1	0	1.3351	70.23
2	0.25	1.3399	71.07
3	0.5	1.3447	71.86
4	0.75	1.3496	72.67
5	1	1.3545	73.96

A calibration curve showing the RA as a function of the RI is shown in Fig. 2.30(b). The slope of the calibration curve is ∼195 °/RIU. The inverse of the slope represents the sensitivity of the SPR instrument, which is around 8 μRIU/degree.

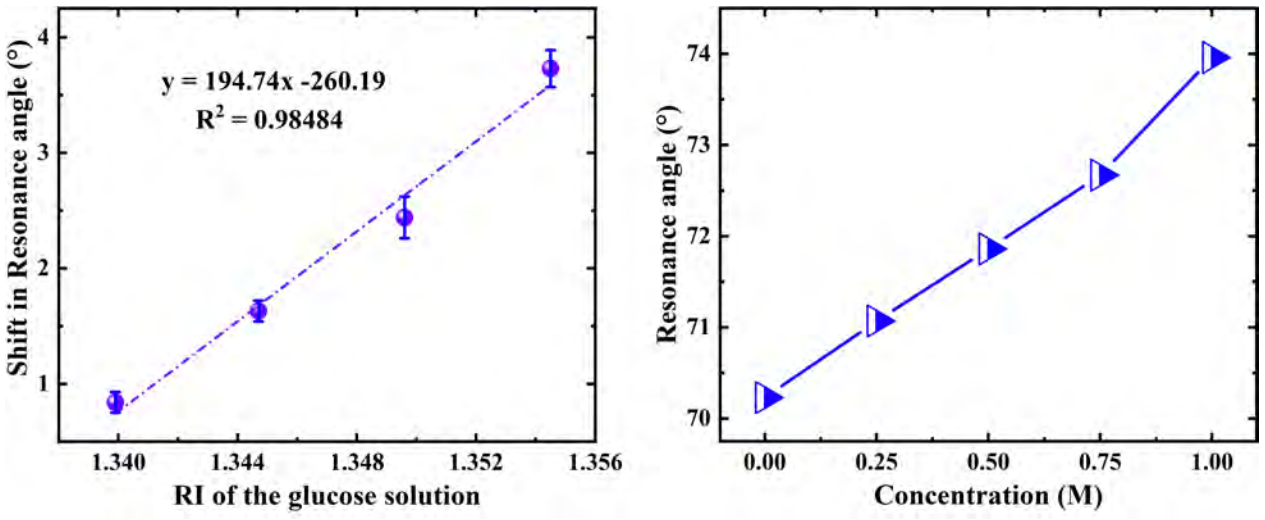

FIGURE 2.30: Calibration curves for our SPR sensor.

2.5.1 Large range scan

The traditional SPR instruments have a scan range limited to about 10 to 12°. In order to switch the measurement from one medium to another, the commercial equipment needs a complex adjustment like the change of optics, etc.

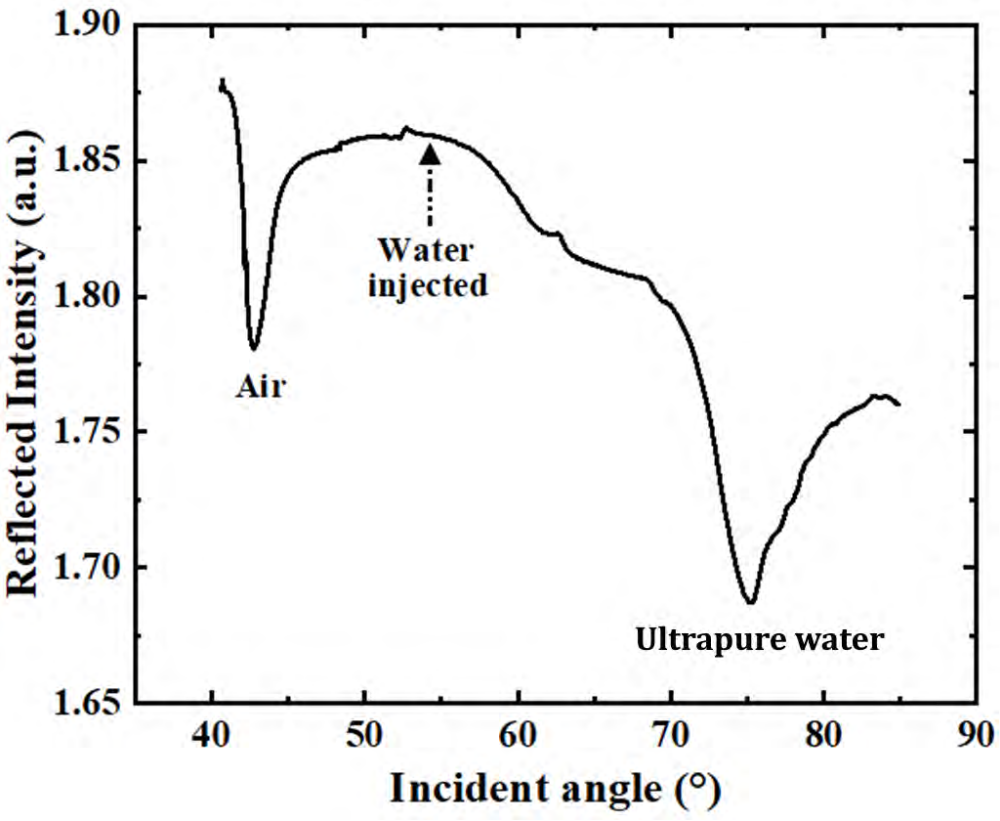

FIGURE 2.31: SPR scan for air, and ultrapure water recorded simultaneously with a single channel flow cell.

But the novel feedback approach in our SPR sensor enhances the scan range to a very large value. Our optoelectronic sensor is capable of scanning a wide range from 35° to approximately 85° without any change in optical alignments. This feature makes the SPR equipment beneficial to sense the analyte in gaseous and aqueous mediums easily. Fig. 2.31 shows the SPR scan for air and ultrapure water simultaneously scanned with a single channel flow cell. The SPR angle for air and ultrapure water are 44.66° and 74.94° respectively.

2.6 Flow Cell

Our SPR instrument is not only limited to the SPR sensorgram, but it is also compatible with real-time kinetics analysis-based applications. Some isolated flow channels can be integrated with the sensing assembly which is known as flow cells. The flow cell has a flow channel with one input end and one output end side. The channel has some open areas that can be connected with the active surface of the sensing layer for the analyte - ligand's interaction. The flow cells possess a silicone O'ring at the bottom side which ensures the leak-proof coupling of the flow cell and the sensing chip assembly.

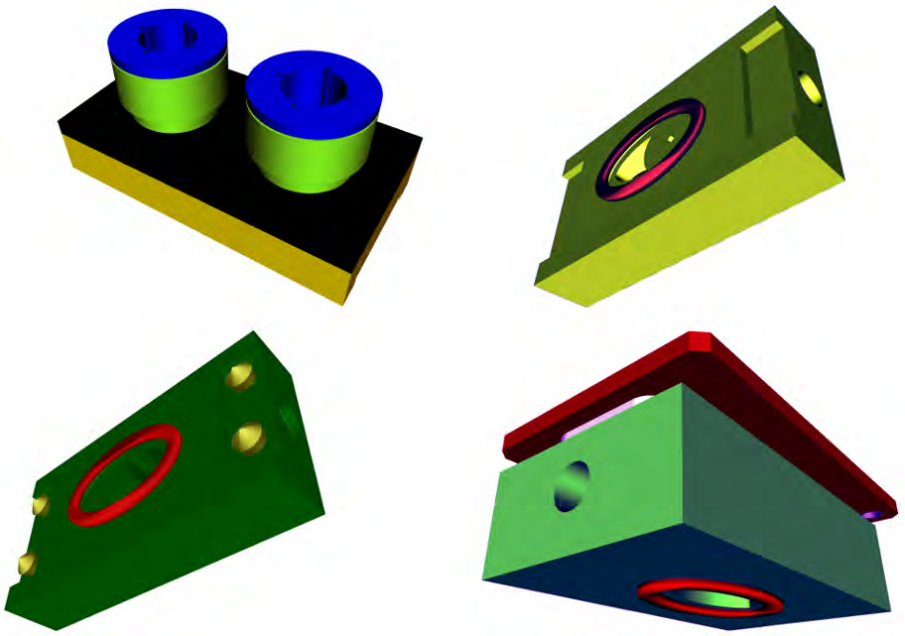

FIGURE 2.32: Various flow cells which can be integrated with our SPR sensor. (a) For gaseous analytes, (b) For aqueous medium, (c) For four-probe measurement, and (d) For humidity and temperature-based SPR observations.

Based on the optical setup of the SPR instrument, several flow cells were designed and printed using a 3D printer. The materials used for printing were Polylactic Acid (PLA) and Acrylonitrile Butadiene Styrene (ABS), which provide very high accuracy of 250 microns in their structures and good stability in aqueous/air medium. The schematic of the gas and liquid flow cells is shown in Fig. 2.32.

2.6.1 SPR sensor setup for sensing analytes in gaseous medium

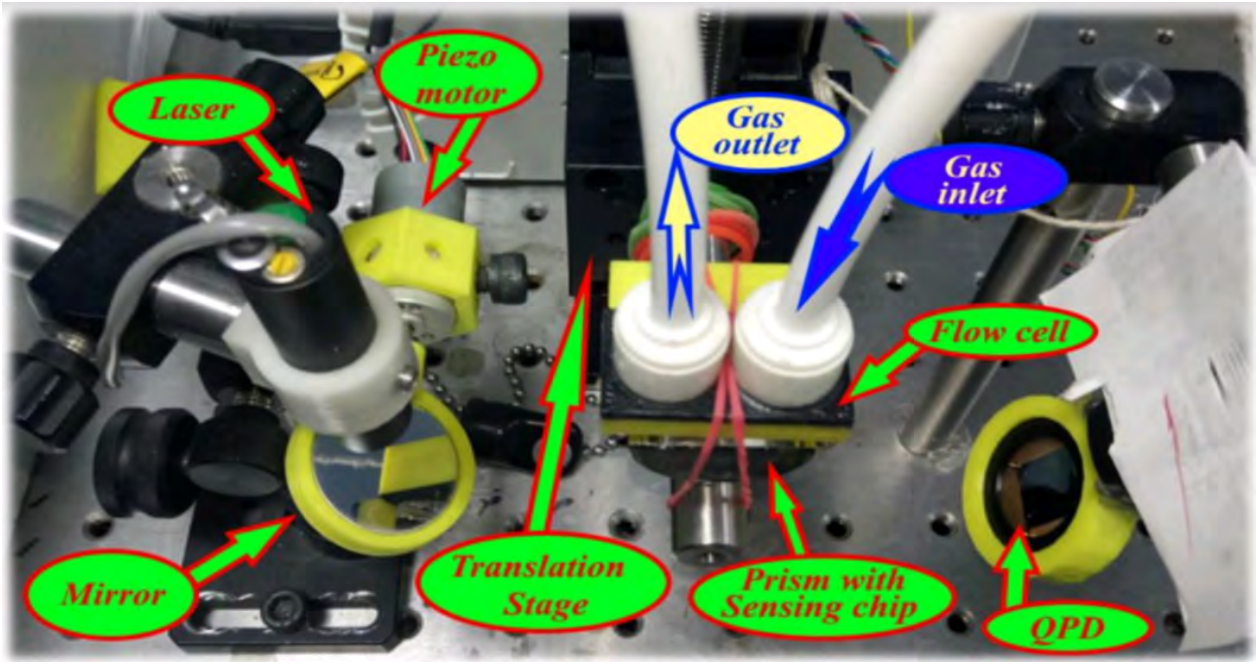

FIGURE 2.33: Actual setup for SPR equipment as a gas sensor.

Fig. 2.33 shows the actual setup for SPR equipment as a gas sensor. The gas flow cell is attached to the top of the sensing assembly. The flow cell has two valves on its top surface for gas inlet or outlet.

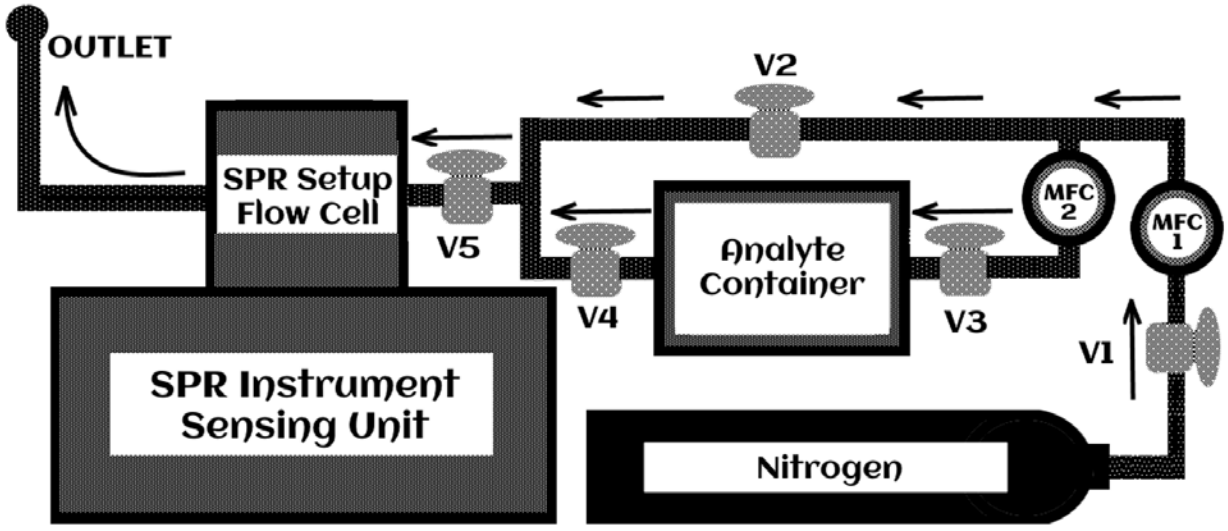

FIGURE 2.34: Block diagram of the setup of SPR-based gas sensing.

The gas inlet valve is connected to the Mass Flow Controller (MFC) units with the help of some ON/OFF valves and PTFE tubes. The schematic of the gas sensing setup is shown in Fig. 2.34.

2.6.2 SPR sensor setup for sensing analytes in aqueous medium

Fig. 2.35 shows the setup for an SPR-based sensor for measurement in an aqueous medium. The liquid flow cell is attached to the top of the sensing assembly. The two silicone tubes are fixed with their side walls to inject and remove the liquid medium. To inject the relevant solution, the inlet system is connected to the peristaltic pump which helps to maintain the flow rate of the solution on the sensing chip and helps the regeneration process for further experiment. The solution after sensing is collected in some container using another silicone tube channel.

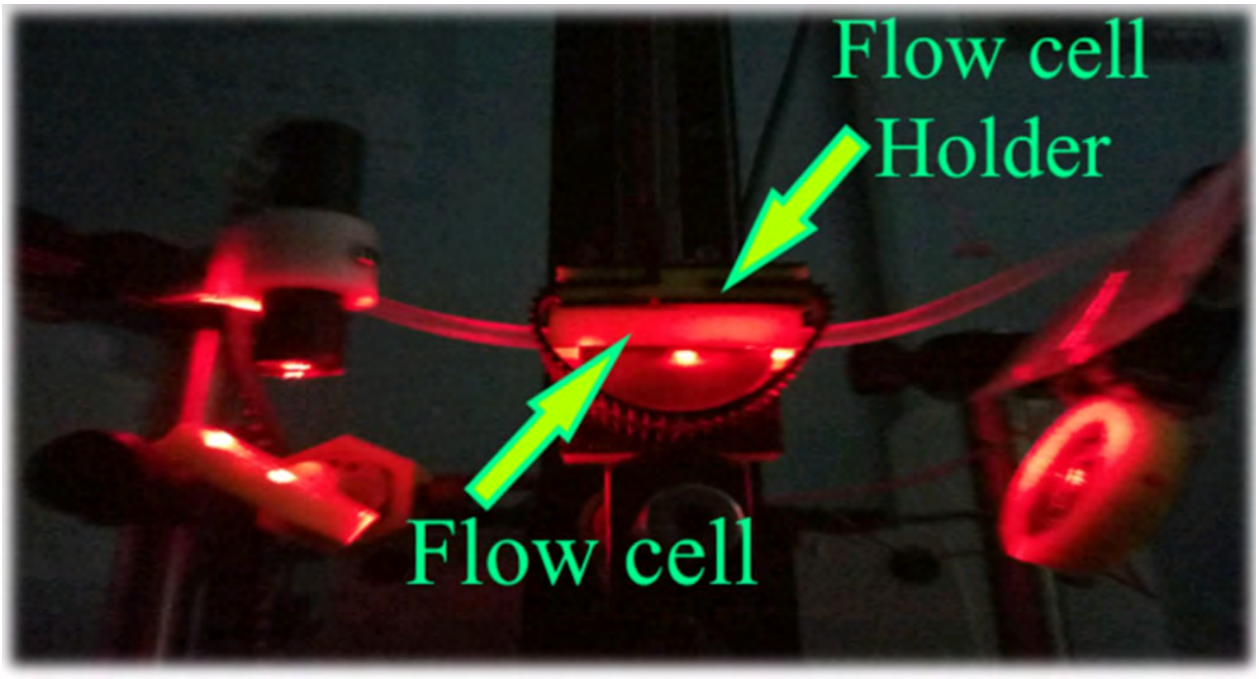

FIGURE 2.35: Actual setup for SPR equipment for sensing in liquid medium.

2.7 Scientific recommendations

Firstly, the developed SPR instrument was demonstrated at IIT Delhi in front of the scientific committee of DST India in 2018. In 2019, it was validated by three eminent scientists of the country: Prof. Ajay Agarwal of CEERI Pilani, Prof. Sandeep Kumar, and Prof V. Lakshmi Narayanan of RRI, Bangalore. The equipment was transported to RRI, Bangalore by courier, and the performance was demonstrated to the scientists. The equipment was installed on a study table, and a set of experiments were performed to show its capability. The report received from the scientists is attached in the Appendix. Some images of the demonstration are shown in Fig. 2.36.

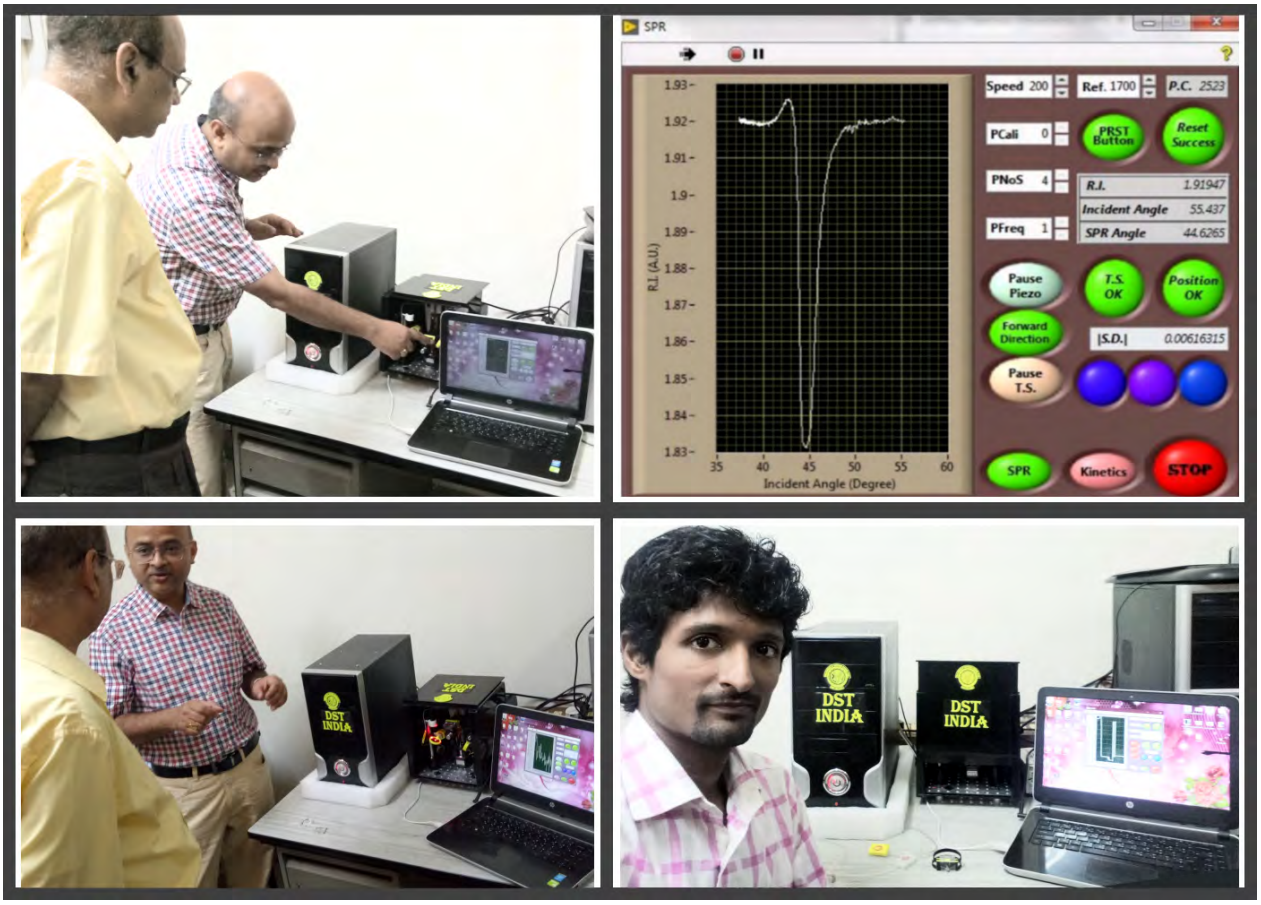

FIGURE 2.36: Some images of demonstration of our SPR sensor at various scientific institutions.

2.8 Commercialization process of OptroniX20

The equipment is ready for commercialization. In this process, we have launched a website: https://www.sprsensors.org. The website was designed by ourselves and launched on a service provider www.wix.com platform. The first page of the website is shown in Fig. 2.37.

FIGURE 2.37: First page of the website "www.sprsensors.org".

2.9 Conclusion

The developed SPR instrument is capable of performing high-end experiments related to academics or industries. The commercially available SPR instruments are complex, bulky, and costly. The novel optomechanical design has addressed all these issues without compromising its merits at international standards. There is some scope for further improvement and optimization, which can be addressed during the incubation period.

The developed SPR instrument is utilized for various traditional (sensing) and non-traditional applications (effect of polarization of external EM wave on SPR response). In this thesis, we demonstrated the sensing application of the developed SPR instrument. The instrument is used for some non-traditional applications, such as the measurement of birefringence and optical switching.

Chapter 3

Sensing application of SPR using self-assembled nanoribbons of discotic liquid crystal molecules

---

The developed SPR equipment was employed for a variety of applications. Herein, we utilized nanostructures by self-assembling organic discotic liquid crystal molecules for sensing some volatile organic compounds like ethanol and acetone using the developed SPR instrument. The supramolecular structure of the organic molecules can be perturbed easily by the application of a small force field. Triphenylene-based discotic liquid crystal (TP) molecules are rich in π-electrons which facilitate the π-stacking interaction of the molecules leading to the formation of one-dimensional nanowires. These nanowires can assemble to form nanoribbons due to a lateral cohesive force among the nanowires. The flat nanoribbons undergo a morphological transformation due to the incorporation of silver nanoparticles (SNP) into the matrix of TP molecules. The presence of SNP induces a non-chiral twisting of the nanoribbons; therefore, the flat nanoribbons transform into a helical nanoribbon structure. The global chiral structure exhibited by the composition of achiral constituents is due to the creation of topological defects like disclination and dislocation. These defects can lead to geometrical frustration in

the nanoribbons, which relaxes with the formation of twisted helical nanoribbons. A minor change in the morphology of the supramolecular assembly can have a remarkable effect on the physicochemical properties of the nanoribbons. In this chapter, we demonstrate that even a minor change in the geometry of aliphatic chains on the surface of nanoribbons can be employed for sensing organic solvents such as acetone and ethanol. The sensing was performed at room temperature. Relative humidity has no effect on the sensing response. This work is reported by us in Nanotechnology of IOP in 2020 (DOI: 10.1088/1361-6528/ab93eb) and Materials Today: Proc of Elsevier in 2021 (DOI:10.1016/j.matpr.2021.02.736).

3.1 Introduction

There are several examples in nature where molecular aggregation leading to supramolecular assembly can perform extraordinarily. Several structures due to self-assembly have been reported in the literature [61]. Among them, the self-assembly leading to one-dimensional (1D) nanowires is one of the interesting nanomaterials which offer high anisotropy in physicochemical properties. Such systems can successfully be utilized for several applications including photovoltaics, optoelectronics, semiconducting, and sensors. The nanowire viz. Carbon nanotubes, ZnO, TiO_2, gold, and silver nanotubes are widely studied [61–64]. Here, we developed organic nanowires governed by the self-assembly of discotic liquid crystal molecules in a solvent medium. In general, the discotic liquid crystal molecules exhibit delocalized π-electrons on the disc plane. Due to the $\pi - \pi$ stacking interaction between the discotic molecules, a 1D column of the molecules can be obtained. Such columns can further assemble to form various thermotropic discotic liquid crystal mesophases, e.g., discotic nematic, columnar, and hexagonal columnar phases. The columnar phase can act as an organic semiconductor wherein the charge transfer pathways can be obtained along the length of the columns. On appropriate doping, the discotic system can act as either p or n-type semiconductor [65–67]. Self-assembly of the organic molecules in the solvent medium can lead to the formation of several interesting nanostructures depending on the competing interactions between molecules. Various one-dimensional heterostructures have also been extracted from nature which has the extraordinary capabilities of molecular aggregation, which direct them

toward the supramolecular assemblies like nanowires or the helical structures like proteins, lipids, cholesterol, etc. [68–70].

The most common naturally occurring supramolecular assembly is the helix [61]. There are several biological phenomena that are governed by the helices of lipids, cholesterols, and proteins [62–64]. In general, the helical structure is induced by a chiral constituent or a mixture of chiral and achiral molecules [65]. In soft materials, e.g., liquid crystals, the competition between the local chiral interaction and the global constraints can lead to geometrical frustration which can yield a unique assembly, e.g., twisted or cylindrical structures [66–68]. Sometimes, the chiral supramolecular structures formed by achiral molecules can be induced by some external stimuli, including temperature, electric field, and polarized electromagnetic waves [69–72].

Kim et al. have reported a complete induction, control, and locking of supramolecular chiral helical nanostructure of achiral constituents by circularly polarized light in the visible range [69]. Under some constraints, it is possible to obtain the chiral nanostructure without the influence of external stimuli [73, 74]. A chiral nanostructure exhibited by achiral barbituric acid at the air-solid interface was reported [75]. This chiral nanostructure was obtained due to the H-bond network among the monolayer of achiral barbituric acid. The helical nanostructure can be obtained by incorporating topological defects, e.g., dislocation and disclination in the self-assembly of achiral molecules. These topological defects can lead to geometrical frustration in the assembly, which on relaxation, yields the supramolecular chiral nanostructure [76, 77].

In this chapter, the self-assembly of the TP molecules was facilitated, leading to the formation of nanofibers. The one-dimensional system can behave like a semiconductor. We performed a systematic electrical characterization of the nanofibers of pure TP molecules and their doping with silver nanoparticles (SNP). Interestingly, the pure and the doped nanofibers behaved like a semiconductor wherein the activation energy drops due to the insertion of SNP in the TP nanofiber matrix. The chirality in the supramolecular assembly of the achiral classical triphenylene-based discotic liquid crystal (TP) molecule was induced by incorporating achiral silver nanoparticles (SNP). The TP molecules can self-assemble into nanowires due to their

strong π-stacking interactions. Such nanowires can assemble into nanoribbons due to a lateral cohesive force [78] which is similar to that observed in the case of bundles of single-walled carbon nanotubes [79]. The presence of SNP in the nanoribbons induces topological defects, and henceforth, the system relaxes to a twisted nanoribbon structure with a Gaussian or saddle-like curvature [80].

The twisted geometry possesses a larger surface-to-volume ratio as compared to that of flat nanoribbons. The surface of the nanoribbons consists of aliphatic chains of TP molecules, each of which possesses ten -CH_2 units. The morphology of these aliphatic chains in the assembly can be perturbed by molecules of organic solvents like acetone and ethanol. A minute change in the morphology of the aliphatic chain in the nanoribbons due to their interaction with molecules of the organic solvent can create a minor change in the dielectric properties of the nano-system. Such a minor change is measured using a surface plasmon resonance (SPR) instrument. Our studies reveal a minor change in the morphology of a nano-system due to its interaction with analytes that can be effectively employed as a sensing mechanism.

3.2 Experimental Procedure

The triphenylene-based discotic liquid crystal (TP) molecules were synthesized in the laboratory [81]. The molecular structure of the TP molecule is shown in Fig. 3.1.

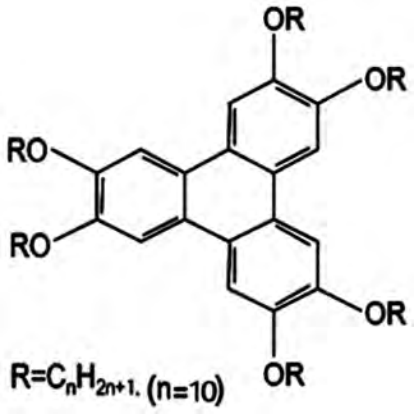

FIGURE 3.1: Chemical structure of the triphenylene-based discotic liquid crystal (TP) molecule.

The high-performance liquid chromatography (HPLC) grade chloroform, absolute ethanol, and acetone were obtained from Merck. A 10 mg/ml clear solution of the molecule was prepared in the chloroform solution. About 10 ml of absolute alcohol was poured into the chloroform solution. The TP molecules were self-assembled at the chloroform-alcohol interface and formed nanofibers in the form of cloudy material. The nanofiber synthesis is shown in Fig. 3.2.

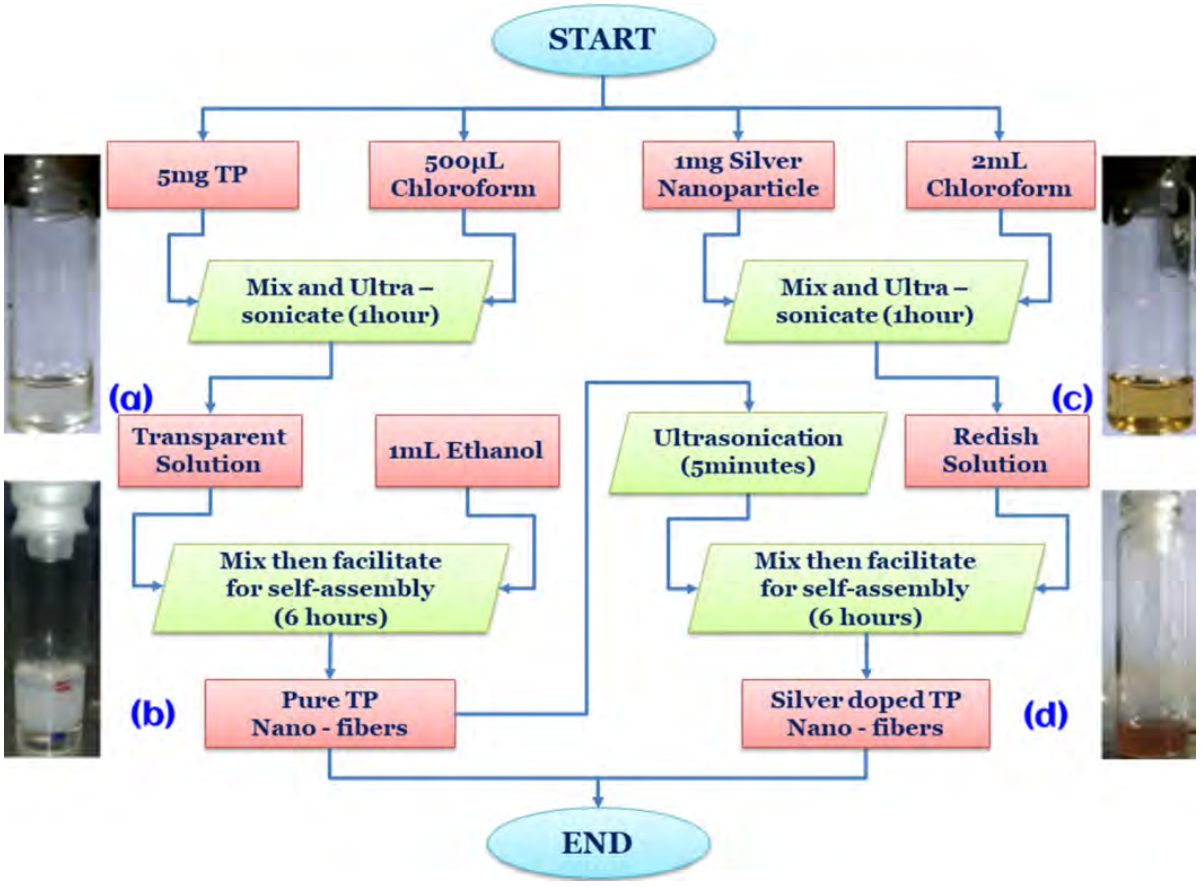

FIGURE 3.2: Synthesis procedure for pure and silver nanoparticles (SNP) doped TP nanofibers.

The silver nanoparticles (SNP) were synthesized using the standard chemical protocols [82]. The nanoparticles were protected against coagulation by functionalizing them using hexane-thiol. The size of the nanoparticles was around 2–3 nm [82]. The nanoparticles were incorporated into the matrix of nanoribbons consisting of TP molecules by dispersing them into the same chloroform solution at different weight percentages.

The fibers were spread by a drop-cast method onto the solid substrates viz. silicon wafers, glass plates, and interdigitated electrodes (IDE) to form a very thin film. In the drop-cast method, the solution of the sample was allowed to flow down under gravity from the surface of the substrate leaving behind a very thin layer of the material. The nanofiber deposition with drop-casting is shown in Fig. 3.3.

The nanofibers on the substrates were observed using optical microscopy (OM) in transmission mode at various magnifications from 5X to 40X. To observe nanofibers at a lower length scale, Atomic Force Microscopy was performed in both contact and semi-contact mode using Si-tips of spring constant k = 28.3 N/m and resonant frequency f = 438.8 KHz. The morphology of the assembly was obtained using a field emission microscope (FESEM) with an operating voltage of around 10 kV and magnification of 30 000X (FEI, APREO).

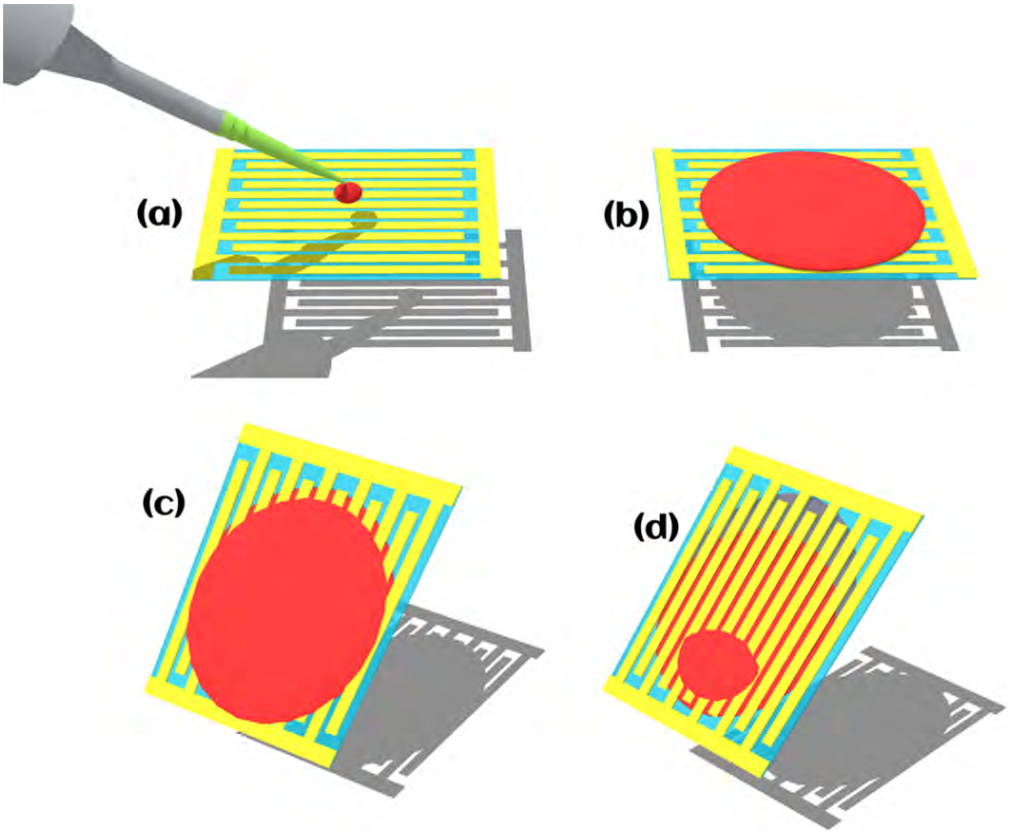

FIGURE 3.3: Deposition of TP nanofibers on an IDE using a drop-casting process.

Electrical characterizations of the nanofibers in pure and doped states were performed using

a lab-developed setup. The nanofiber deposited IDE was inserted in a homemade computer-controlled heating stage which can perform in the temperature range from 30°C to 90°C with a resolution of 0.1°C. A silicone rubber heating element and a Resistance Temperature Detector (RTD) unit were connected with a programmable power supply (APLAB) and a digital multimeter (Keithley 2400 series), respectively. A PID-controlled LabView program was developed to control the temperature of the heating stage. The schematic diagram for the experimental setup for the electrical characterization is shown in Fig. 3.4.

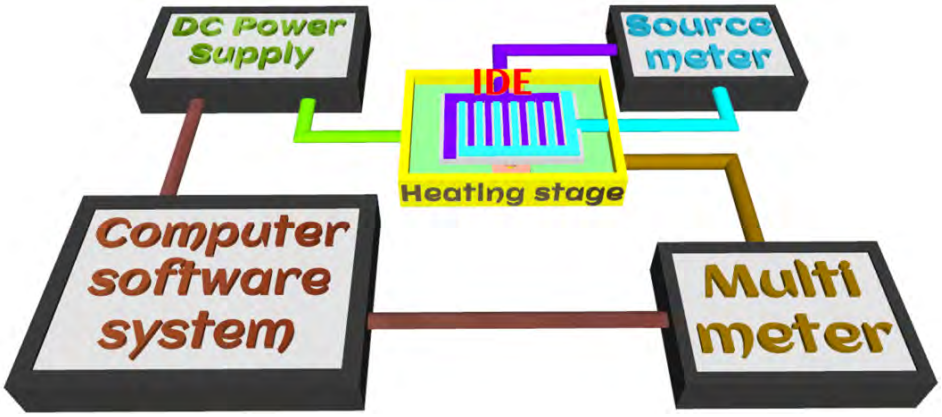

FIGURE 3.4: Schematic diagram of the experimental setup for the electrical characterization.

The sample deposited IDE was connected with the multimeter using thin copper wires. To establish the electrical connections properly, the silver conductive paste was applied at the junction of the IDE and the copper wire and dried for 1 hour. The IV measurement on the nanofibers was recorded by applying a bias voltage range from -10 V to +10 V at a step of 0.005 V. The temperature varied from 42°C to 90°C in the steps of 4°C.

For SPR measurement, a $\sim$ 3 nm Cr layer followed by a 50 nm thick gold film was deposited onto a BK7 glass substrate (refractive index = 1.51) using a sputtering deposition system (QUORUM). The drop-casted thin film of fibers was prepared on such substrates. The SPR spectra were obtained using a home-built instrument by recording reflected intensity as a function of the angle of incidence [46].

A gas - sensing setup was developed [83] and integrated with the SPR instrument. The saturated vapor of solvent (acetone or ethanol) was mixed with a carrier gas (N_2) in the

desired proportion using two mass flow controllers (Alicat Scientific) to obtain the required ppm of the molecules [84]. Fig. 3.5 shows the SPR instrument as a gas sensor.

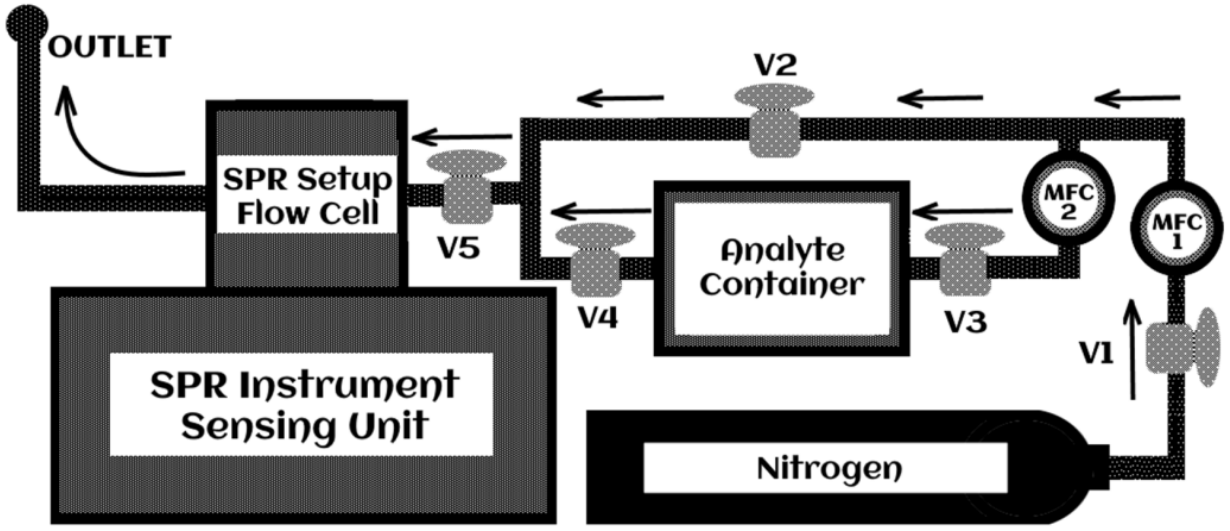

FIGURE 3.5: Gas sensing setup integrated with the SPR instrument.

The relative humidity was measured near the sensing layer ($\sim$ 0.5 mm above) by integrating an Arduino-based humidity sensor (DTH11) in a 3D - printed flow cell. All the experiments were performed at room temperature, i.e., 24.0 $\pm$ 1 °C.

3.3 Results and discussion

The optical micrographs of drop-casted film of nanofibers are shown in Fig. 3.6. The images were captured at two different magnifications. The images show a nice formation and distribution of the nanofibers.

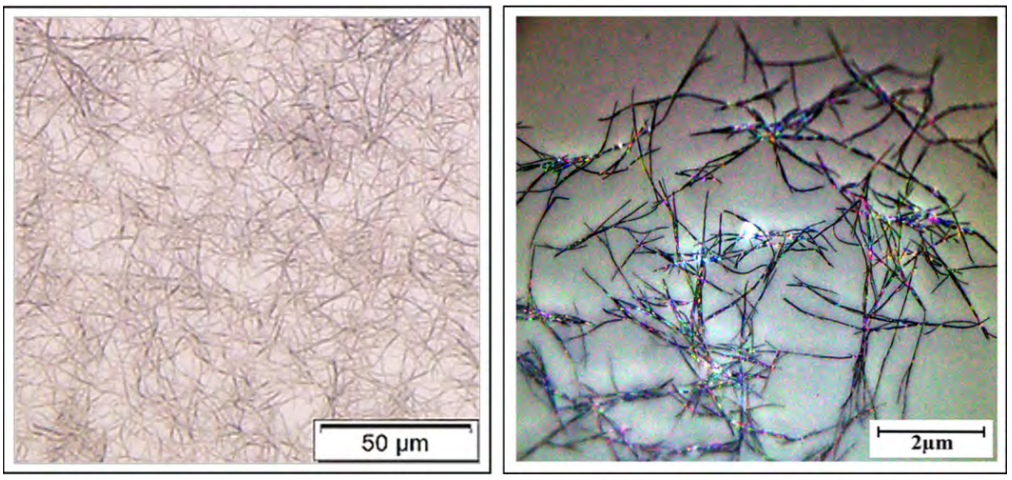

FIGURE 3.6: The optical microscopy images of nanofibers drop-casted on a glass substrate.

The atomic force microscope (AFM) images of the nanoribbons are shown in Fig. 3.7. The morphology in the three images in Fig. 3.7 is consistently scaling as per the scan length during AFM imaging. The patterns reveal more like fibers than that nanoribbons. This is due to the long-range Van der Waals interaction between the tip and the molecules leading to a smoothing effect on the edges of the nanoribbons.

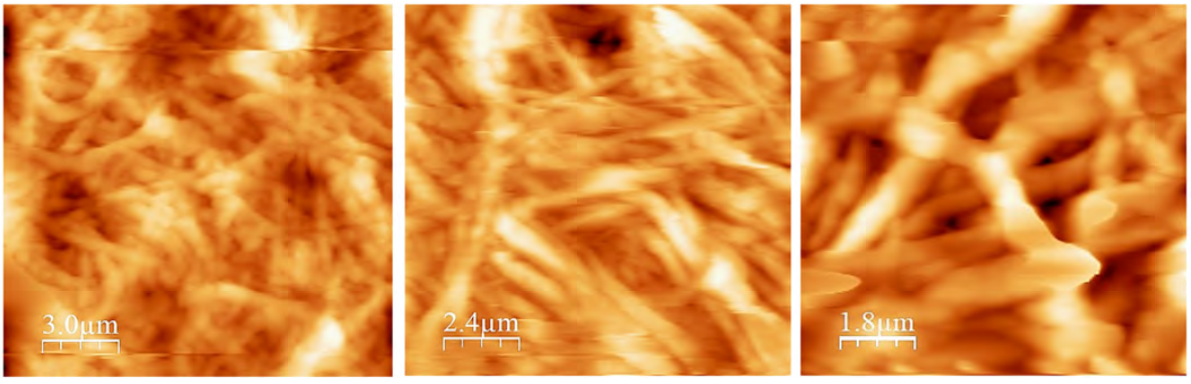

FIGURE 3.7: Atomic force microscope images of the drop cast film of the nanofibers at different length scales.

The nanofibers were drop-casted on the IDE for their electrical characterization. The optical micrographs of the nanofibers spread on the IDE and between the gaps of the IDE's finger are shown in Fig. 3.8. A nice distribution of the nanofibers can be seen from the image. The presence of the nanofibers can be verified in Fig. 3.8(b).

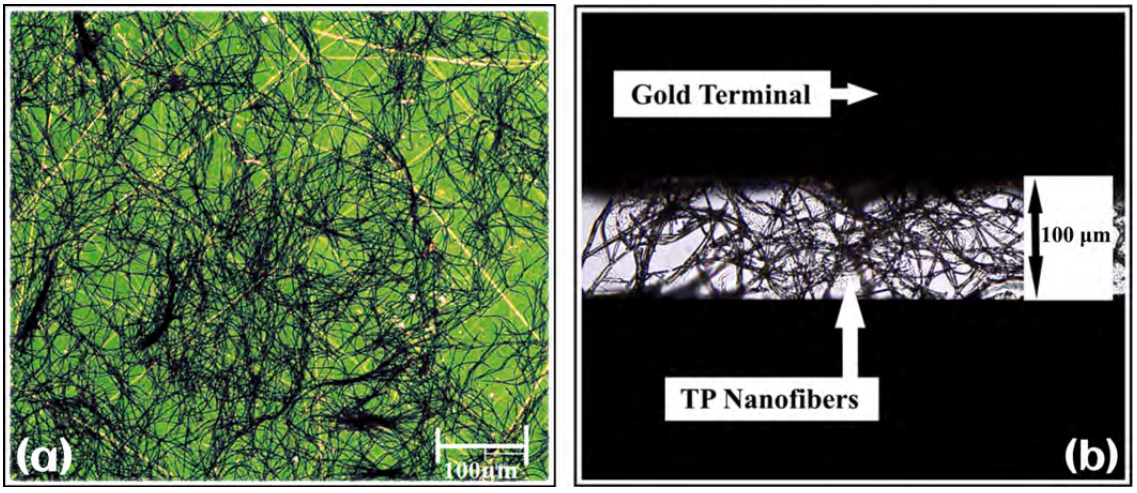

FIGURE 3.8: Optical micrographs of the nanofiber spread over an IDE at (a) contact pad and (b) between the IDE's finger.

The current-voltage (I-V) characteristics curves of the TP nanofibers were obtained at different temperatures and are shown in Fig. 3.9(a). The characteristic curves of the nanofibers show the bidirectional non-linear relationship for the applied voltage range of ±10V, which is the signature of a semiconducting behavior in the chosen voltage range.

The I-V characteristics for the 0.1, 0.2, & 0.5 wt% silver nanoparticles doped nanofibers as a function of temperature are shown in Fig. 3.9(b), (c), and (d), respectively. For the SNP doped nanofibers, the I-V characteristics are bidirectional & linear (like a low-value resistor), which indicates the Ohmic behavior of the doped nanofiber system.

In all the cases of pure and doped nanoribbon systems, the conductivity increases with the temperature, which indicates a classical semiconducting behavior. For silver nanoparticles doped and undoped nanofibers, the I-V curves are symmetric in the first and third quadrants, which indicates a very low amount of electric charge reminiscence. The 0 A current at 0 V indicates the passive nature of the nanoribbons. The Arrhenius plots are fitted satisfactorily with linear curves, which indicate the charge transfer due to the hopping mechanism [75].

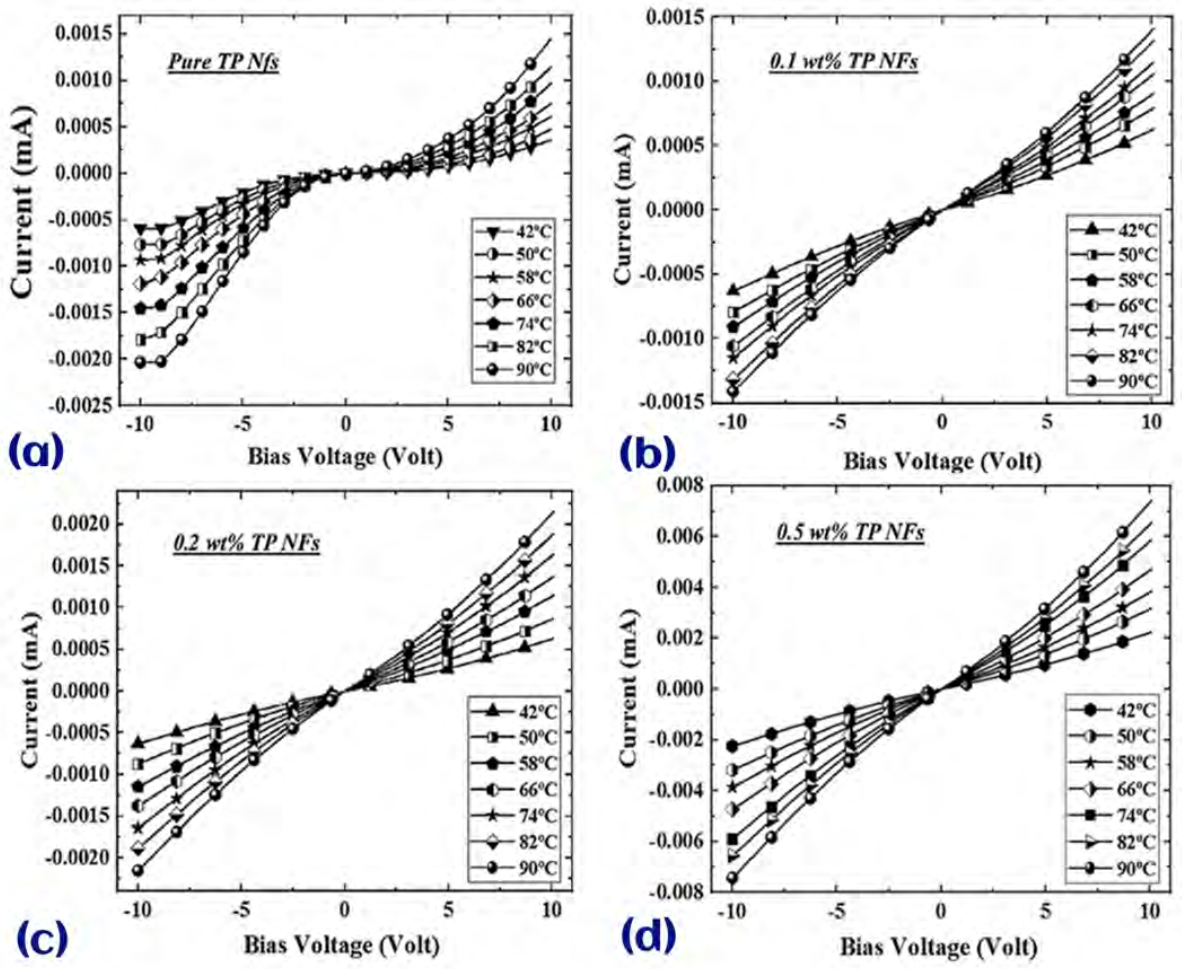

FIGURE 3.9: The current-voltage (I-V) characteristics curves recorded at different temperatures for (a) pure TP nanofibers, and (b), (c) and (d) 0.1, 0.2, & 0.5 wt% silver nanoparticles doped nanofibers, respectively.

The activation energy (E_A) of doped and pure nanoribbons is calculated from the Arrhenius plot of Fig. 3.10(a) and is shown in Fig. 3.10(b). The E_A drops more than 50% due to doping of silver nanoparticles of even 0.1 wt% as compared to pure nanoribbons. The E_A increases with a further increase in the concentration of silver nanoparticles as compared to that of 0.1wt%. There is an overall decrease in E_A due to doping as compared to pure nanoribbons.

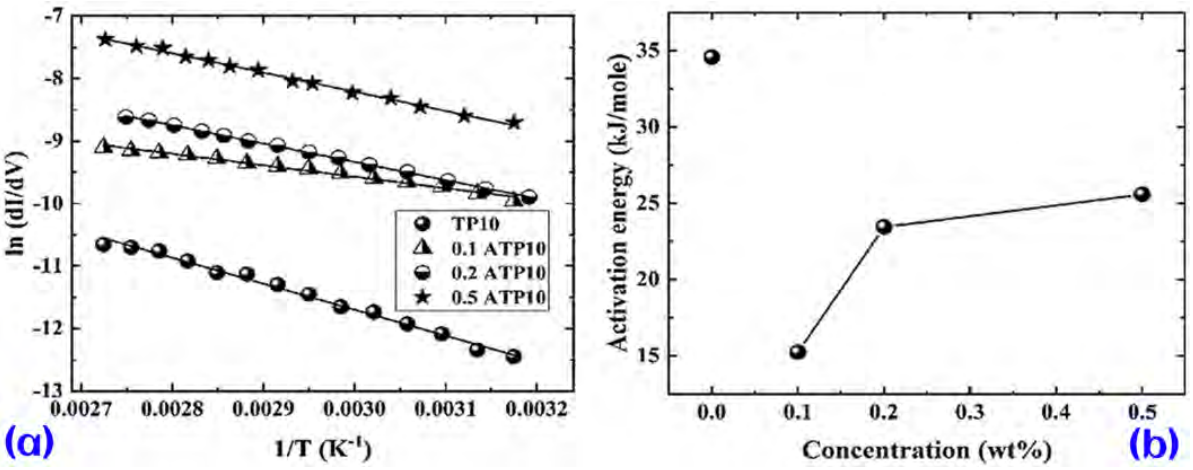

FIGURE 3.10: (a) Arrhenius plot (b) The activation energy (EA) of doped and pure nanofibers.

The FESEM images of the assembly of TP molecules are shown in Fig. 3.11. The image in Fig. 3.11(a) shows some flat strands of fibers. These are strands of nanoribbons. The width of the nanoribbons lies in the range of 50–110 nm. An observation of the scaled image in Fig. 3.11(b) shows very thin ribbon-like layers which are wound together into a structure resembling a spring onion. Thus, a more clear structure of the assembly of the TP molecules is like nanoribbons.

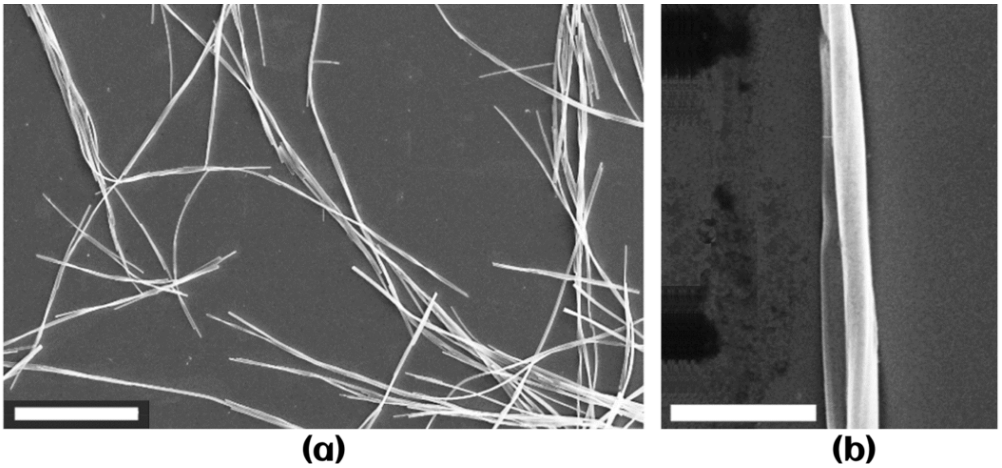

FIGURE 3.11: The field emission scanning electron microscope (FESEM) images showing the nanoribbons of TP molecules. The scale bar in (a) and (b) represents a length of 20 and 2 μm, respectively.

The SNP was incorporated into the matrix of the nanoribbons at three different weight percentages, and the FESEM images were obtained. The 0.1 wt% SNP incorporated nanoribbons are shown in Fig. 3.12. The twisted nanoribbon structure can be seen in the images. The twisted structure exhibits a Gaussian or saddle-like curvature. The average pitch of the helical structure is found to be around 1200 nm. The helical structure exhibits both left and right-handedness and they are shown enclosed in rectangles with dash and dotted boundaries, respectively. Fig. 3.12(b) depicts one strand of twisted nanoribbons wherein both handednesses, can be observed. Since the twisting is induced by the nonchiral dopants, the handedness of the obtained chiral structure is the mixture of right and left-handed nanoribbons.

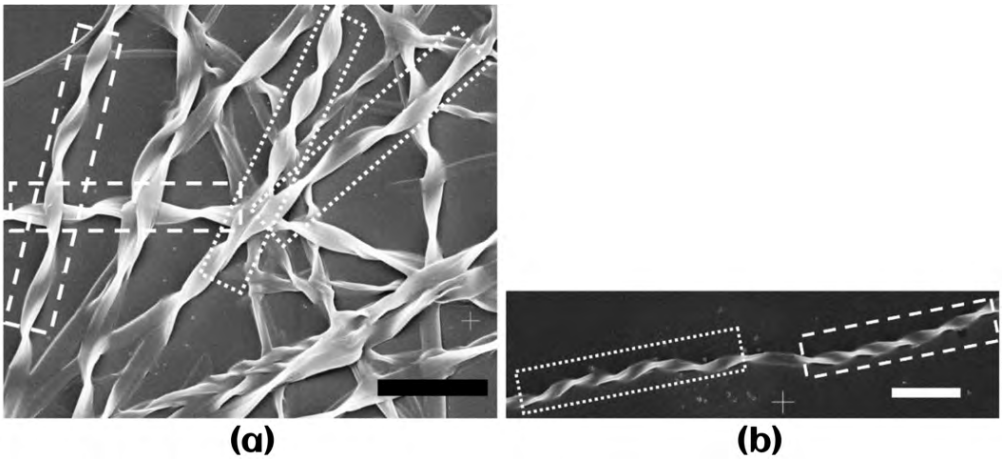

FIGURE 3.12: The field emission scanning electron microscope images show the twisted nanoribbons due to the incorporation of 0.1 wt% of SNP. The twisted nanoribbons inside white rectangles with dash and dotted boundaries exhibit left and right-handed nanoribbons, respectively. The scale bar represents a length of 3 μm.

The morphology of the supramolecular assembly of TP molecules with a higher concentration of SNP is shown in Fig. 3.13. With the increase in the concentration of SNP, the morphology of the twisted structure continues to exist. The further increase in a concentration greater than 0.5 wt% leads to phase separation of the nanoparticles. Similarly, a concentration less than 0.1 wt% of SNP does not induce the twisting in the nanoribbons. The average pitch of the helical structure for the compositions with 0.2 and 0.5 wt% of SNP is found to be around 2000 and 2400 nm, respectively. Thus, the value of pitch is found to increase with the concentration of the SNP in the matrix of the TP molecule.

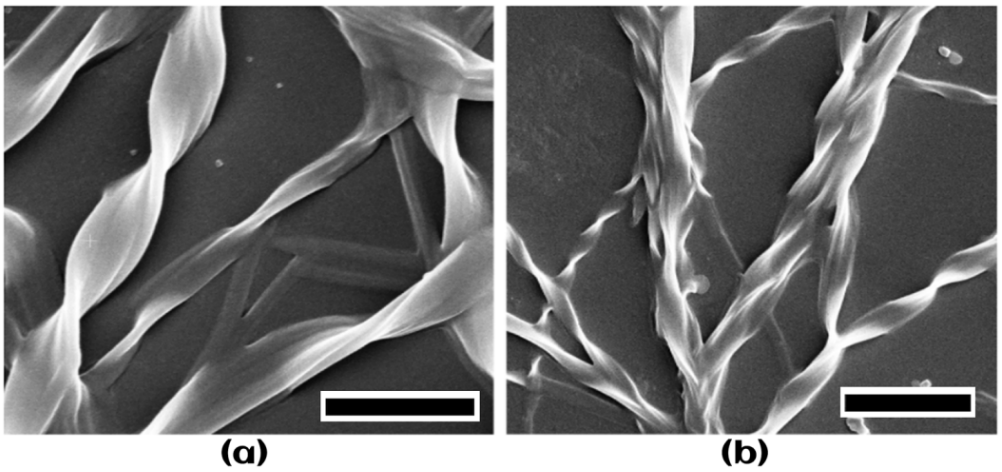

FIGURE 3.13: The field emission scanning electron microscope images show the twisted nanoribbons due to the incorporation of (a) 0.2 and (b) 0.5 wt % of SNP. The scale bar in (a) and (b) represents a length of 2 and 3 μm, respectively.

The core of the TP molecule is rich in π-electrons. Such molecules display a greater affinity towards each other through their π-π interaction. Due to such π-stacking, the discotic molecules self-assemble and yield a one-dimensional nanowire. These nanowires can interact with each other laterally through a cohesive force in a similar manner to that seen in the case of bundles of single-walled carbon nanotubes [84, 85]. The lateral assembly of the nanowires grows to give rise to a flat ribbon-like structure (Fig. 3.14(a)). Due to the incorporation of SNP in the matrix of TP molecules during the self-assembly, topological defects in the form of dislocations and disclinations are created (Fig. 3.14(c)). These defects can develop a geometrical frustration leading to some non-uniform interplanar elasticity which relaxes with the formation of helical twisted ribbons (Fig. 3.14(b)) [77, 86]. It can be noted that with the increase in the concentration of SNP, unlike a chiral dopant, the pitch of the helix increases. A chiral dopant can induce a helical structure due to a local chiral interaction and global constraints, which are imparted by the geometry of self-assembled structures [65]. Therefore, the pitch of helices should decrease with the increase in the concentration of the chiral dopants [65, 66, 87]. In the present case, with the increase in the concentration of SNP dopants, the concentration of defects increases. These defects may annihilate and thereby reduce the strength of geometrical frustration in the assembly [88, 89]. Hence, the overall chirality of the twisted nanoribbons seems to decrease with the increase in the concentration

of SNP. The outer surface of the nanoribbons and helical nanoribbons consists of aliphatic chains of TP molecules. Even the geometrical perturbation of aliphatic chains due to their interaction with some analytes can lead to a change in the dielectric constant, which can be measured at a high resolution using the optical phenomenon surface plasmon resonance (SPR). The surface plasmon wave is generated due to a quantized oscillation of free electrons at the metal-dielectric interface by the incidence of the electromagnetic wave. SPR can occur due to the matching of components of wavevectors corresponding to the incident electromagnetic wave and the surface plasmon wave.

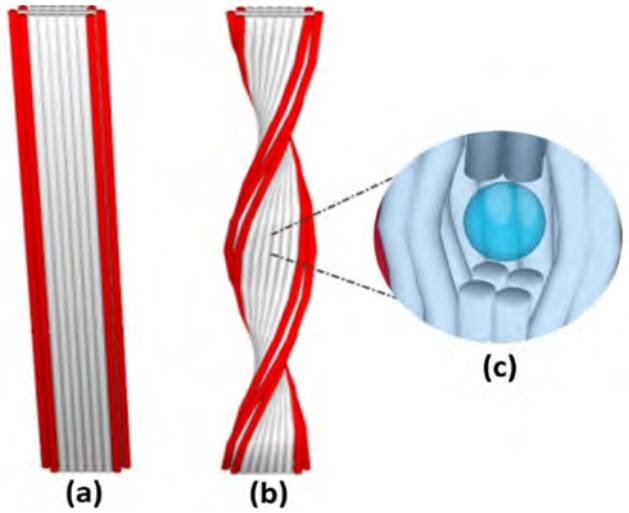

FIGURE 3.14: Schematic representation of (a) nanoribbon and (b) twisted helical nanoribbon and (c) an SNP inside twisted nanoribbon. Each tubule (nanowire) represents one column of π-stacked TP molecules. The nanowires interact laterally through a cohesive force to yield nanoribbons.

In the Kretschmann configuration, this can be detected by recording reflected intensity as a function of the angle of incidence. At SPR, the reflected intensity tends to be minimum due to the maximum absorption of incident beam energy by the resonance condition. The resonance condition is extremely sensitive to a minor change in the dielectric constant at the metal surface. This is the basic foundation for using the SPR phenomenon for any chemical and biological sensing applications. SPR-based sensors are label-free, sensitive, and of very high resolution. A minute change in dielectric/refractive index at the interface, which arises due to even morphological changes, can be detected very accurately using the SPR phenomenon. The reflected intensity as a function of the angle of incidence can be modeled theoretically

by applying Fresnel's theory for a number of layers involved in the experiment [46]. The refractive index of the layers can be estimated from such modeling. The optical anisotropy in ultrathin film fabricated by self-assembly and the Langmuir-Blodgett techniques arises due to the tilt of the molecules with respect to the surface normal and can be measured using the SPR phenomenon [90].

A minor perturbation in the geometrical structure of the nanoribbons can lead to a perceptible change in the dielectric constant when measured using an SPR instrument. This phenomenon was employed for sensing organic solvents, namely acetone, and ethanol, using the nanoribbons and nanoparticles incorporated in nanoribbons. The surface area of the helical nanoribbons due to the incorporation of SNP in the matrix of TP molecules is expected to increase enormously, which can lead to enhanced sensing performance as compared to that of flat nanoribbons.

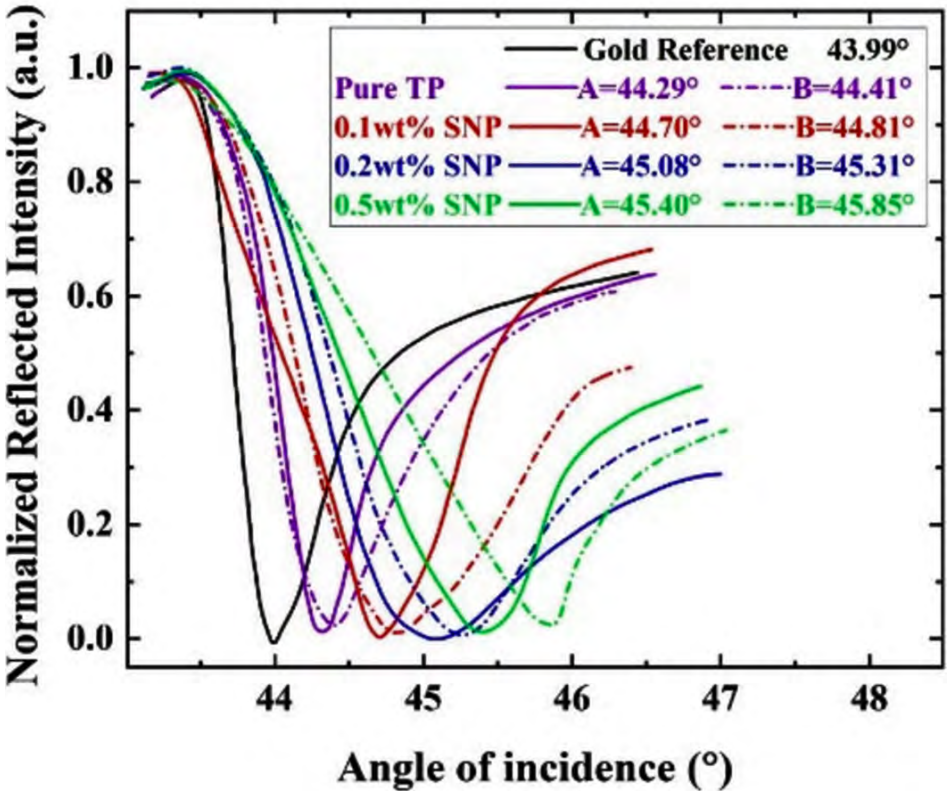

FIGURE 3.15: The SPR spectra obtained for nanoribbons and helical nanoribbons measured in the orthogonal directions, A and B.

The optical anisotropy of the nanoribbons was measured using the SPR phenomenon. The film of the nanoribbons was deposited on the surface of 50 nm gold film over the BK7 glass plate. The SPR spectra were recorded in two orthogonal directions, and they are shown in Fig. 3.15. The resonance angle (RA) for the orthogonal directions of a given composition of the film is found to be different. The difference in the RA values measured in the orthogonal direction for a given composition indicates some degree of optical anisotropy of the dielectric material deposited over the gold film.

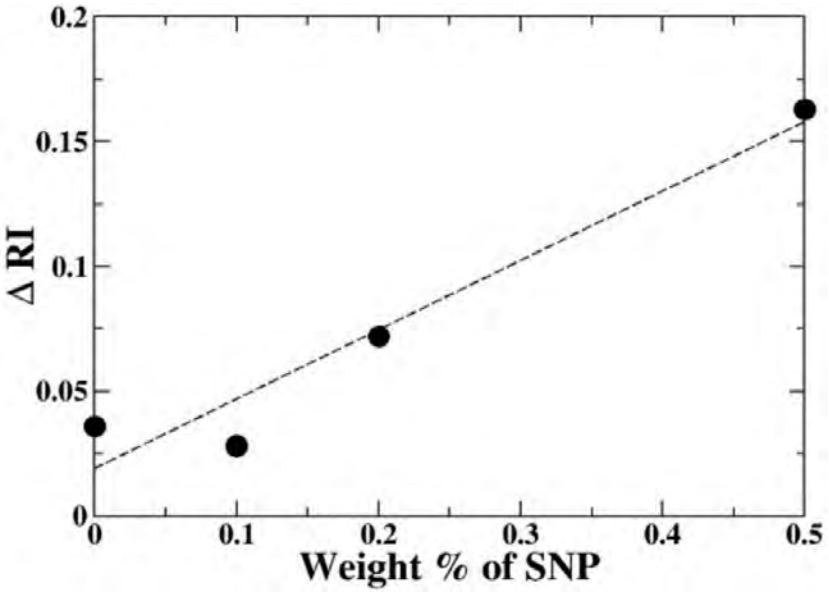

FIGURE 3.16: The RI estimated using Fresnel's relation and the change in RI (ΔRI) measured in orthogonal direction plotted as a function of the concentration of SNP in the nanoribbons.

The refractive index (RI) is estimated by modeling reflectivity from three interfaces, viz. glass-gold, gold-nanoribbon, and nanoribbon-air, as a function of the angle of incidence by utilizing the Fresnel's relation [46]. The change in RI when measured in the orthogonal direction (ΔRI) for different compositions is plotted as a function of the concentration of SNP in the TP matrix (Fig. 3.16). The anisotropy grows with the increase in the concentration of SNP in the matrix of TP molecules. Fig. 3.17 shows the kinetic curves for normalized response (NR) measured while sensing acetone and ethanol using SPR with a bare gold surface. The SPR signal, in terms of reflected intensity, is normalized with respect to the concentration of

the analyte dispensed through a flow cell over the sensing layer. The magnitude of normalized response is found to be larger for ethanol than that for acetone.

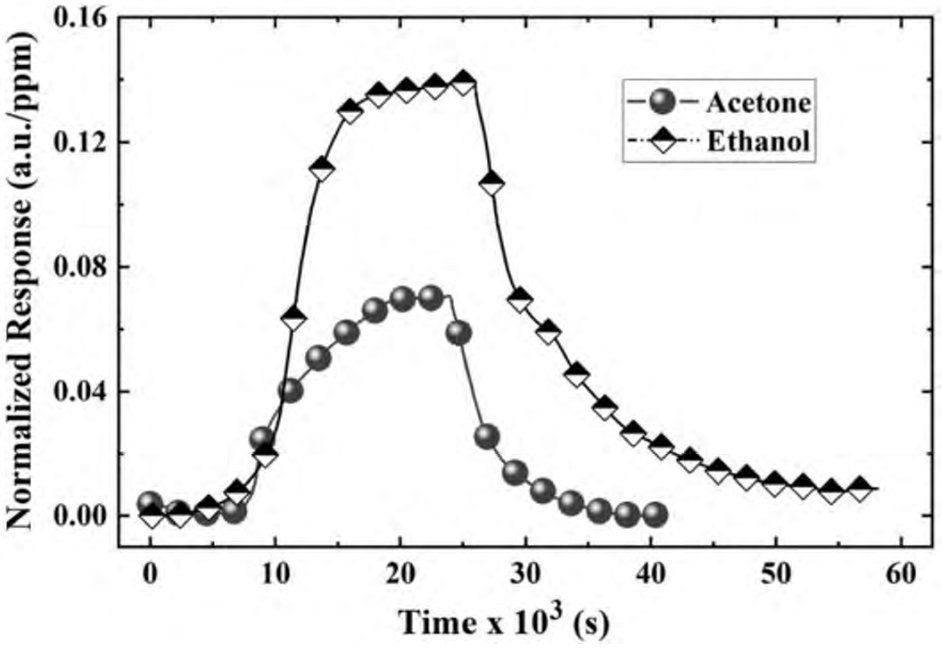

FIGURE 3.17: The normalized response curves as a function of time obtained from the SPR instrument on dispensing acetone and ethanol through a flow cell. The sensing layer is just the bare gold surface.

The gold surfaces were functionalized by depositing nanoribbons and helical nanoribbons incorporated with SNP and were employed for sensing acetone and ethanol. Fig. 3.18 shows the normalized response curves for sensing acetone and ethanol. The magnitude of NR for sensing ethanol is found to be large compared to that of acetone. In addition, the magnitude of NR when sensing acetone and ethanol is about three times larger compared with that of the functional layer of pure gold (Fig 3.17). Ethanol is more polar compared to that acetone and thereby interacts more effectively with the aliphatic side chains of the TP molecules in the nanoribbon's framework.

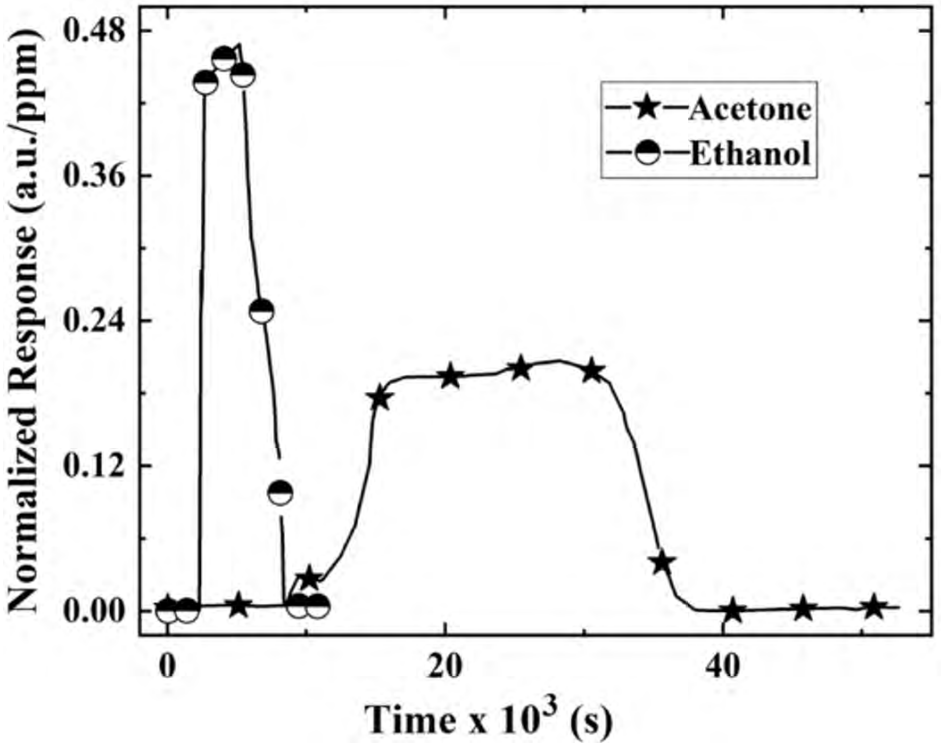

FIGURE 3.18: The normalized response curves obtained from the SPR instrument on dispensing acetone and ethanol through a flow cell. The sensing layer was a film of nanoribbons of pure TP molecules.

Therefore, the perturbation in the geometry of aliphatic chains of the TP molecules in the supramolecular assembly is significantly larger due to its interaction with ethanol as compared to the interaction with acetone. The role of relative humidity (RH) on the sensing performance was studied. We recorded the percentage change in the response due to the presence of water molecules. Fig. 3.19 shows the percentage change in the SPR response as a function of relative humidity from the bare gold surface, nanoribbons on a gold surface, and nanoribbons on the gold surface with acetone and ethanol. The RH has a negligible effect on sensing acetone and ethanol using the nanoribbons. The aliphatic chains of the TP molecules in nanoribbons create a good hydrophobic layer over the gold surface and thus do not interact with the water molecule. The effect of RH on the bare gold surfaces is also negligible until RH $\leq 75\%$. There is a minor increase in percentage response for higher RH values. Pure gold is hydrophobic in nature and thus does not interact with water molecules [91].

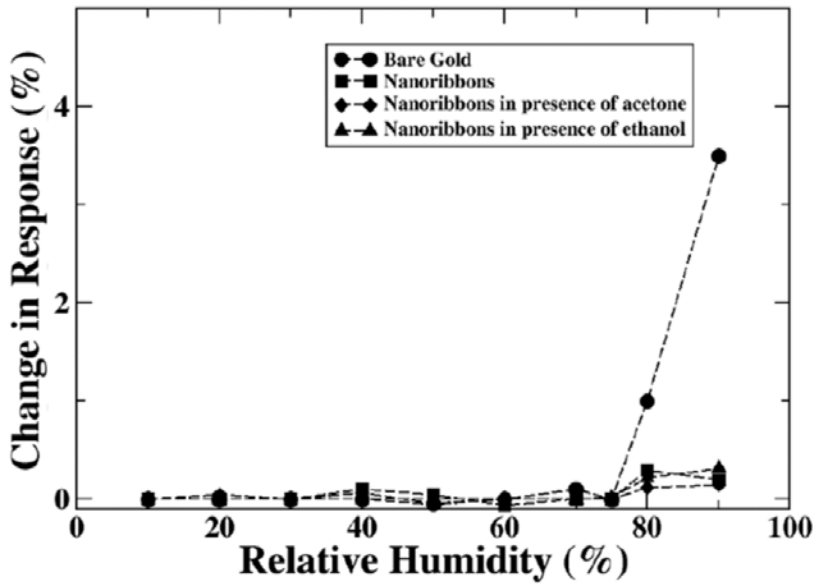

FIGURE 3.19: Effect of relative humidity on SPR response from different functional layers e.g. bare gold, nanoribbons on gold, nanoribbons in presence of acetone or ethanol at a fixed concentration of 0.1 ppm.

We found a significant improvement in the sensing performance when the SNP-incorporated nanoribbons were employed for sensing organic solvents.

Fig. 3.20 shows the acetone and ethanol sensing response from functional layers consisting of nanoribbons incorporated with a different weight percentage of SNP. The magnitude of the normalized response is found to increase with the increase in the concentration of SNP in the nanoribbon matrix. The enhancement in response is attributed to the gain in the surface-to-volume ratio of the twisted nanoribbons as compared to that of flat nanoribbons. For the concentration of 0.6 wt% of SNP, the response is found to be similar to that of 0.5 wt%. The maximum miscible concentration of SNP in the TP matrix is 0.5 wt% above which there is phase separation.

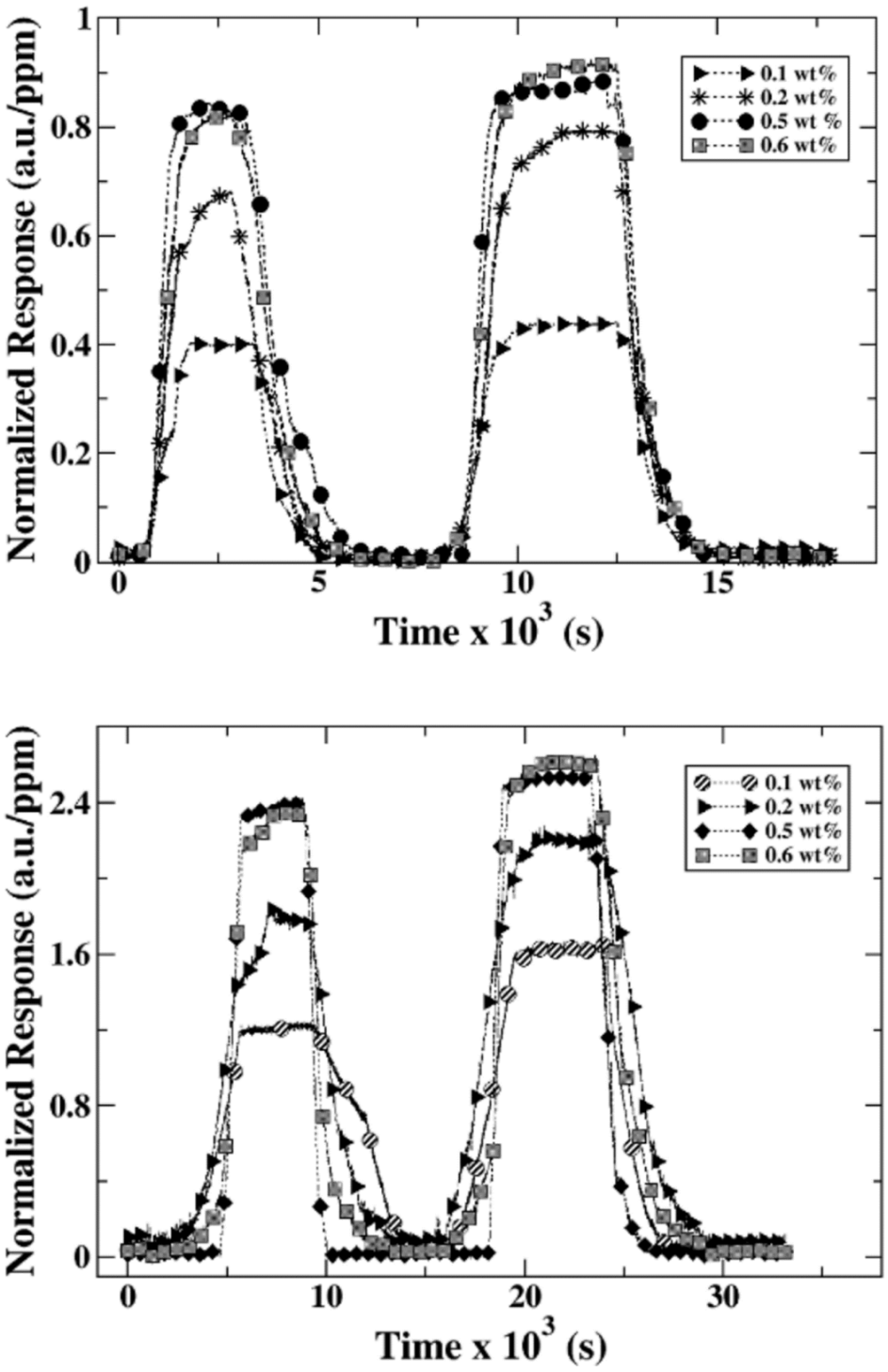

FIGURE 3.20: The normalized response curves obtained from the SPR instrument on dispensing (a) acetone and (b) ethanol through a flow cell. The sensing layer consists of nanoribbons of TP incorporated with different weight percentages of SNP.

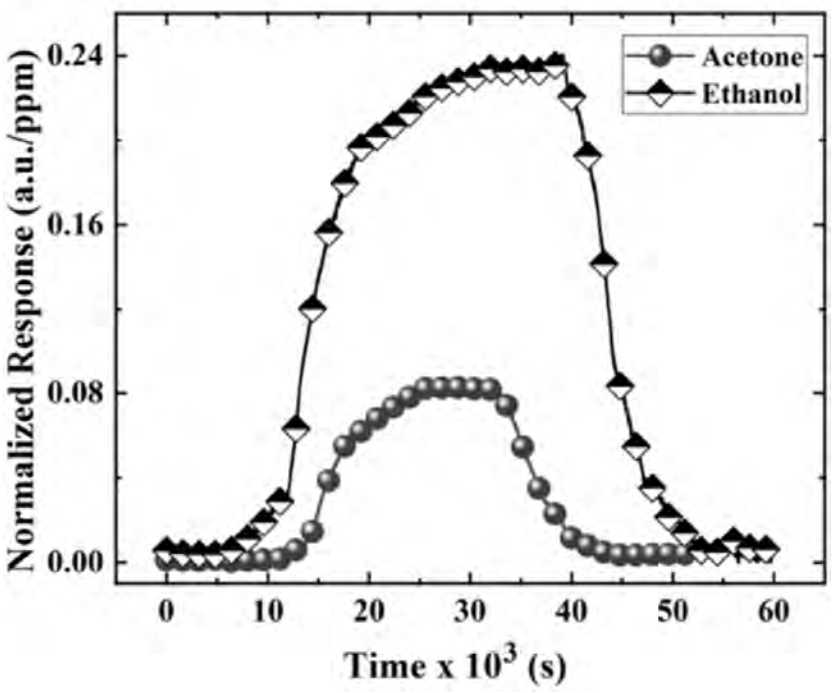

FIGURE 3.21: The normalized response curves were obtained from the SPR instrument on dispensing acetone and ethanol through a flow cell. The sensing layer consists of the spin-coated thin film of TP molecules.

In order to confirm the role of supramolecular assembly on sensing performance, a spin-coated film of TP molecules was deposited, and the sensing performance was evaluated. The normalized response curve is shown in Fig. 3.21. The magnitude of the normalized response curves from the spin-coated film is found to be much lower than that from supramolecular assemblies of nanoribbons and twisted nanoribbons. The TP molecules in the spin-coated film are expected to arrange randomly on the surface. Due to the interaction of TP with the molecules of the organic solvents, the perturbation in the molecular assembly brought in by them is marginal. Hence, the response is not very appreciable when measured using the SPR technique. The magnitude of the normalized responses (|NR|) obtained during sensing of acetone and ethanol by using different functional layers is shown in Fig. 3.22.

The sensing performance of the nanoribbons and twisted nanoribbons is found to be remarkably high as compared to that of bare gold and spin-coated film of TP molecules. The enhanced normalized response due to twisted nanoribbons is due to a gain in the surface-to-volume ratio as compared to flat nanoribbons. The |NR| values from twisted nanoribbons with 0.5

wt% of SNP are found to be enhanced by more than one order of magnitude as compared to pure gold or a spin-coated film of TP molecules.

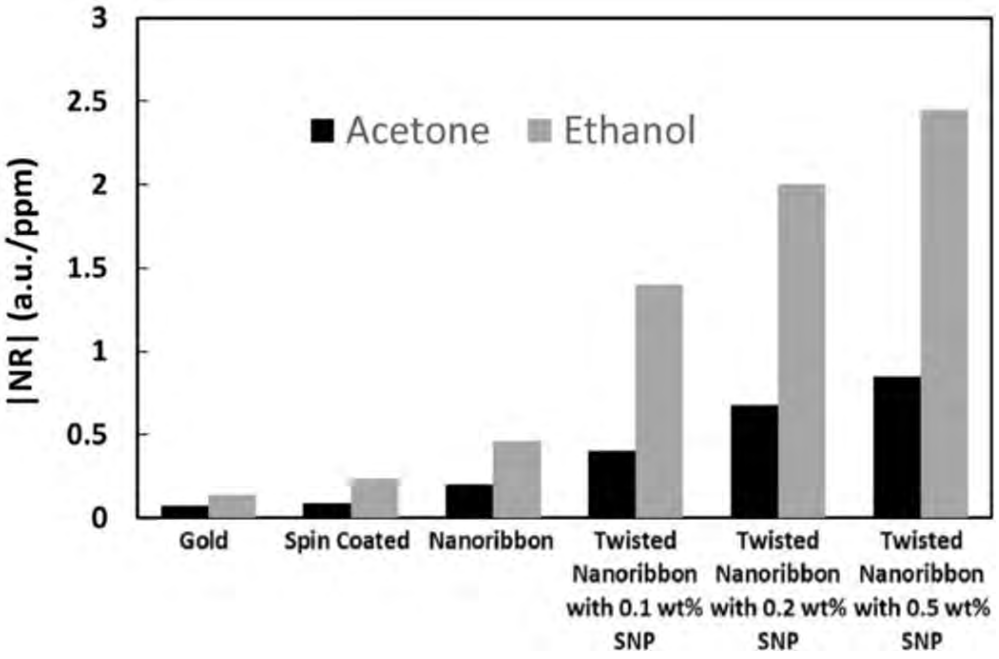

FIGURE 3.22: Bar diagram showing the magnitude of normalized response |NR| obtained during sensing of acetone and ethanol using different functional layers.

The perturbation of the aliphatic chain structure of the supramolecular assembly by the organic solvents acetone and ethanol can be measured at a high resolution by using the SPR phenomenon. Our studies lay the foundation for sensing applications utilizing the supramolecular assembly of discotic liquid crystal molecules.

3.4 Conclusion

The TP molecules are found to be very interesting. The assembly of the TP molecules in the solvent phase shows the nanofibers. These nanofibers behave like a classical semiconductor wherein the charge transfer is governed by the hopping mechanism. On doping with SNP, the activation energy drops by 43%. Critical structural analysis using the FESEM images reveals flat nanofibers similar to nanoribbons. The self-assembly of discotic liquid crystal

molecules yields a supramolecular nanoribbon structure which is governed by the $\pi - \pi$ stacking interaction between the discotic molecules. Here, the 1D nanowire assembly further assembles due to lateral van der Waals interaction forming the long ribbons structure. The nanowire assembly can be perturbed with the formation of defects like disclination and dislocation due to the incorporation of silver nanoparticles. This leads to the formation of twisted helical nanoribbons. The electrical characterization reveals the overall semiconducting properties of the nanoribbons and twisted nanoribbons. The charge transfer is dominated by the hopping mechanism in both assemblies. The EA decreases due to the incorporation of silver nanoparticles.

The morphology of the nanoribbons changes dramatically due to the incorporation of SNP in the TP matrix. The presence of SNP in the matrix introduces topological defects in the form of disclinations and dislocations. Such defects induce geometrically frustrated assembly leading to helical nanoribbons. The supramolecular assembly of nanoribbons and twisted nanoribbons consists of aliphatic chains of the TP molecules on their surface. The geometry of aliphatic chains can be perturbed by their interaction with the molecules of organic solvents. The helical nanoribbons obtained due to the incorporation of SNP tend to increase the surface-to-volume ratio leading to an enhanced sensing performance towards acetone and ethanol. The exposure of nanoribbons and SNP - incorporated nanoribbons to organic solvents like acetone and ethanol can create a minor distortion in their molecular assemblies, which can be detected using the SPR phenomenon at a very high resolution. It was further observed that the response was better for ethanol than that of acetone due to the fact that ethanol is more polar than acetone which can bring in a larger distortion to the molecular assemblies in the nanoribbons. The sensing performance was demonstrated at room temperature, and it was found to be independent of relative humidity. This work demonstrates that the morphological perturbation of the aliphatic chains of the organic molecules during their interaction with organic solvent molecules can give rise to a perceptible change in RA from the SPR instrument. It is, therefore, interesting to investigate the minuscule change in the refractive index of the ultrathin film of rod-shaped organic molecules either due to the tilt of the molecules or polarization-induced morphological changes. These were investigated, and the results are reported in the next chapters of this thesis.

Chapter 4

Surface plasmon resonance for the measurement of polarization of EM wave dependent sensitivity from an ultrasensitive layered structure

---

The previous chapter indicated that morphological transformations in the aliphatic chains of the nanostructures of the TP molecules can be employed for sensing acetone and ethanol gases due to the perceptible response from the SPR instrument. It is therefore interesting to investigate the next level of measurement by investigating the anisotropy in the refractive index in ultrathin film and polarization-dependent modulation of the SPR response due to the incidence of the EM wave. The developed SPR instrument was employed for the measurement of optical birefringence in ultrathin film and was reported by our group in Plasmonics, in 2021, (DOI:10.1007/s11468-021-01373-1). This chapter deals with the fabrication of a highly sensitive layered structure of organic molecules and presents the influence of polarization of the external electromagnetic (EM) wave on the surface plasmon resonance response from the layered structure. The layered structure was formed by depositing a self-assembled monolayer

(SAM) of mercaptoundecanoic acid (MUA) followed by a single layer of Langmuir-Schaefer (LS) film of traditional calamitic liquid crystal molecule, 4-octyl-4- biphenyl carbonitrile (8CB). The SAM of MUA was found to be non-responsive to the change in resonance angle (RA) of surface plasmon resonance (SPR) due to the change in polarization of the external EM wave. However, such a layer provides a soft-surface platform for the single layer of 8CB molecules which gets perturbed locally due to the incidence of the external EM wave. We obtained an oscillatory modulation of the change in RA due to the change in the polarization angle of the EM wave with respect to the plane of incidence. The magnitude of sensitivity was found to be $\sim$4 milli°/° angle of polarization of the external EM wave. This study strongly suggests that the sensitivity of an SPR-based sensor can be controlled by altering the linear state of polarization of the incident external EM wave. This work is reported by us in Europhysics Letters in 2021 (DOI: 10.1209/0295-5075/133/67005).

4.1 Introduction

The optical phenomenon of surface plasmon resonance (SPR) is extremely popular in the field of sensing technology owing to its capability to offer label-free and a very high-resolution sensing platform [92–94]. There are several recent advancements in SPR-based technology, viz., surface plasmon resonance imaging for addressing multi-analytes [95, 96] and electrochemical surface plasmon resonance for biosensing [97–99].

A minute change in the dielectric constants of the medium on the metal surface due to adsorption of molecules can perturb the resonance condition, which can be detected at a high resolution by recording the change in resonance angle (RA). It has been demonstrated that not only the change in dielectrics due to the adsorption of analytes on the metal surface but also optical anisotropy (in-plane birefringence) due to the tilt of shape anisotropic organic molecules in a monolayer can be measured using the SPR phenomenon [100]. Similarly, in another report, we found that the structural perturbation in the aliphatic chains of a supramolecular assembly of discotic liquid crystal molecules due to its interaction with organic solvents can be measured using the SPR phenomenon. The measurement of such perturbation

can provide a new paradigm for sensing organic solvents using the supramolecular assembly of organic molecules [101]. The organization of organic molecules can be perturbed by several external fields, e.g., temperature, pressure, and electric field of an EM wave. In this chapter, we report the SPR measurement from a strategically developed layered structure of ultrathin films of organic molecules on perturbation due to the incidence of an external EM wave. The perturbation is found to be polarization dependent which yields a systematic change in the SPR response due to a change in the angle of polarization of the external plane polarized EM wave. The developed layered structure can serve as a functional layer for sensing applications wherein the sensing performance can be optimized by simply adjusting the angle of polarization of the external incident EM wave.

4.2 Experimental Procedure

A sensitive layered structure of ultrathin films of organic molecules was fabricated on a gold-deposited glass plate (SPR chip) by successive deposition of a self-assembled monolayer (SAM) of mercapto-undecanoic acid (MUA) followed by a single layer of Langmuir-Schaefer (LS) film of 4-cyano-4-pentylbiphenyl (8CB) molecules. Both the molecules were procured from Sigma-Aldrich at their highest purity and were used without any further purification. The -SH group of MUA can bind chemically with the gold surface to yield a well-organized single layer of SAM. In addition to this, the terminal -COOH group of MUA can offer hydrophilic functionality to the fabricated SAM. The 8CB molecules exhibit liquid crystalline phases, e.g., nematic and smectic, as a function of temperature in the bulk state. It is well known that the Langmuir monolayer of 8CB molecules is stable at the air-water (A/W) interface [102]. The monolayer at the A/W interface was observed with Brewster Angle Microscope (BAM). The monolayer at the A/W interface exhibited gas and liquid-like phases. The LS film of 8CB molecules was deposited in the liquid-like phase on the MUA-deposited gold substrate. The 8CB molecules are tilted with respect to the surface normal in the LS film [103]. The inclined monolayer can be viewed in the schematic as shown in Fig. 4.1. Such tilted molecules in the LB film can offer in-plane optical anisotropy [100].

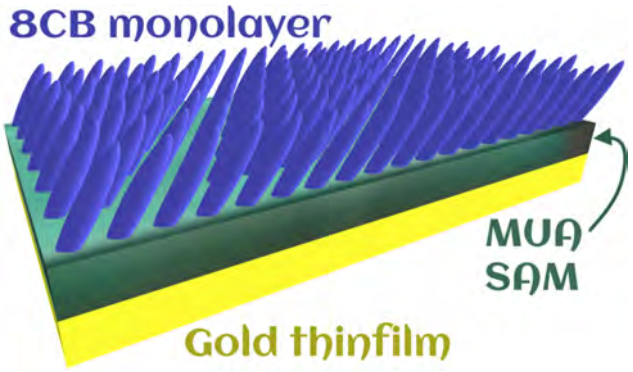

FIGURE 4.1: Schematic of a layered structure with tilted 8CB molecules.

The SPR chip was fabricated by the deposition of 50 nm thick gold film on a BK7 glass plate (refractive index = 1.51) by a sputtering technique. The SAM of MUA was deposited on the SPR chip by immersing it in a 1 mM solution of MUA in absolute ethanol solvent (from Merck). The substrate was taken out from the solution after 10 hours and was rinsed successively with absolute ethanol and deionized water. This yields a single layer of SAM of MUA with a hydrophilic surface due to the presence of the -COOH group at the terminal end of the MUA molecule. The gold chip with SAM of MUA was utilized for the fabrication of LS film of 8CB molecules. The presence of a single layer of SAM of MUA provides a soft surface for the 8CB molecules to feel the polarized states of the electric field of the external EM wave.

4.3 Results and discussion

The surface pressure (Π)-area per molecule (A_m) isotherm of Langmuir monolayer of 8CB molecules at the A/W interface was obtained using a Langmuir Blodgett (LB) trough (KSV-NIMA) and is shown in Fig. 4.2. The monolayer exhibits the traditional gas, liquid-like phase, and the collapsed state Fig. 4.2 [104]. The maximum value of in-plane isothermal elastic modulus (E) [105] is found to be 18 mN/m which is comparable with the elastic modulus of the liquid-like phase [106].

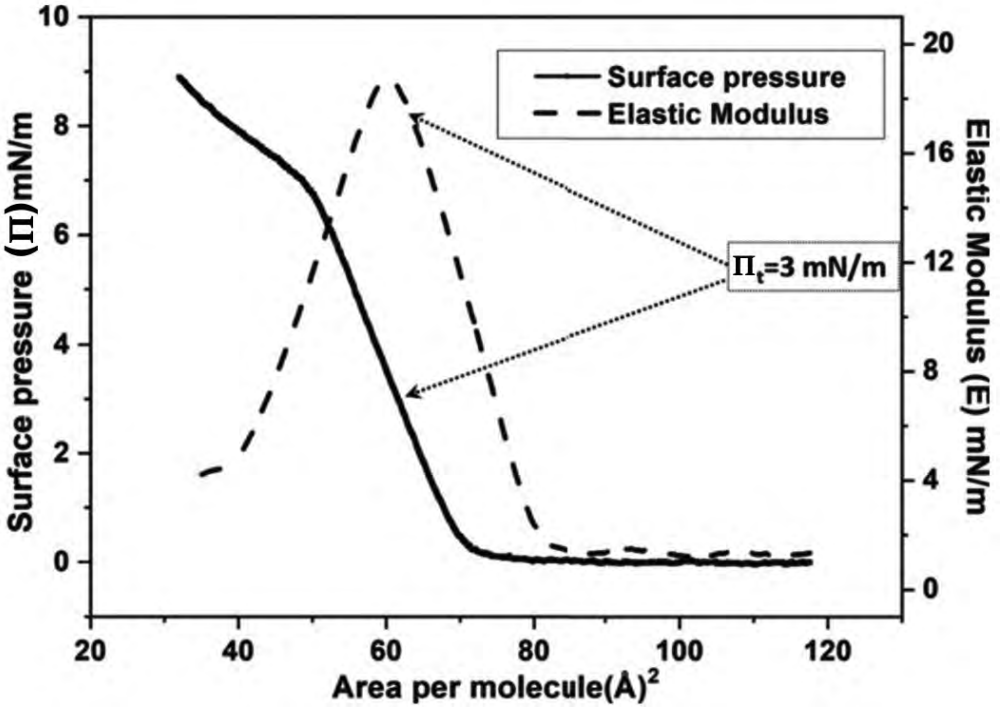

FIGURE 4.2: Surface pressure (Π)-area per molecule (A_m) isotherm of Langmuir monolayer of 8CB at the air-water interface. The corresponding isothermal in-plane elastic modulus (E) as a function of A_m is shown. The target surface pressure (Π_t = 3 mN/m) for the deposition of LS film is indicated in the isotherm and elastic modulus curves by arrows.

The BAM images of the Langmuir monolayer of the 8CB molecules at the A/W interface were captured in the different states of the monolayer (Fig. 4.3). The coexistence of gas (dark) and liquid-like (gray) phases can be seen from the image. On compression, the gray region grows and covers the complete field of view of the camera.

A single layer of 8CB was transferred from the A/W interface onto the MUA-modified gold chip by LS film deposition technique at a target surface pressure (Π_t) of 3 mN /m. Here, Π_t = 3 mN/m was chosen such that the film was transferred at the highest surface pressure just before the monolayer instability. In the LS method, a customized substrate holder was 3D printed such that it makes an angle of 15° with respect to horizontal. This mechanism facilitates the drainage of entrapped water between the substrate and organic layer during the horizontal transfer mechanism of the LS method. After the deposition of 8CB molecules, the layered structure consisting of gold/SAM of MUA/LS film of 8CB was employed for SPR measurements.

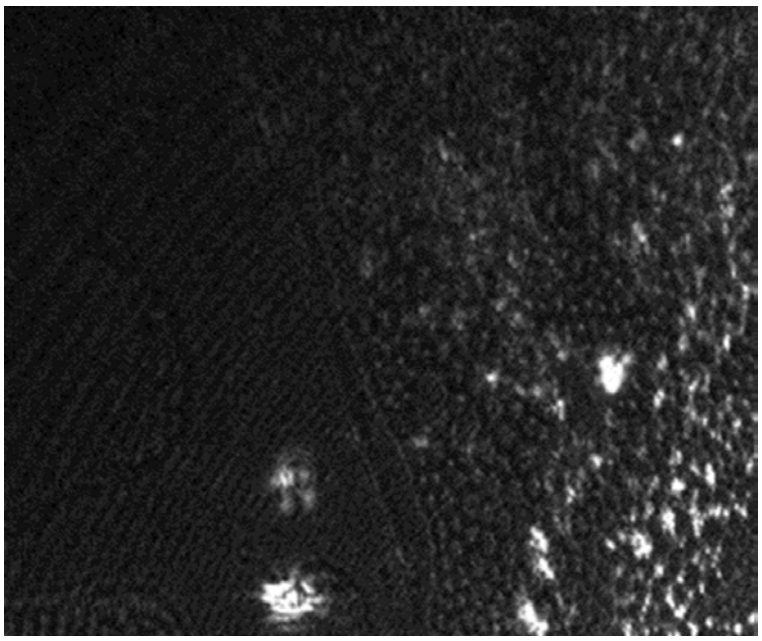

FIGURE 4.3: BAM image shows the coexistence of gas (dark) and liquid-like (gray domains) phases. The image size is 1.8×1.2 mm^2.

The morphology of the LS film of 8CB on the MUA-modified gold chip was obtained using Atomic Force Microscopy (AFM, NOVA) and Field Emission Scanning Electron Microscope (FESEM, FEI-APREO). The AFM images obtained for the unfunctionalized gold SPR chip (Fig. 4.4(a)), SAM of MUAon SPR chip (Fig. 4.4(b)) and LS film of 8CB deposited on the SAM of MUA functionalized SPR chip (Fig. 4.4(c)). The AFM images were taken at the same scale length. The average roughness observed is 1.42, 0.36, and 1.11 nm respectively.

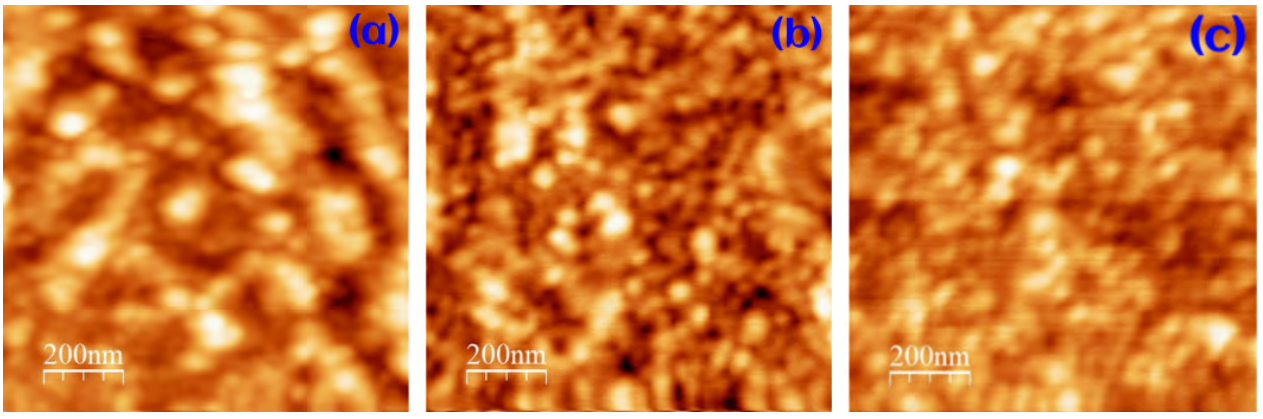

FIGURE 4.4: AFM images (a) unfunctionalized gold SPR chip (b) SAM of MUA on the SPR chip and (C) 8CB monolayer deposited on the SAM of MUA functionalized SPR chip.

Fig. 4.5(a) and (b) are the micrographs of the unfunctionalized gold SPR chip and SAM of MUA on the SPR chip. The liquid-like domains of the 8CB molecules in the LB film can be seen in the image (Fig. 4.5(C)).

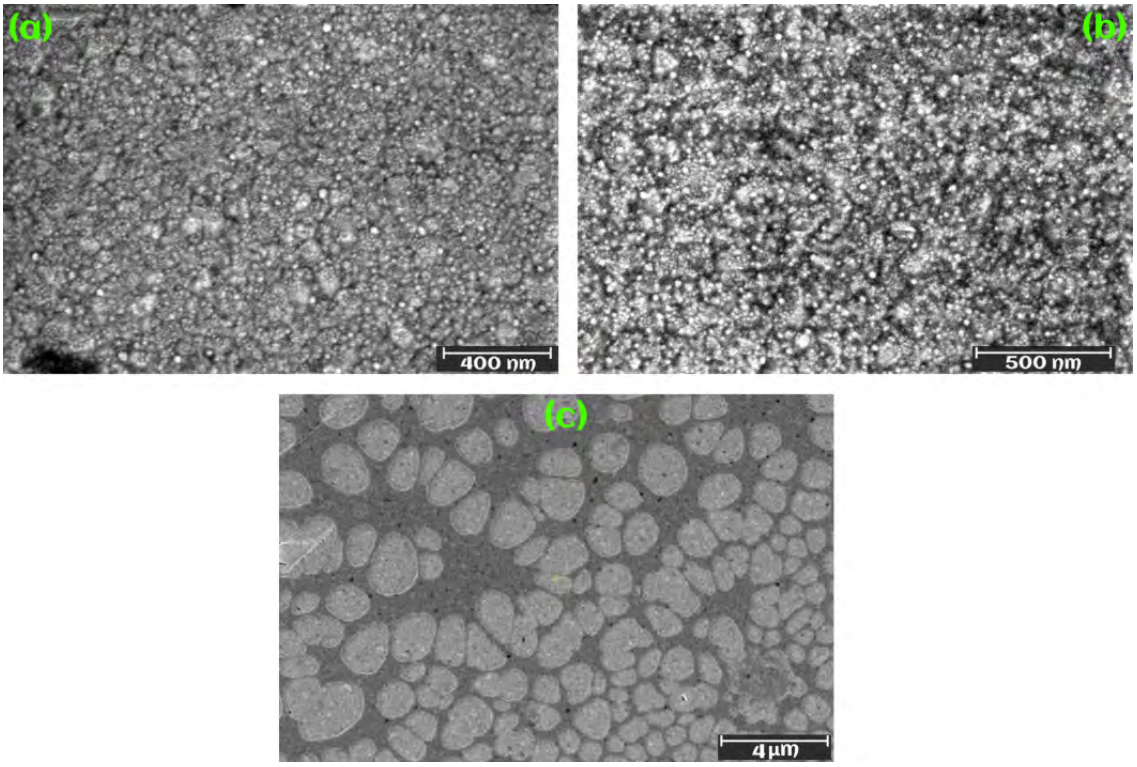

FIGURE 4.5: Field emission scanning electron microscope (FESEM) image of (a) bare SPR chip, (b) MUA SAM employed SPR chip (c) LS film of 8CB molecules deposited onto MUA modified SPR chip.

The SPR curves (Fig. 4.6) for gold/air, SAM of MUA over gold, and LS film of 8CB over the SAM of MUA are recorded using the SPR instrument in the Kretschmann configuration [46] for normal orientation of the film. The SPR curves for the SAM of MUA and LS film of 8CB were also recorded by rotating the films in the orthogonal direction. The optical anisotropy in terms of the refractive index of the ultrathin film due to the projection of rod-shaped molecules in the two-dimensional plane can be quantified in terms of shifts in resonance angles (RA) measured from the SPR curves of the film in the orthogonal direction [100]. The shift in RA of SAM of MUA and LS film of 8CB measured in the orthogonal direction is 0.07 and 0.36°, respectively. The non-zero values of $\Delta\theta$ indicate the optical anisotropy of the film due to the tilt of the molecules. The average tilt of the molecules in the ultrathin film can be

estimated from the average thickness of the film. Hence, the thickness of each layer, viz., gold, SAM of MUA, and LS film of 8CB was estimated from the X-Ray Reflectivity (XRR) measurement.

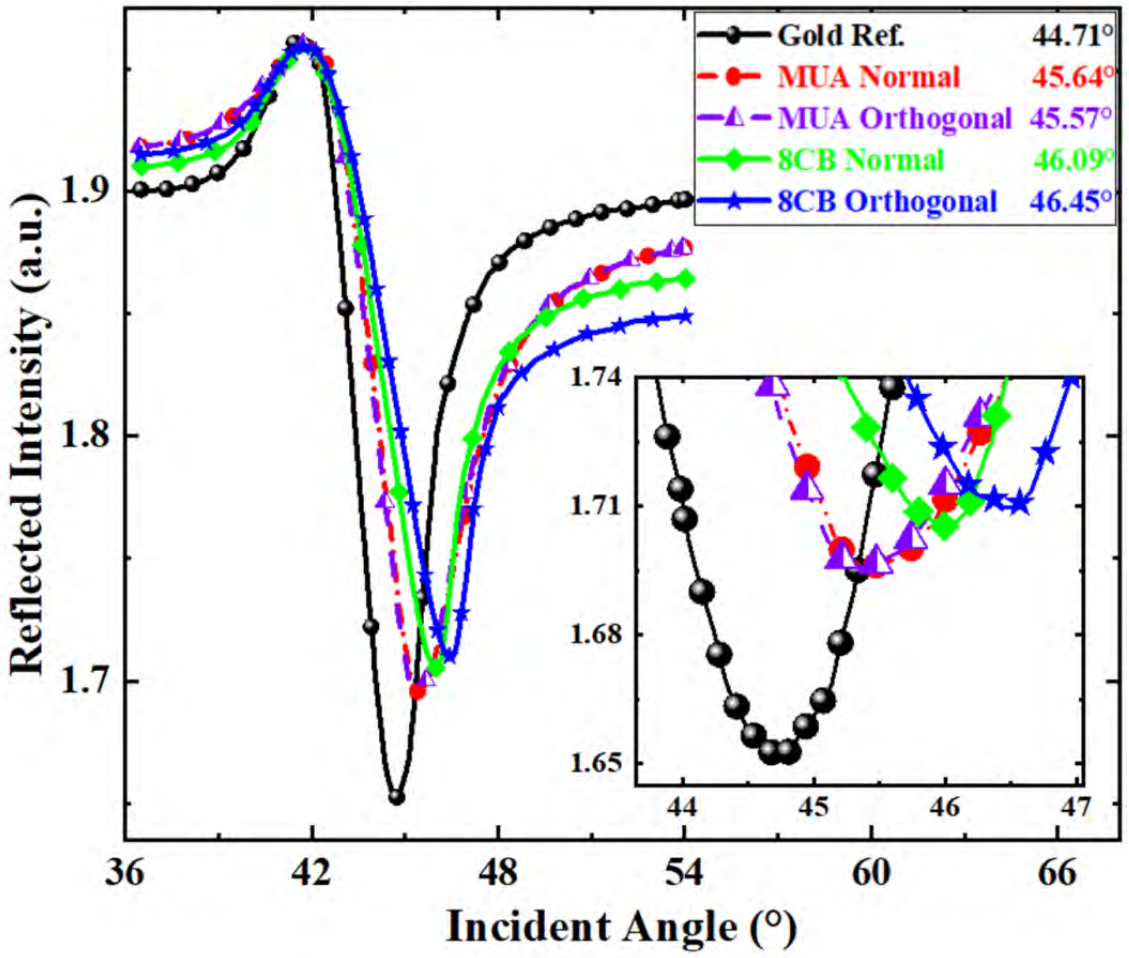

FIGURE 4.6: The surface plasmon resonance curves for gold/air, gold/SAM of MUA, and gold/SAM of MUA/LS film of 8CB. The SPR curves for each interface are recorded in orthogonal directions of the film. The values of the resonance angle (RA) are mentioned in the box.

Fig. 4.7 shows the XRR data (Rigaku, SmartLab) obtained for the gold film deposited over the BK7 glass plate, SAM of MUA over the gold film, and LS film of 8CB over SAM of MUA. The thickness of each layer was estimated by fitting the experimental curve with Parrat's formalism [106]. The thickness of the gold film, SAM of MUA, and LS film of 8CB in the layered structure was found to be 49.5, 1.7, and 1.0 nm, respectively. The theoretical value of the length of MUA and 8CB molecules was estimated from ChemSketch and it was found

to be 1.6 and 2.0 nm, respectively. The theoretical and experimental values of thickness for SAM of MUA are comparable, however, the experimentally obtained value of the thickness of LS film of 8CB is half as compared to the theoretically calculated value. The lower value of thickness as obtained in the XRR measurement can be accounted for by the tilt of the 8CB molecules in the LS film. Thus, the estimated tilt of the 8CB molecules with respect to the substrate normal is 60° which is inconsistent with an earlier reported value [103]. The tilted molecules in the ultrathin film have a non-zero projection on the 2D plane of the substrates which gives rise to the optical anisotropy as observed during the SPR measurements of the film in the orthogonal directions (Fig. 4.6).

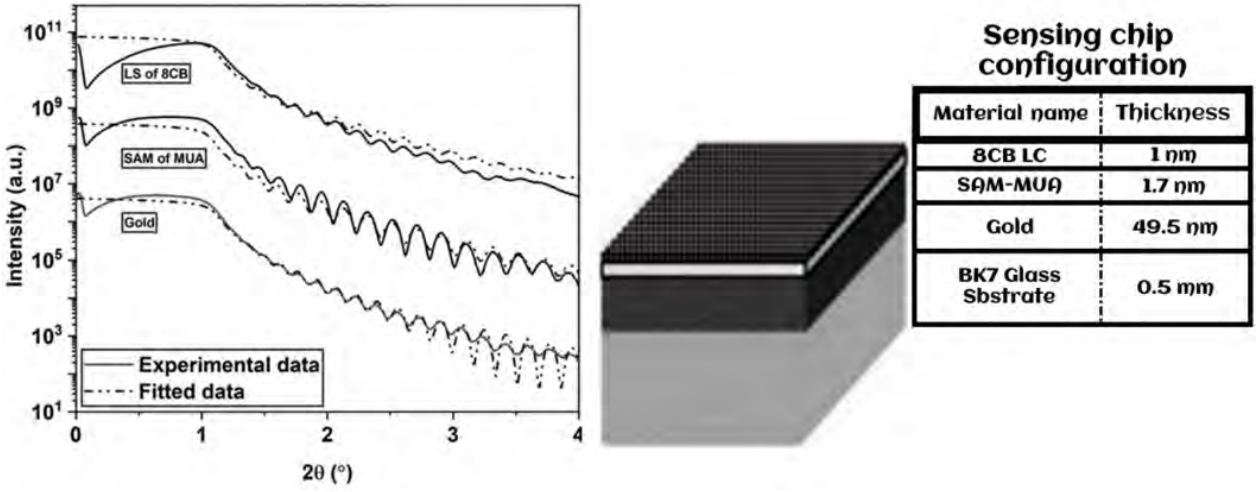

FIGURE 4.7: The X-ray reflectivity (XRR) curves obtained from a gold layer deposited over a glass substrate, SAM of MUA over the gold, and a single layer of LS film of 8CB deposited over the SAM of MUA. The experimental curve (solid line) is fitted with Parrat's formalism (dashed line) and the thickness of the layer is estimated. The schematic of the layered structure is shown.

Few reports in the literature indicate that the structural perturbation like gauche to trans (and vice versa) type in thin organic film at an interface can be induced by laser [107, 108]. Here, a modified Kretschmann configuration for the measurement of SPR response from the organized layered structure as a function of the angle of polarization of an externally polarized EM wave is developed in the laboratory. The schematic of the modification can be seen in Fig. 4.7. The SPR instrument using the Kretschmann configuration was developed as discussed in [46]. The setup was modified by integrating a second plane polarized diode laser. The head

of the diode laser was mounted on a circular graduated scale of resolution 1°. The EM wave of the known state of linear polarization was incident normally on the layered structure at the point of interrogation and the SPR response as a function of the angle of polarization (θ_p) of the second incident EM wave was recorded traditionally using the primary laser. The θ_p was measured with respect to the plane of incidence consisting of the primary laser and the detector of the SPR instrument. The resonance angle (RA) for the SAM of MUA was found Few reports in the literature indicate that the structural perturbation like gauche to trans (and vice versa) type in thin organic film at an interface can be induced by laser [107, 108]. Here, a modified Kretschmann configuration for the measurement of SPR response from the organized layered structure as a function of the angle of polarization of an externally polarized EM wave is developed in the laboratory. The schematic of the modification can be seen in Fig. 4.8. The SPR instrument using the Kretschmann configuration was developed as discussed in [46]. The setup was modified by integrating a second-plane polarized diode laser.

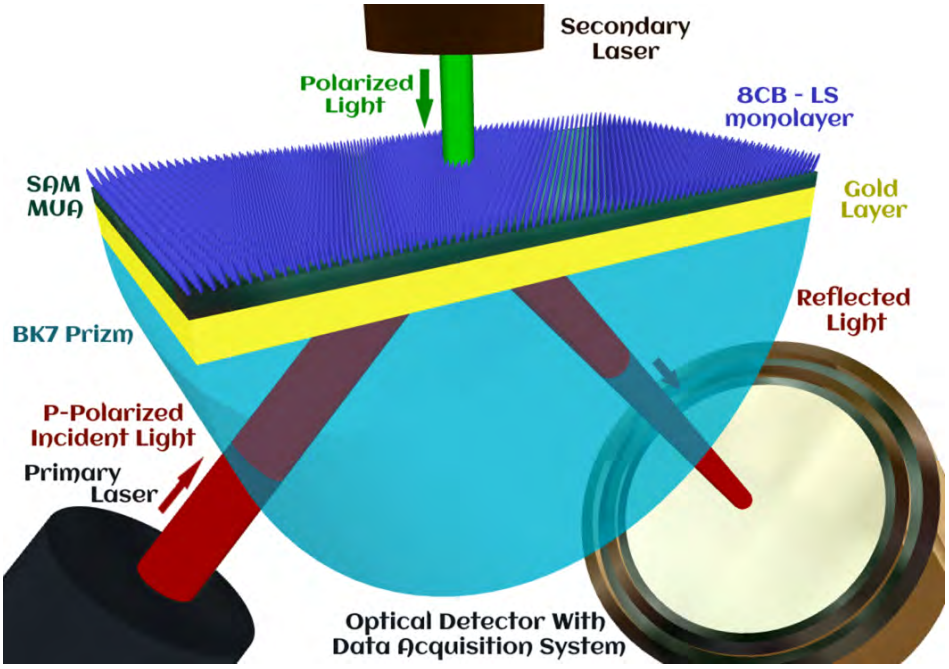

FIGURE 4.8: Kretschmann configuration setup for the measurement of surface plasmon resonance (SPR) response from the layered structure. The primary laser is used for the excitation of the surface plasmon polaritons, whereas a plane-polarized second laser is used for inducing structural perturbation in the 8CB layer. The angle of polarization of the second laser was varied with respect to the plane of polarization of the primary laser (θ_p), and the SPR response was measured.

The head of the diode laser was mounted on a circular graduated scale of resolution 1°. The EM wave of the known state of linear polarization was incident normally on the layered structure at the point of interrogation and the SPR response as a function of the angle of polarization (θ_p) of the second incident EM wave was recorded traditionally using the primary laser. The θ_p was measured with respect to the plane of incidence consisting of the primary laser and the detector of the SPR instrument. The resonance angle (RA) for the SAM of MUA was found at an interval of change in θ_p by 90°. This suggests that any structural perturbation in the LS film of 8CB induced by the external EM wave is reversible in nature. The layered structure (gold/MUA/8CB) is thus highly sensitive toward any perturbation even due to the incidence of external EM fields. This study provides a platform for tuning the sensitivity of SPR-based sensors by altering the polarization of the external EM wave. In the present case, the sensitivity calculated from Fig. 4.9 lies in the range of 3.5–4.5 milli°/° of the angle of polarization of the external EM wave.

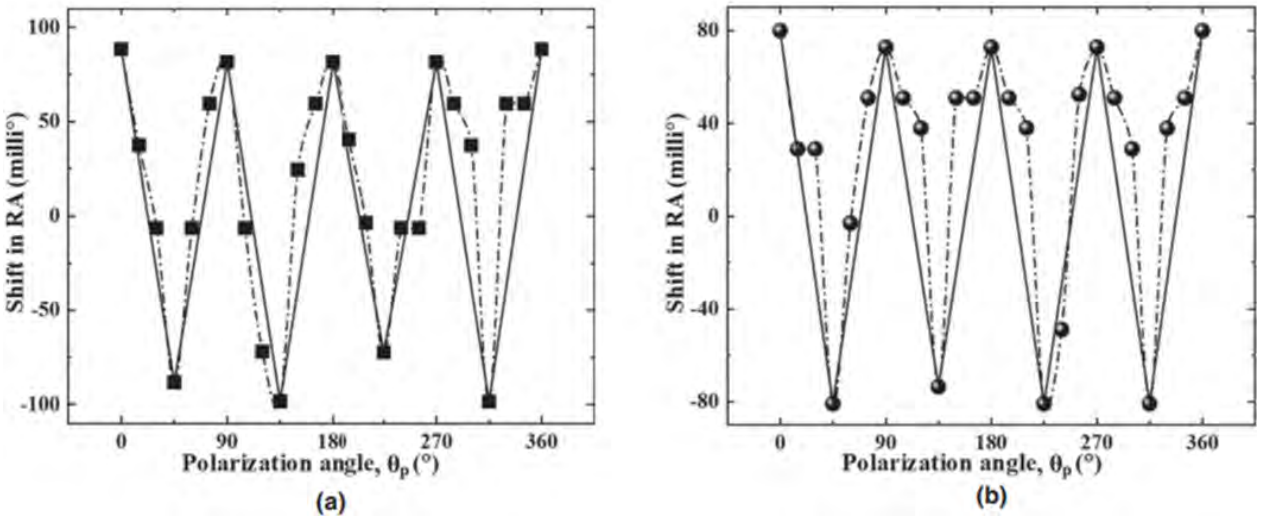

FIGURE 4.9: The variation in the shift in the resonance angle (RA) as a function of the angle of polarization (θ_p) of the external electromagnetic wave of wavelength (a) 653 nm and (b) 532 nm obtained from layered structure (gold/MUA/8CB) using a modified SPR instrument. θ_p is measured with respect to the plane of polarization of the primary laser in the SPR setup. The experimental data are shown as symbols and broken lines, whereas the solid lines are fit to show the oscillatory nature.

This study presents a systematic control of resonance angle in SPR measurement from a sensitive layer by the polarization of an external EM wave. A layered structure (gold/SAM of

MUA/LS film of 8CB) was fabricated strategically such that the monolayer of liquid crystal molecules (i.e., LS film of 8CB molecule) can be perturbed by the polarization of external EM waves. The underlying SAM of MUA offers a soft surface for the 8CB molecules to respond largely due to the incident EM wave. The oscillatory nature of the shift in RA as a function of the angle of polarization of the external EM wave was obtained. In the development of a biosensor, the surface of the transducer is functionalized by immobilizing suitable ligands in a layered structure. The sensitivity of such an SPR-based biosensor can be controlled by an external EM wave.

4.4 Conclusion

This study presents a tunable sensitivity of an SPR-based sensor by altering the polarization of a plane-polarized external EM wave. In the next chapter, an ultrathin film of optically active liquid crystal molecules was employed for observing the optical switching phenomenon using the developed SPR instrument.

Chapter 5

Surface plasmon resonance for optical switching application using ultrathin film of photoactive liquid crystal molecules

---

In the previous chapters, we demonstrated a very high capability of the SPR instrument by recording any perturbation in the local molecular structure to great accuracy. In this chapter, we employed an optically active ultrathin film of liquid crystal molecules and observed the optical switching properties using the SPR phenomenon. The development of an optically active area consisting of organic molecules is essential for the devices like optical switches and waveguides, as they can be easily maneuvered by the application of suitable electromagnetic (EM) waves.

In this chapter, we report another non-traditional application of the SPR phenomenon wherein the SPR response is monitored due to a change in morphology of the H-shaped liquid crystal molecules in ultrathin LB film. A photoactive surface was created by the deposition of a single layer of Langmuir-Blodgett (LB) film of a novel H-shaped liquid crystal (HLC) molecule. The synthesized HLC molecules possess azo-groups and nitro-groups. The azo-group can be isomerized (trans-cis transformation) by irradiating them with ultraviolet

(UV) light. The nitro-group can provide sufficient amphiphilicity to the HLC molecules to form a stable Langmuir monolayer at the air-water interface. Fig. 5.1 shows the morphological changes on ultrathin film of H-type liquid crystal molecules under the influence of ultraviolet electromagnetic wave.

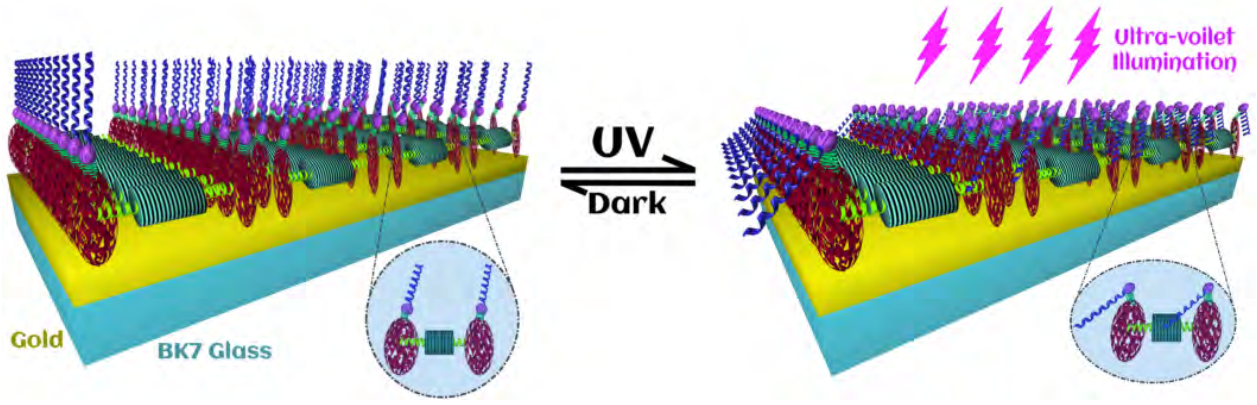

FIGURE 5.1: Morphological changes on the ultrathin film of H-type liquid crystal molecules under the influence of ultraviolet electromagnetic wave.

The Langmuir monolayer of the HLC molecules exhibited gas and liquid-like phases. A single layer of LB film of HLC molecules was deposited on a gold chip of a home-built surface plasmon resonance (SPR) instrument. The azo-groups of the molecules in LB film were excited by UV irradiation leading to a change in morphology due to trans-cis transformation. Such a change in morphology can lead to a minuscule change in the refractive index (RI) of the LB film. The developed SPR instrument was utilized for the measurement of such minute changes in RI. In our studies, we found systematic changes in the resonance angle of the LB film of HLC molecules as a function of the intensity of the UV irradiation. We measured switch-on and switch-off intensity, which may suggest that the LB film of HLC molecules can find applications in optical switches or waveguides. This work is published by us in Journal of Molecular Liquids of Elsevier in 2022 (DOI: 10.1016/j.molliq.2022.120071).

5.1 Introduction

The control of physicochemical properties of materials due to external parameters, viz. electric, magnetic fields, or electromagnetic (EM) waves, is essential for the design and development of novel devices. One of the popular mechanisms is to obtain control by designing photoactive organic molecules. Mostly, the chromophore is chemically attached to the molecules which can be excited by the absorption of the suitable EM wave. The molecule can de-excite to a lower energy level by a radiative process with the emission of an EM wave of lower energy or a non-radiative process by changing the morphology of the molecules. Azo-group (-N=N-) is one of the groups which can be a morphological transformation from trans-to-cis by exciting them using EM wave of wavelength in the ultraviolet range [109–116]. The molecule can relax back to trans conformation either by exposure to ambient light or even in a dark state [117]. The morphological transformation of organic molecules promises several unique device applications viz. optical switches, molecular motors, waveguides in photonics, etc [114, 118–122]. The mesophases of liquid crystal (LC) molecules can be influenced by external parameters like temperature, pressure, and electric and magnetic fields. The structure-property relationship of the liquid crystal molecules is important to obtaining LC-based high-performing devices. The chemical structures of the molecules can be changed to introduce new phases and enhance liquid crystalline properties in a given mesophase. The liquid crystal molecules possessing the azo-group are very interesting as the morphology of the molecules can be changed under the influence of EM waves leading to changes in the bulk liquid crystalline phases. Two-dimensionally confined monolayers are good candidates for the development of next-generation flexible and transparent optoelectronics devices [123–126]. Due to the enhanced physicochemical properties of the ultrathin films, their activity is extremely high as compared to the thick layers or bulk materials. It is, therefore, interesting to study the surface behavior of organic molecules exhibiting functional groups which can be tapped through external parameters to deliver high-performing devices. The deposition of ultrathin film at air-solid interfaces using the Langmuir-Blodgett (LB) methodology is very interesting as they possess a huge potential for industrial application. It can be applied as both active and passive layers for a number of device fabrications. In the field of sensors, it has been reported

that the organized and ultrathin nature of LB films of materials can offer a large enhancement in sensing parameters as compared to randomly oriented thick films [127, 128]. The LB films can be used for non-linear optical devices, photovoltaics, ultrafiltration membrane, molecular electronics, and energy storage devices [129–131]. The shape-anisotropic liquid crystal molecules at the air-water interface show very interesting results. A single layer of LC molecules at an interface offers a highly in-plane anisotropy in optical properties [132]. The low in-plane elastic modulus of the film of LC molecules facilitates easy geometrical perturbation by the application of external electric, magnetic fields, and EM waves [133]. Such geometrical perturbation can influence the optical and electrical properties and thereby provides an avenue for controlling the physical properties of the film by such external parameters.

There are several forms of shape anisotropic LC molecules which can form a stable Langmuir monolayer at the air-water interface and show a variety of interesting phenomena. There are several studies on Langmuir monolayer and LB films of rod-shaped [134], disc-shaped [135], and bow-shaped [133, 136] liquid crystal molecules. There are some studies on non-traditional LC molecules [137–139]. In this chapter, we report our studies on H-shaped LC molecules consisting of azo-groups and several chiral centers. The presence of two nitro-groups provides sufficient amphiphilicity to the molecules to form a stable Langmuir monolayer at the air-water interface. The monolayer in the liquid-like phase of the water subphase is transferred to a solid substrate by the highly controlled Langmuir-Blodgett (LB) technique [140]. The morphology of the LB film was obtained using a field emission scanning electron microscope (FESEM). The azo groups of the HLC were excited by irradiating the LB film using a UV source. This facilitates the trans-to-cis transformation. Such morphological transformation can lead to a change in the refractive index (RI) of the LB film, which was studied using a very high-resolution surface plasmon resonance instrument. Here, we report systematic changes in the RI by changing the intensity of the UV irradiation. We found a cut-off and saturation intensity which might be an indicator for the development of optical switches or RI-modulated photonic waveguides. In our earlier study (chapter - 4), we reported that polarization of an incident EM wave induced a change in morphology in a layered structure which can be studied using the SPR phenomenon [141]. SPR is a label-free highly sensitive

optical phenomenon which can yield a perceptible change in RI due to minuscule changes in RI of the film deposited onto the gold chip of the SPR instrument [1].

5.2 Experimental Procedure

The H-shaped liquid crystal (HLC) molecule was synthesized in the laboratory. The synthesis is briefly described in the supplementary information. The HLC molecule exhibits liquid crystalline phases as: crystal 45°C smectic & 78°C isotropic. The molecule exhibited nitro groups which can provide sufficient amphiphilicity for them to form a stable Langmuir monolayer at the air-water interface. The chemical structure of the molecule is shown in Fig. 5.2.

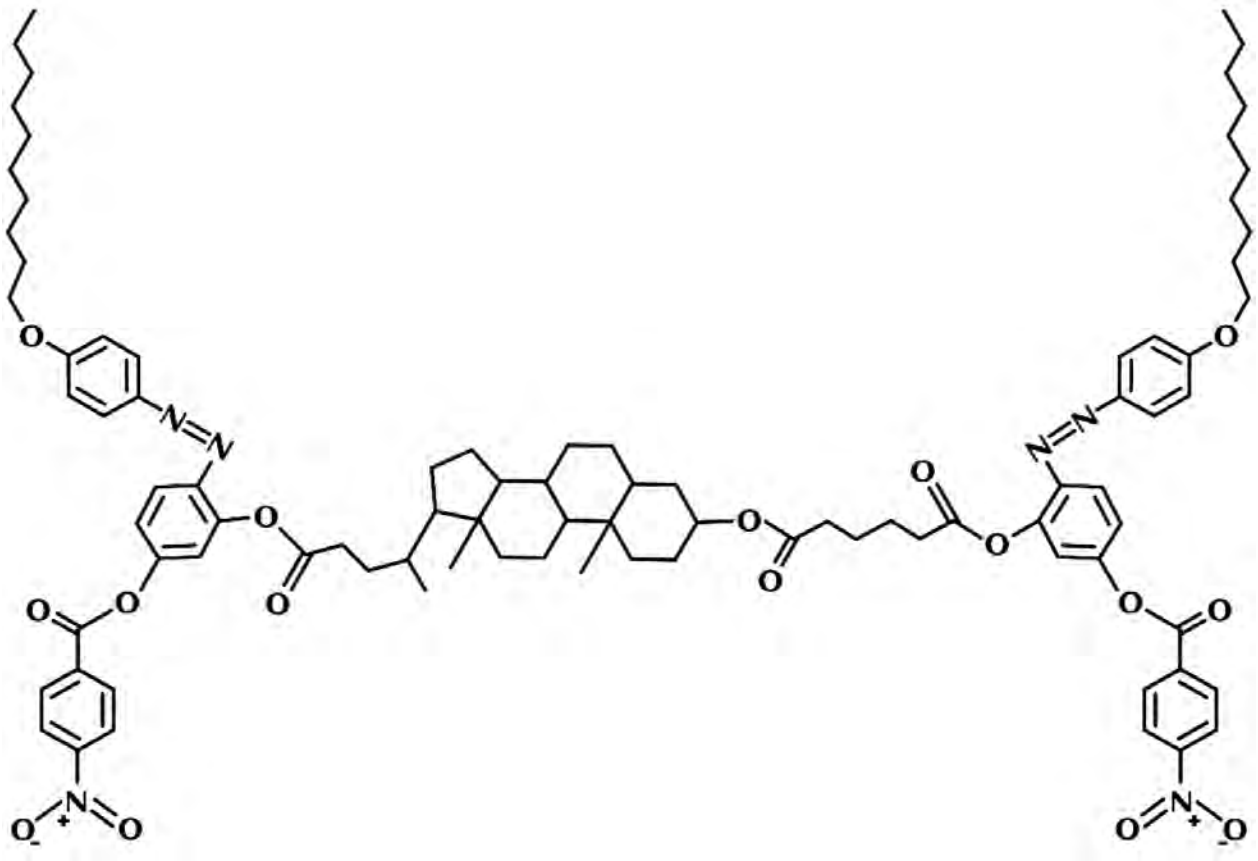

FIGURE 5.2: Chemical structure of H-shaped mesogenic liquid crystal molecule (HLC)Bis [5 – (4 – n – dodecyloxybenzoyloxy) – 2 – (4 – methylphenylazo) phenyl] adipate.

A 0.5 mg/ml clear solution was obtained by dissolving the HLC molecules in the high-performance liquid chromatography (HPLC) grade chloroform (Merck). The molecules were spread onto quartz substrate by drop-casting method, and the UV absorption spectrum of the molecules was recorded in the transmission mode. The solution of the HLC molecules was spread dropwise using a micro syringe (Hamilton) on the surface of ultrapure ion-free water (MilliQ) in a Langmuir-Blodgett trough (KSV NIMA). The trough was equipped with coupled double barriers for symmetric compression of the monolayer. About 15 minutes time was allowed for the solvent to evaporate from the surface of the water, leaving behind the dispersed HLC molecules. The monolayer was compressed at a speed of 5 mm/min and the surface pressure (Π) -area per molecule (A_m) isotherm was recorded. The monolayer at the air-water interface was imaged using a Brewster angle microscope (MicroBAM, KSV NIMA). The Brewster angle microscope (BAM) was equipped with a 50 mW laser of wavelength 659 nm.

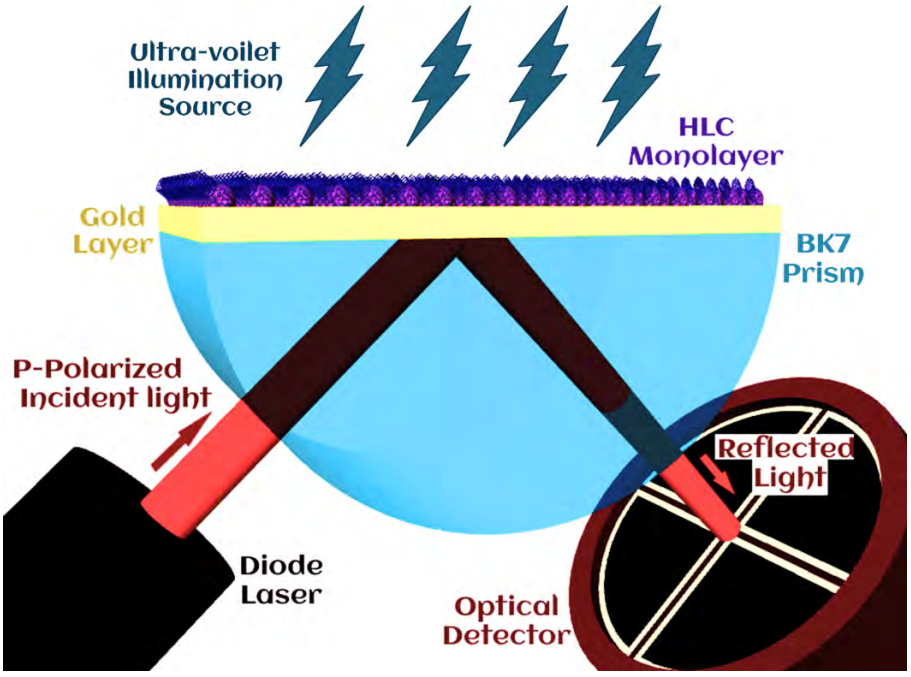

FIGURE 5.3: Upgraded SPR setup with UV illumination.

The Langmuir monolayer of the HLC molecules was transferred onto solid substrates through the LB technique at a target surface pressure (Π_t) of 15 mN/m. The substrates used in our studies were one-side polished silicon wafers (Ted Pella), gold-deposited quartz wafers

(SRS, USA), and the SPR chip consisting of Cr/Au layers deposited on BK7 glass (RI=1.51) substrates. The SPR chips were fabricated in the laboratory by depositing chromium (Cr) film of thickness 4 nm followed by a gold layer of thickness 50 nm on the BK7 glass substrates. The metal deposition was done using a DC sputter (Quorum). The morphology of the LB films of the HLC molecules was obtained using a field emission scanning electron microscope (FESEM, Zeiss Sigma). The SPR measurements were performed using a home-built setup developed in the Kretschmann configuration [93]. This configuration is based on angular interrogation wherein the angle of incidence is changed at a high resolution and reflected intensity is recorded simultaneously. The angular resolution of the setup was 5 μrad. Using the standard glucose solutions, the sensitivity of the equipment was obtained as 195 °/RIU.

In order to irradiate the LB film of the HLC molecules with a UV source during the SPR measurement, the SPR instrument was modified as shown in the schematic (Fig. 5.3). In the SPR setup, a provision was made to irradiate the LB film deposited onto the gold chip using an external UV source.

The UV source exhibited a spectrum (Fig. 5.4). The spectrum reveals a predominant peak at around 350 nm which will be sufficient to facilitate the $\pi - \pi^*$ transition in the HLC molecules [142].

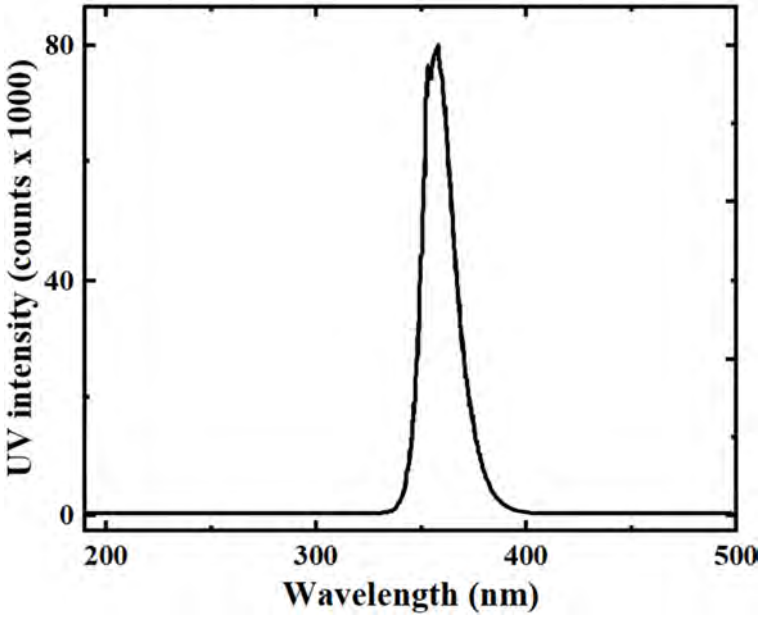

FIGURE 5.4: The characteristics spectrum of the UV source.

5.3 Results and discussion

The absorption spectrum of the HLC molecules spread onto quartz substrate is shown in Fig. 5.5. The major absorption peaks were seen at 220, 256, and 357 nm. The absorption peak corresponding to 357 nm is due to the $\pi - \pi^*$ transition. The absorption at 357 nm can cause a trans-cis transformation of the azo-groups of the HLC molecules. The cis-transformed molecules can switch back to trans configuration on exposure to ambient light or even in the dark state [117].

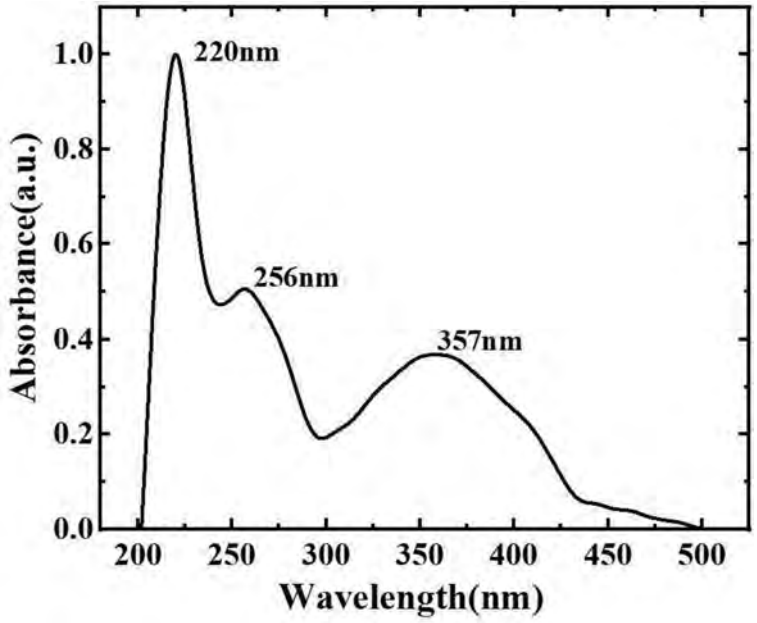

FIGURE 5.5: The absorption spectrum of HLC molecules.

The morphological change in the azo-based molecules due to the incidence of electromagnetic waves can be used potentially as optical switches. Similarly, for a waveguide application [143], it is essential to control the refractive index (RI) using external parameters. In this study, we report control of RI due to photoinduced isomerization of HLC molecules in ultrathin LB film.

The Π - A_m isotherm of HLC molecules at the air-water interface under the dark condition is shown in Fig. 5.6. The dark condition was chosen to ensure that all the azo-group of the molecules should exist in a trans-state before the deposition of ultrathin film using the LB technique. The isotherm of the monolayer of HLC molecules shows a classical trend. It

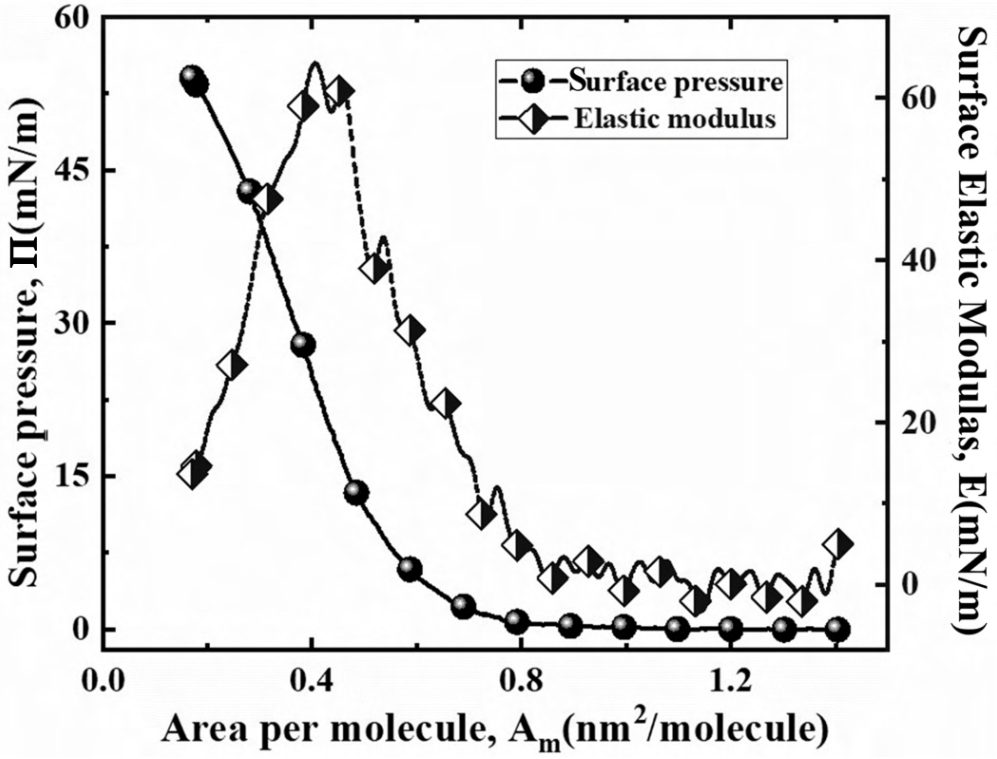

FIGURE 5.6: Surface pressure (Π) -area per molecule (A_m) isotherm and the corresponding in-plane surface elastic modulus (E) - (A_m) of Langmuir monolayer of HLC molecules at the air-water interface.

shows a startup rise in surface pressure at around 0.7 nm^2. The surface pressure continues to rise monotonically thereafter till a change in slope is noticed at 0.3 nm^2. This might be the initiation of a collapsed state. In-plane surface elastic modulus (E) is calculated from the Π - A_m isotherm using the relation E = - A_m (dΠ/dA_m) and shown in Fig. 5.6. A maximum value of E was found to be 65 mN/m at around 0.4 nm^2. This value may indicate a liquid-like phase of the HLC monolayer at the air-water interface [102]. The images of the monolayer at the air-water interface were captured using a BAM. These are shown in Fig. 5.7. The image captured at 1.0 nm^2 shows the coexistence of two features, dark and bright domains (Fig. 5.7(a)). The dark region represents the gas phase whereas the bright domains may represent a liquid-like phase of the HLC monolayer. On further compression, the bright domains merge to yield a homogeneous bright texture (Fig. 5.7(b)). This is the uniform liquid-like phase of the monolayer of HLC molecules. A close observation of the BAM image of the liquid-like phase shows some patchy texture.

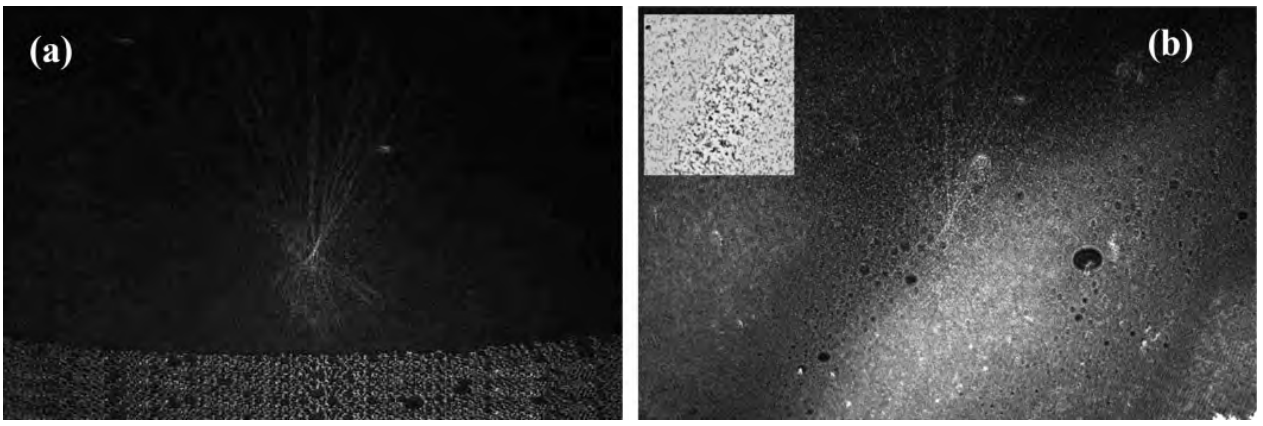

FIGURE 5.7: The BAM images were taken at an area per molecule of (a) 1.0 nm^2 and (b) 0.5 nm^2. The size of the images is 1.2×1.8 mm^2. The size of the inset image is 275×225 μm^2.

The area of the HLC molecule planar to the water surface (face-on) is estimated to be 4 nm^2 whereas the vertical to the water surface (edge-on) configuration is estimated to be 0.35 nm^2. The limiting area per molecule (A_o) for the liquid-like phase was observed at 0.56 nm^2. This is higher than the edge-on configuration and less than the face-on configuration. It is therefore possible that the HLC molecules in the liquid-like phase can have edge-on conformation with tilted molecules as shown in the schematic Fig.5.8 (left).

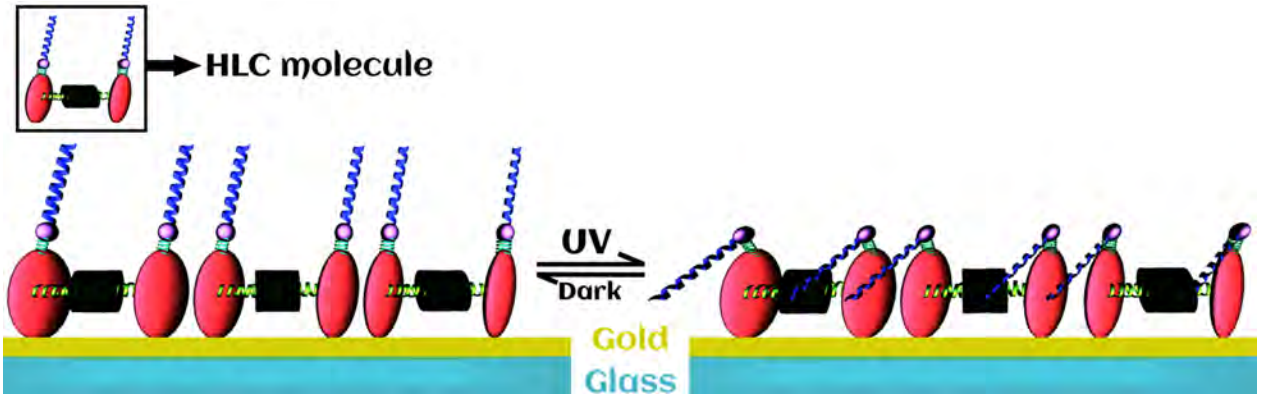

FIGURE 5.8: Trans-Cis transformation of HLC molecules due to irradiation with EM wave. One HLC molecule is shown in the top-left box.

As per the variation of E - A_m (Fig. 5.6), the maximum E value was obtained at about 22 mN/m. Compression beyond this can lead to instability in the monolayer, as it approaches near collapse. In order to achieve a stable LB film in a highly compressed and stable state, a

target surface pressure of 15 mN/m was chosen for LB deposition. This pressure corresponds to the liquid-like phase of the HLC monolayer. The morphology of the LB film deposited onto the silicon substrate was obtained using FESEM and shown in Fig. 5.9. The image shows a very interesting pattern. The dark background is due to the Si wafer whereas the bright strand-like domains are due to HLC molecules in the LB film. The bright strand domains are mostly curvy in nature and they assemble to form flower-like patterns. The pattern does not exhibit any backbone which rules out the possibility of dendritic growth during natural crystallization. Since the HLC molecule exhibits several chiral centers, it facilitates the strand-like domains to bend. The pattern observed in the FESEM image is due to the forced assembly of the HLC molecules under the constrained experimental conditions during LB film deposition in the liquid-like phase of the monolayer.

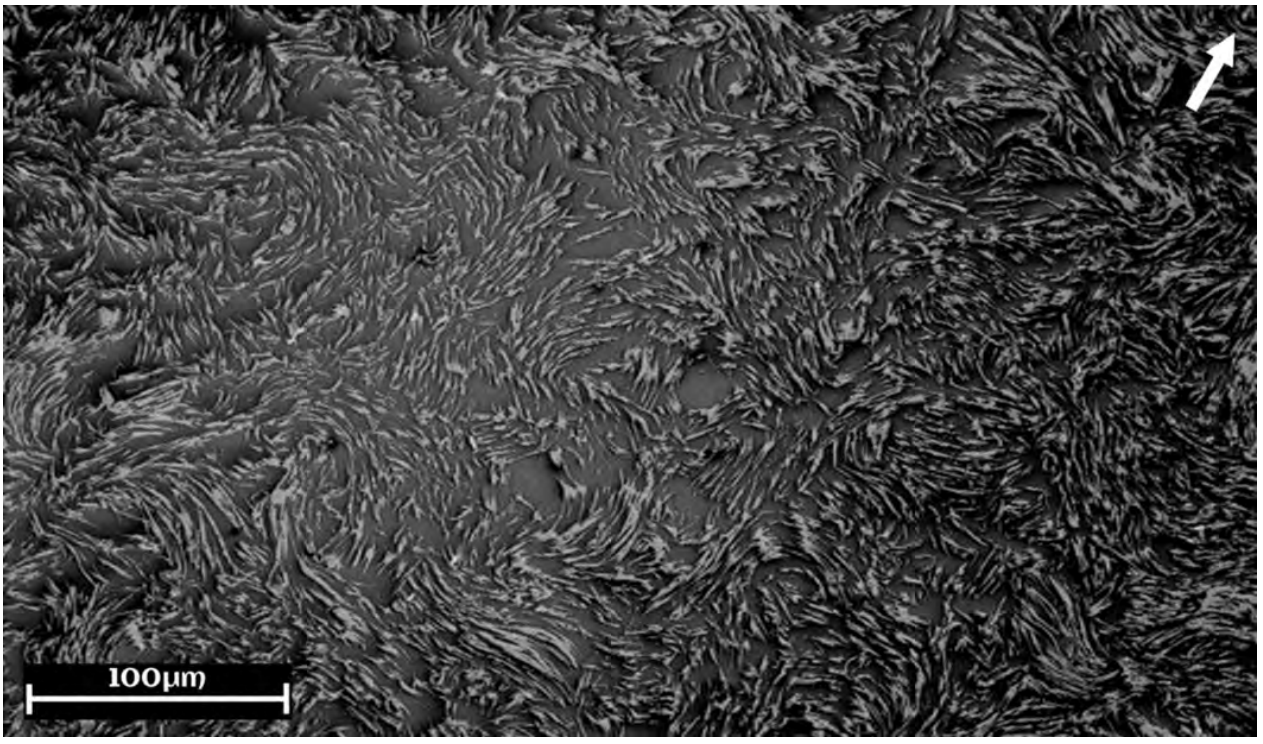

FIGURE 5.9: FESEM images of LB film of HLC molecules deposited on a silicon substrate at a surface pressure of 15 mN/m. The arrow in the image represents the dipping direction of the substrate during the LB film deposition.

The HLC molecules in the LB film can provide access to its azo-groups which can be photoinduced by the application of suitable electromagnetic waves. As observed from the

absorption spectrum (Fig. 5.5) of the HLC molecules, an incidence of UV radiation can facilitate the trans-cis transition in the molecules which can thereby change the morphology of the molecules in the LB films. The trans-cis transformation in the molecules can be perceived by a high-resolution and sensitive optical phenomenon viz. surface plasmon resonance (SPR). The morphological change in the ultrathin film can lead to changes in the refractive index (dielectrics) of the film which can be measured using the SPR phenomenon. In recent reports from our group, it has been observed that the morphological changes in aliphatic chains on organic molecules can be measured using the high-resolution SPR phenomenon [132, 144]. In this chapter, trans-cis isomerization in the HLC molecules in the LB film was photoinduced by irradiation with UV electromagnetic wave. The cis-configured molecules can switch back to trans-configuration due to irradiation with an ambient light/dark state.

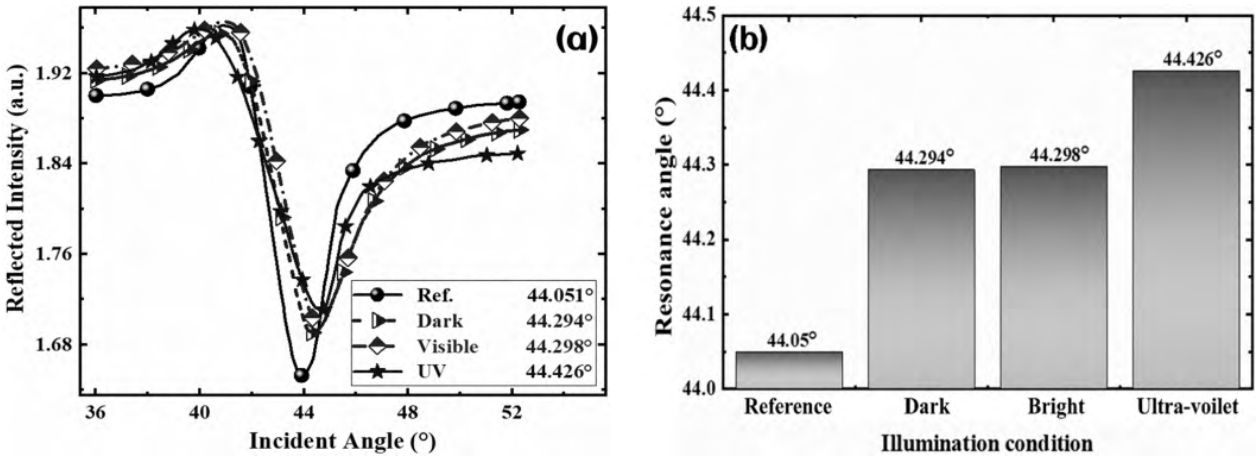

FIGURE 5.10: (a) SPR spectra and (b) the corresponding resonance angle (RA) obtained from LB films of HLC molecules deposited in the liquid-like phase under different illumination conditions. The dark and bright illumination represents the experiment performed with ambient light switch-off and switch-on, respectively.

The LB film of HLC molecules was deposited in the liquid-like phase at a target surface pressure of 15 mN/m on the sensing chip of the SPR instrument. The SPR spectra were collected by changing the angle of incidence and recording the reflected intensity. At resonance, the reflected intensity reduces to a minimum which indicates the highest energy transfer from incident EM wave to surface plasmon polaritons. The angle of incidence at minimum reflected intensity is termed a resonance angle (RA). A perturbation in the thin film due to some external parameter can change the dielectrics (refractive index) of the film which in turn can

shift the resonance angle. A measure of the shift in resonance angle can be quantified in terms of change in the refractive index using the standard Fresnel's theory of reflection from interfaces [145].

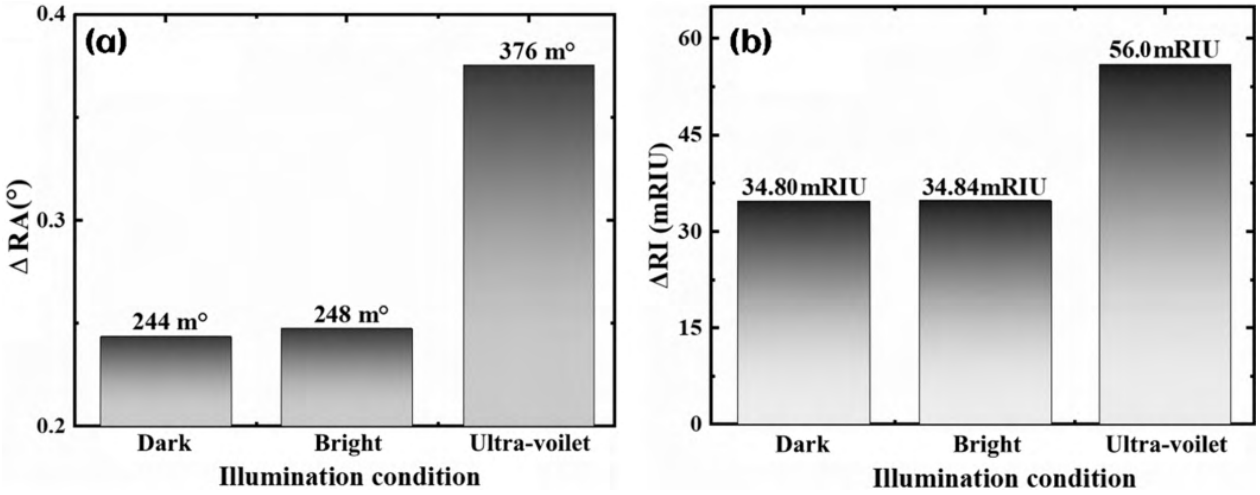

FIGURE 5.11: (a) Shift in resonance angle (ΔRA) with respect to the reference (gold/air) SPR spectra and (b) the corresponding change in refractive index (ΔRI) obtained from LB films of HLC molecules deposited in the liquid-like phase under the different illumination conditions. The dark and bright illumination represents the experiment performed with ambient light switch-off and switch-on, respectively.

Fig. 5.10(a) shows the SPR spectra of LB film of HLC molecules under the influence of irradiation with different illumination conditions. The shift in the spectra towards a higher angle of incidence as compared to that of reference (gold/air) indicates dielectric perturbation due to the deposition of LB films of HLC molecules and its dependency on irradiation with EM waves. It can be noted from the bar diagram (Fig. 5.10(b)) that RA measured under dark and bright states is nearly the same. This may indicate that the structural perturbation is not induced either in the dark or bright state of the experimental measurements. The RA shifted to higher values due to irradiation with UV light. This is due to the trans-cis transformation of the HLC molecules due to the UV light leading to a change in the refractive index of the film. The shift in resonance angle (ΔRA) with respect to the reference (gold/air) and the corresponding change in refractive index (ΔRI) of the LB film of HLC molecules under the different illumination conditions is shown in Fig. 5.11. The RI was calculated using Fresnel's reflection theory for a stack of layers [141]. The change in RI due to the deposition

of LB film is found to be 34.8 mRIU. This value remains invariant either in the dark state or in the bright state. However, a significant increase in the value of ΔRI (56 mRIU) was found when the LB film was irradiated with UV light. This is due to a trans-cis conformational change in the HLC molecules of the LB film. We have observed full recovery of the cis-state to trans-state by simply maintaining the dark condition during the SPR measurement.

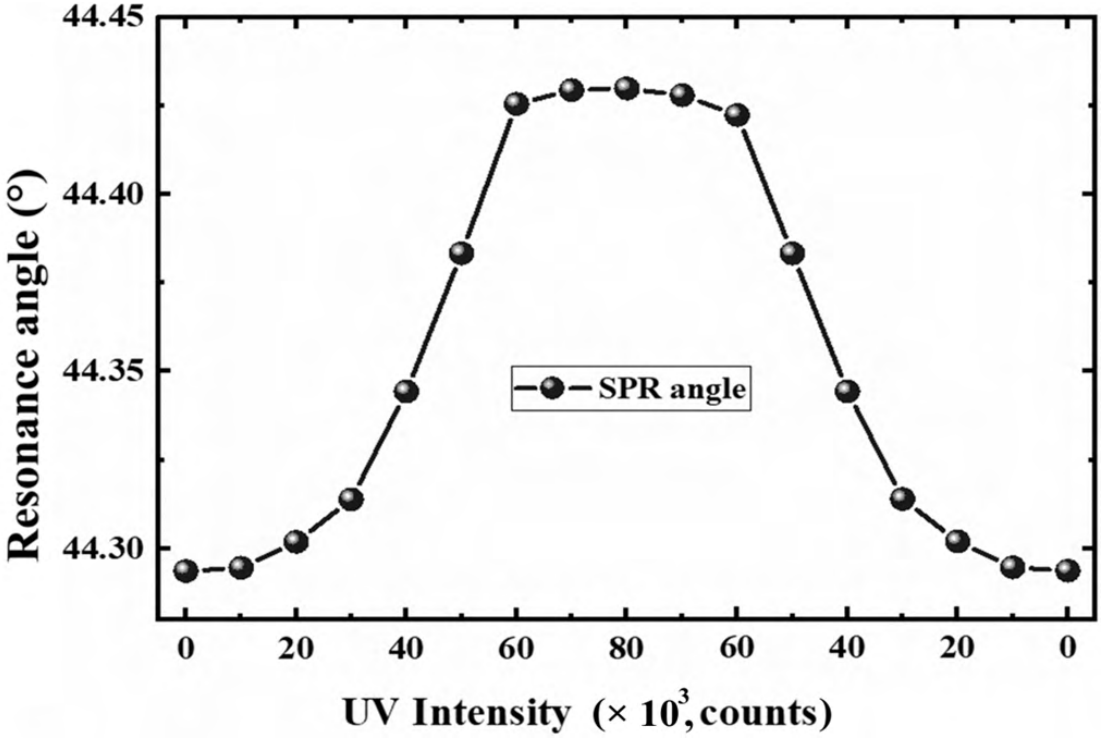

FIGURE 5.12: Optical switching due to UV illumination.

The morphological changes due to UV irradiation-induced isomerization can find potential applications in the field of optical switches and RI-modulated waveguides. The extent of isomerization was explored by increasing the intensity of the UV radiation and measuring the RA, simultaneously. This is shown in Fig. 5.12. It appears from the curve that there is a threshold intensity of 10000 counts of UV radiation below which the isomerization does not take place. The RA rises monotonically thereafter till it reaches its maximum at 60000 counts. The RA saturates above 60000 counts of the incident UV radiation. This cycle repeats perfectly which indicates that there is no permanent deformation in the molecular conformation due to the UV irradiation and complete recovery of the molecules from cis to

trans-state. The UV radiation above 60000 counts can switch the number of molecules to the highest extent. These features are a good indication of the optical switch. The modulation in RA can be looked upon as the equivalent modulation of the refractive index of the LB film. Therefore, our studies suggest a precise control of the refractive index of thin film as a function of the intensity of UV radiation. The normalized rate of isomerization (NRI in %) is calculated from the slope of RA Vs intensity curve of Fig. 5.12 and shown in Fig. 5.13. The NRI can be useful for the prediction of switch-on and switch-off intensity. The intensity below 10% of NRI and above 90% of NRI can be considered as the switch-off and switch-on intensity of the optical device. It can be noted from Fig. 5.13 that the switch-on and switch-off intensity of the optical device based on LB film of HLC molecules are 13000 and 46000 counts, respectively.

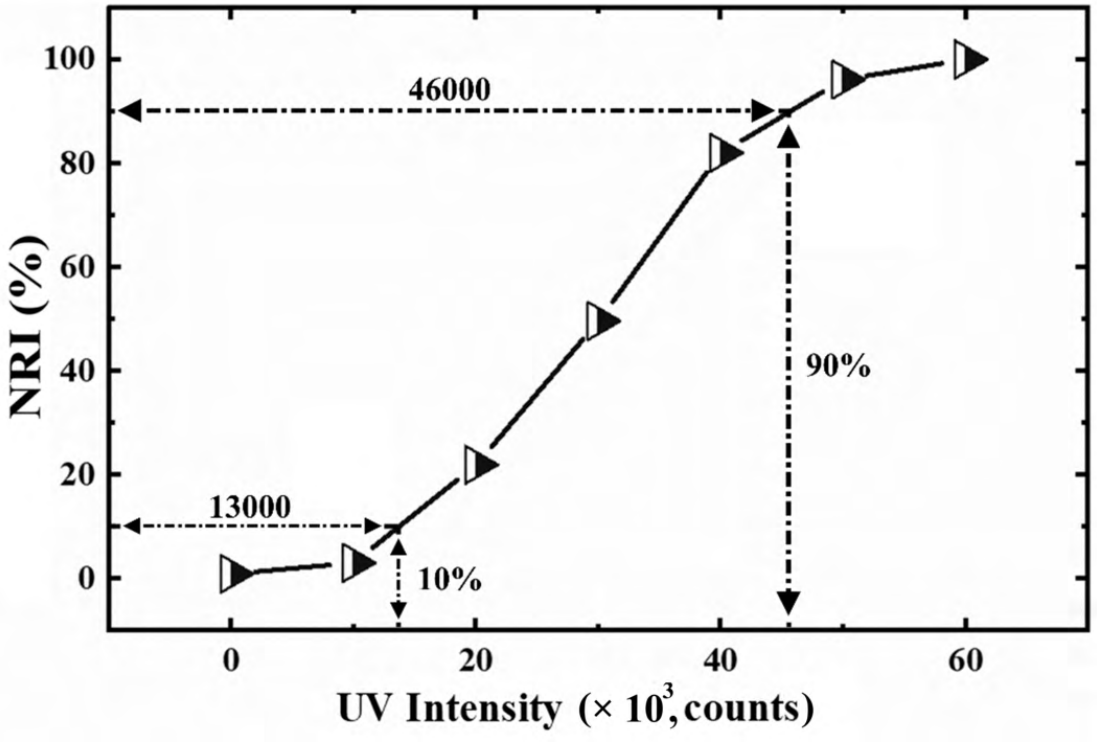

FIGURE 5.13: Normalized rate of isomerization (NRI) of the HLC molecules in the LB film as a function of the intensity of UV light irradiation.

5.4 Conclusion

In this chapter, we demonstrate that the HLC molecules exhibiting optically switchable Azo-groups can form a very stable Langmuir monolayer at the air-water interface. The monolayer exhibited gas and liquid-like phases. A highly optically active layer was created by the deposition of LB film of the HLC molecules in the liquid-like phase. The photo-isomerization of the azo-group of the HLC molecules in the LB film due to irradiation with UV light can lead to morphological change. Such morphological changes can lead to a minuscule change in the refractive index of the film which can be measured using a high-resolution and sensitive SPR phenomenon. A large change in the refractive index (56 mRIU) of the LB film of HLC molecules on irradiation with UV light was found. Such change clearly indicates the morphological transformation due to trans-cis isomerization of the HLC molecule due to irradiation with UV light. The study on the extent of isomerization indicates that the intensity of UV source less than 13000 and more than 46000 can be considered switch-off and switch-on of the optical device developed using the LB film of HLC molecules. This study also suggests that the LB film of the HLC molecule can be employed in optical waveguides wherein the local refractive index can be controlled by the suitable irradiation of UV light.

Chapter 6

Conclusion, future scopes and preliminary results

In this thesis, we report the development of an efficient, low-cost, and yet sensitive SPR device for traditional sensing applications and non-traditional measurements viz. birefringence in ultrathin films. The instrument was fully computer controlled with a very high range of the angular scan. The sensitivity was found to be around 1.92 μRIU with a very high resolution of μ° (Chapters 1 & 2) The instrument was used for sensing volatile gases, e.g., acetone and ethanol using the self-assembled nanoribbons of liquid crystalline molecules (Chapter 3). The ultrasensitive layered structure was formed by depositing SAM of MUA followed by LS of 8CB. The layered structure was perturbed by the polarization of an external EM wave. This work demonstrates control over the sensitivity of an SPR instrument using the polarization of the external EM wave (Chapter 4). The SPR instrument was used to measure the optical switching of liquid crystal molecules by the incidence of a UV light source. The LC molecules exhibited an azo-group which can be isomerized by the incidence of suitable UV radiation (Chapter 5).

6.1 Future scopes

The development of the extremely sensitive SPR-based optoelectronic sensor with a novel approach that provides high resolution and accuracy due to its feedback mechanism. The developed instrument is capable of almost all types of sensing applications, including bio-analysis. There is an enormous future scope in the field. Among the various important developments, some of the advanced modifications of the instrument were attempted by us. Here, we discuss the future scope of the equipment in terms of its development, viz. electrochemical SPR (ESPR), SPR imaging Fluorescence (SPRIF), and a NanoSPR (miniaturized standalone system).

6.2 Preliminary results

Surface plasmon resonance (SPR) is one of the popular optical phenomena which promises remarkable applications in the field of sensors. The sensing technology employing the SPR phenomenon has been improving gradually. A sensor based on the multiparameter measurement is highly reliable and practically impactful [146, 147]. Thus, there are several attempts in different areas of the development of a multiparameter measurement system.

The electronic nose is an example of the integration of multiple electrochemical sensors, which can be used to address multi-analyte independently in a given medium. There are several reports on sensing using electronic-nose [148]. The reports in the literature indicated the advantages of multichannel sensors for dealing with real samples. Here, the sensing area of different channels can be functionalized differently to address different analytes. Hence, a real sample consisting of a number of analytes can be analysed using such devices directly without undergoing the complex sample preparation procedures. There is another way to analyze the real samples by measuring several physical parameters simultaneously in a synchronous manner. Such measurement enhances the reliability of the sensors developed to work for real samples. Hence, there are few attempts to integrate several physical properties measurement units in a multiparameter measurement sensing unit, which can be trained to work efficiently

for real samples in wider ambient conditions [149, 150]. In this regard, the research work relevant to various device integration with our SPR unit is discussed here.

The prism-based Kretschmann configuration of the SPR setup offers very high sensitivity and resolution. During sensing, in addition to the change in RI, several other changes in physical parameters can take place in the active area of the transducer. Some of the significant changes are electrochemical, mass, and optical due to electronic transition, vibrational bands, etc. The development of a multiparameter system may include a provision to measure these physical properties simultaneously. Electrochemical-SPR (ESPR) is getting large scientific attention as electrochemical change is the most commonly observed phenomenon in sensing platforms. Therefore, simultaneous and real-time measurement of electrochemical and optical (RI) properties can offer a robust sensing platform by revealing their dependencies for specific analytes and thereby a strong mathematical pattern for decision-making.

SPRIF is the process to image the SPP wave, which propagates on the surface of the SPR chip and can be imaged using some optical arrangements/setup. The generated SPP waves are poorly intense to the image. Thus, the enhancement of SPP intensity is achieved by surface functionalization with some dye ligands. These dye ligands absorb the radiation emitted by SPP and radiate extremely intense electromagnetic waves in response which can be easy to capture/image with some optical/microscopic arrangements/setup.

6.2.1 Electrochemical SPR (ESPR)

Electrochemical SPR (ESPR) allows the SPR observations to be simultaneous with the electrochemical measurements. The integration of the electrochemical unit with our SPR equipment allows for measuring the changes in the physical properties of the sensing surface during the SPR phase. In ESPR, the gold surface of the SPR chip is used for the excitation of SPP, and the same surface is used as the working electrode (WE) for electrochemical measurements.

The integration of electrochemistry with the SPR (ESPR) can reveal valuable information related to the charge transfer mechanism in the electrolyte on the sensing chip of the SPR.

Thus, our SPR equipment was customized to integrate the electrochemical setup. The schematic of the ESPR setup is shown in Fig. 6.1(a). The homogeneous distribution of analytes is necessary for precise and accurate analysis. Thus, a compatible electrochemical flow cell (ECFC) is designed to integrate with our SPR unit, as shown in Fig. 6.1(b). The flow cell provides an easy way for uniform distribution of the analytes on the active area of the sensing chip. The SPR sensing chip was used as the working electrode (WE), while Platinum and Ag/AgCl were used as the counter electrode (CE) and reference electrode (RE) respectively.

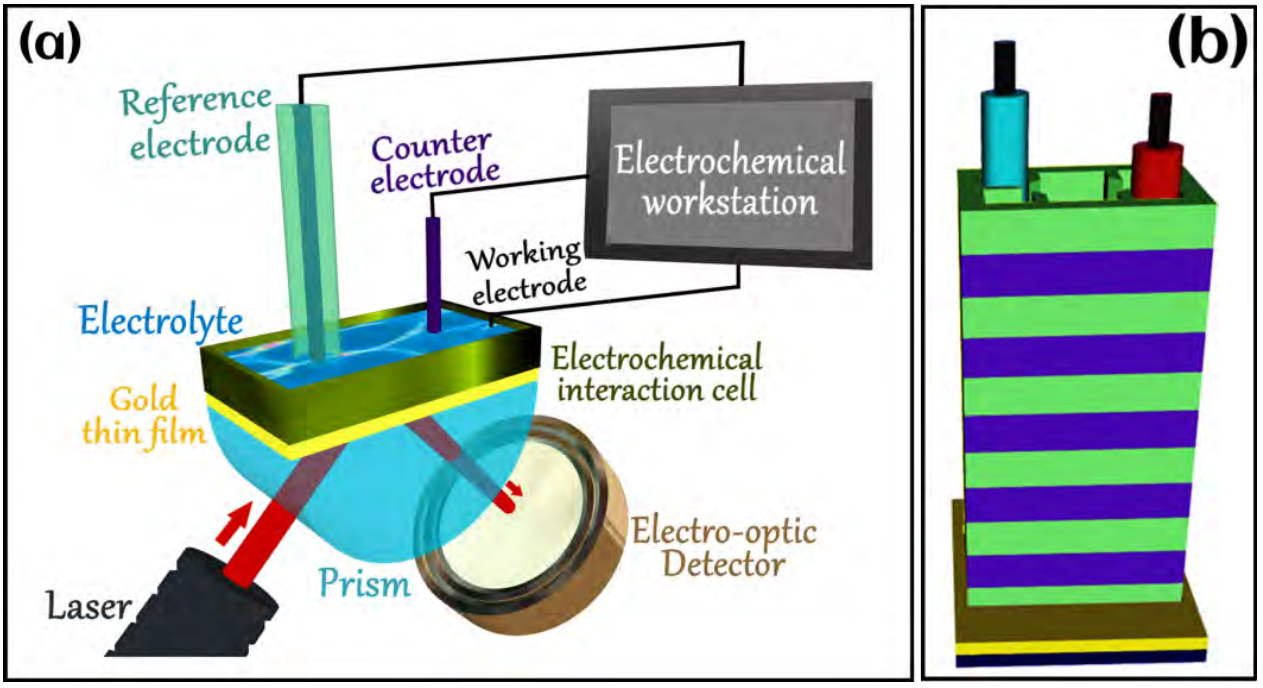

FIGURE 6.1: (a) Schematic of electrochemical SPR system. (b) Schematic of an electrochemical flow cell.

The calibration was done using the KCl and polyvinyl alcohol (PVA) + KCl (1M) dissolved in 10 ml of ultrapure ion-free water medium. The electrochemical cyclic voltammogram (CV) was obtained by changing the voltage at a rate of 0.1 V/m. As the voltage sweeps, the change in SPR response is recorded as a shift in resonance angle simultaneously.

The CV curves show the usual trend of current as a function of applied voltage without any significant redox peaks. The trend is more like a charge storage behavior. Therefore, the surface capacitance values were calculated using the formulas:

$$\text{Charge } (\text{mC/cm}^2) = \frac{\text{Integrated area of CV curve}}{2 \times \text{scan rate}} \tag{6.1}$$

$$\text{Capacitance } (\text{mF/cm}^2) = \frac{\text{Charge}}{\text{Potential window}} \tag{6.2}$$

The variation of surface capacitance as a function of the concentration of PVA in the aqueous medium is shown in Fig. 6.2(b). The slope of the linear trend of the capacitance is 40.9 mF/g-cm^2.

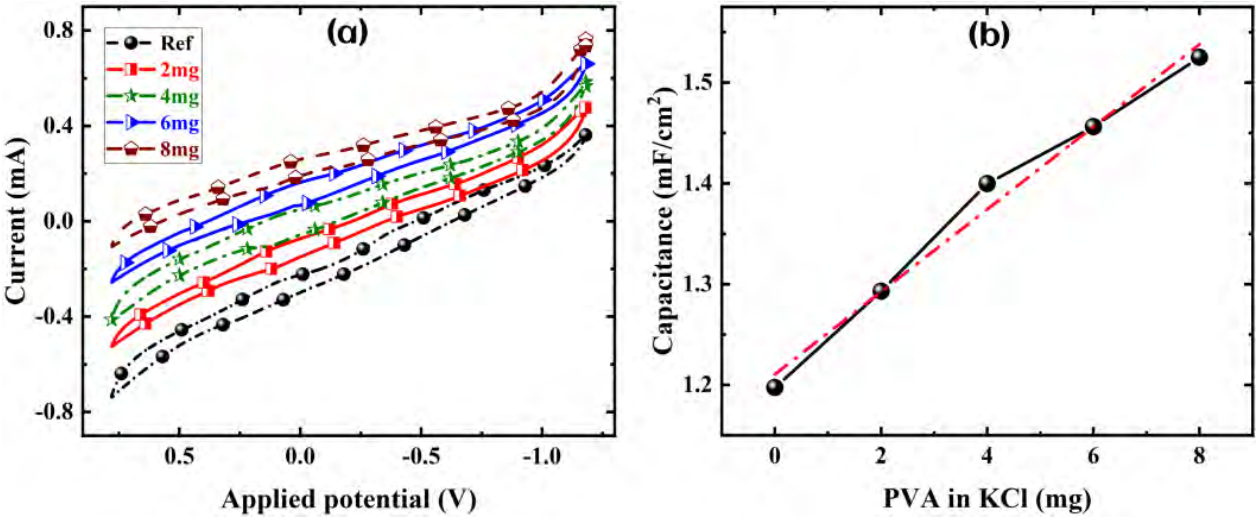

FIGURE 6.2: (a) Cyclic voltammogram curves for different concentrations of PVA dissolved in 10 mL of KCl (1M) solution of ultrapure ion-free water medium. (b) Calibration curve showing the variation of surface capacitance as a function of the concentration of PVA in the aqueous medium.

The change in capacitance occurs due to the change in the dielectric properties (i.e., RI) of the medium adsorbed over the gold surface. This change was measured by recording the shift in RA using the SPR (Fig. 6.3) as a function of change in the concentration of PVA in the aqueous medium possessing KCl. The calibration curve drawn from the SPR response is found to be linear with a slope of about 410.6 °/g (Fig. 6.3). The slope of the calibration curve is an indicator of the sensitivity of the device [90]. These measurements clearly indicate a dependency of electrochemical properties with the dielectric properties of the material at the

metal-dielectric interface. These properties can change due to the interaction of the analytes with the ligands immobilized over the gold surface of an ESPR system.

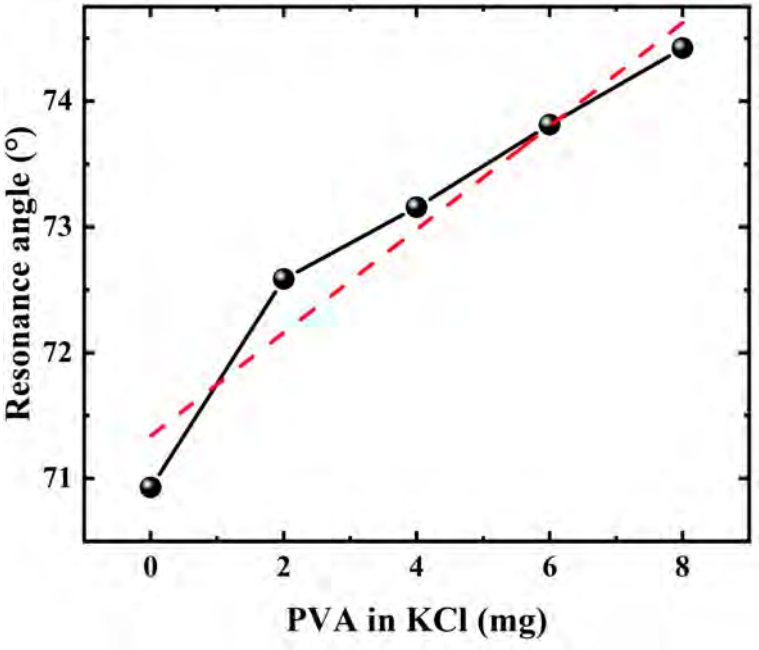

FIGURE 6.3: The calibration curve showing the resonance angle as a function of the concentration of PVA in the aqueous medium.

6.2.2 SPR Imaging using Fluorescence (SPRIF)

In the Kretschmann configuration, there are some attempts to image the plasmonic field on the metal surface. There are several articles showing that the localized SPR phenomenon can yield an intense electric field in a localized area. This field can be utilized to increase the absorption cross-section of the adjacent dielectric medium. The plasmonic field can therefore be employed to excite some radiative materials of high quantum yield. The absorptions of the plasmonic field by the fluorescent materials can facilitate the imaging of the field during the radiative process.

In general, the plasmonic fields on the gold surface in the Kretschmann configuration are very weak to observe using traditional microscopic techniques. Therefore, if the field is amplified through some means, it is possible to image the plasmonic field over the gold surface in the Kretschmann configuration.

A fluorescent material that exhibits a high absorption cross-section for the given experimental setup can be deposited over the gold surface for imaging the plasmonic field. The fluorescent molecules excited by the absorption of the plasmonic wave can undergo de-excitation and emit EM waves of lower energy (higher wavelength). The density of emitted radiation can be controlled either by altering the number density or enhancing the quantum yield of the fluorescent probes. In a preliminary study, we deposited Nile Red dye molecules and excited them using the plasmonic field over the gold surface in the Kretschmann geometry. The absorption and emission wavelength of Nile Red are 549 and 628 nm, respectively.

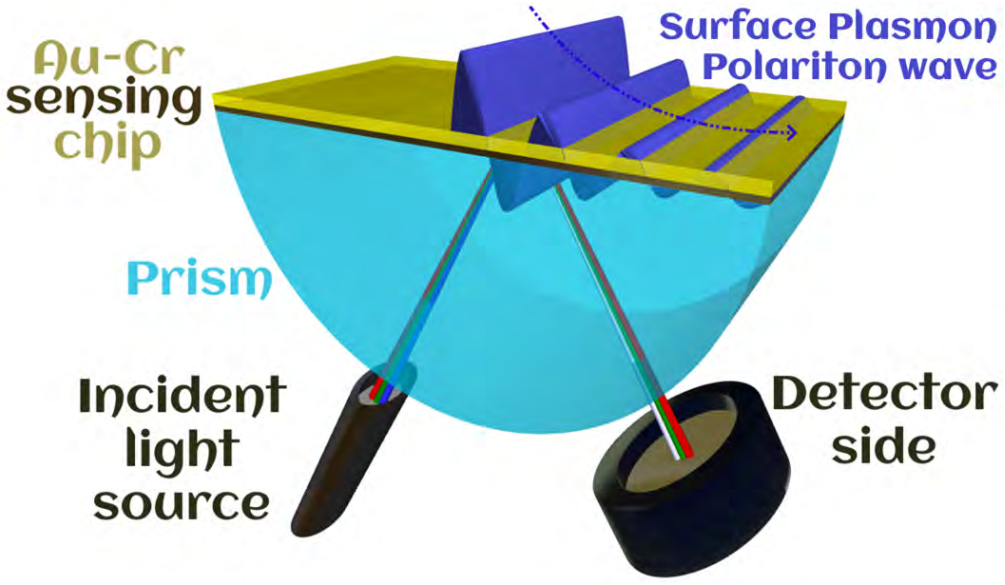

FIGURE 6.4: The schematic diagram of the prism-based Kretschmann SPR configuration.

Fluorescence is the immediate remission of different electromagnetic radiation caused by the electronic d-excitation of the dye molecules in response to the absorbed electromagnetic radiation. The initial excitation occurs through the absorption of a photon from the electromagnetic wave. It translates the free electrons from the ground state to the excited state. Then the remission occurs immediately as soon as the electromagnetic source is removed. Generally, the wavelength of the emitted wave is higher than the absorbed radiation. Fluorescence spectroscopy uses a beam of light that excites the electrons in molecules of certain compounds and causes them to remit the light with different energy. That light is directed towards a

filter and onto a detector for measurement and identification of the molecule or changes in the molecule.

The experimental setup of SPRIF developed in our research laboratory is shown in Fig. 6.5.

FIGURE 6.5: Experimental setup for SPRIF.

In order to image the plasmonic field, it is essential that the incident EM wave for the generation of the SPP wave should be compatible with the absorption band of the chosen fluorescent molecules. Accordingly, the resonance angle should be chosen to establish the phenomenon. Therefore, a calibration curve is obtained between the resonance wavelength and the angle of incidence. The calibration between the applied electromagnetic wavelength and the SPR angle was obtained using a standard gold chip for our SPR sensor. A monochromator was used in the incident optical geometry. The detector side includes various components of the Ocean Optics setup and QPD associated with the NI-DAQ system. Some LabVIEW-based GUI software programs were used for synchronized and precise computer-controlled observations. The SPR chip was functionalized with the 20μl of 1mg/ml Nile Red dye molecules by the drop-casting process. Then a resonance condition was obtained. The SPR angle was fixed and the fluorescence images of the dye ligands under this condition

were captured with high-resolution microscopic optics. The schematic representation of the experiment is shown in Fig. 6.6.

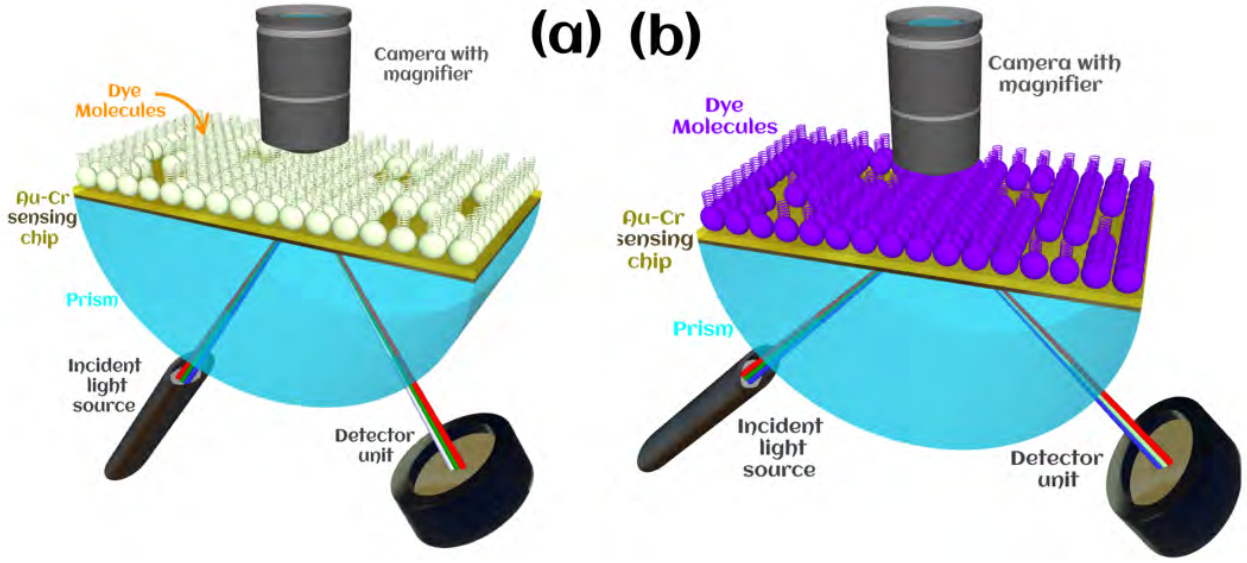

FIGURE 6.6: The schematic setup for the Kretschmann-based SPR setup was modified to observe SPR-assisted fluorescence images (a) dye-ligands in the ground state (b) dye-ligands in the excited state due to the SPR condition.

The SPRIF is calibrated in terms of the wavelength of the incident electromagnetic wave with respect to the resonance angle and is shown in Fig. 6.6. The integrated SPRIF unit indicates the exponential decay in the wavelength of the absorbed light spectrum with an increase in the SPR angle. This trend is fitted suitably with an exponential curve and the parameters are shown in the inset.

The microscopic images captured with the sensing chip functionalized with Nile Red are shown in Fig. 6.7. At the non-resonance incidence angle, the molecules of the dye-ligand are indicating the ground state. Thus, the dispersed Nile Red molecules are showing almost a dark color. At the angle of incidence 47.044°, the molecules initiate the emission of light-red color.

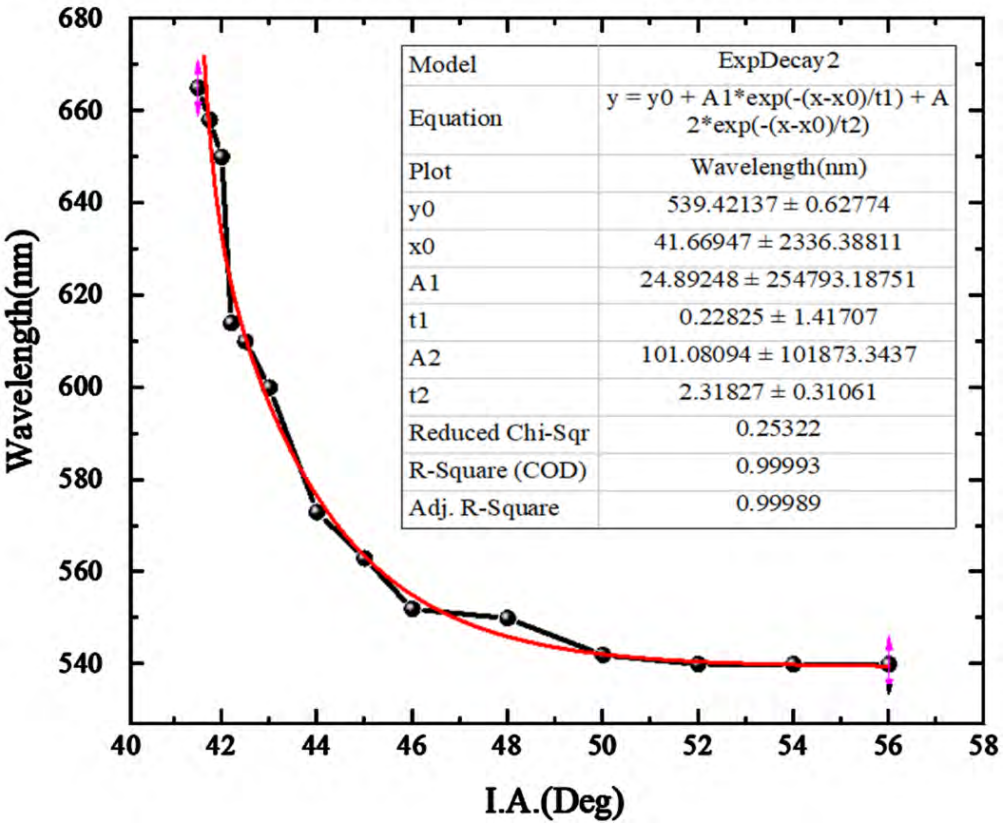

FIGURE 6.7: The calibration curve for the SPRF unit.

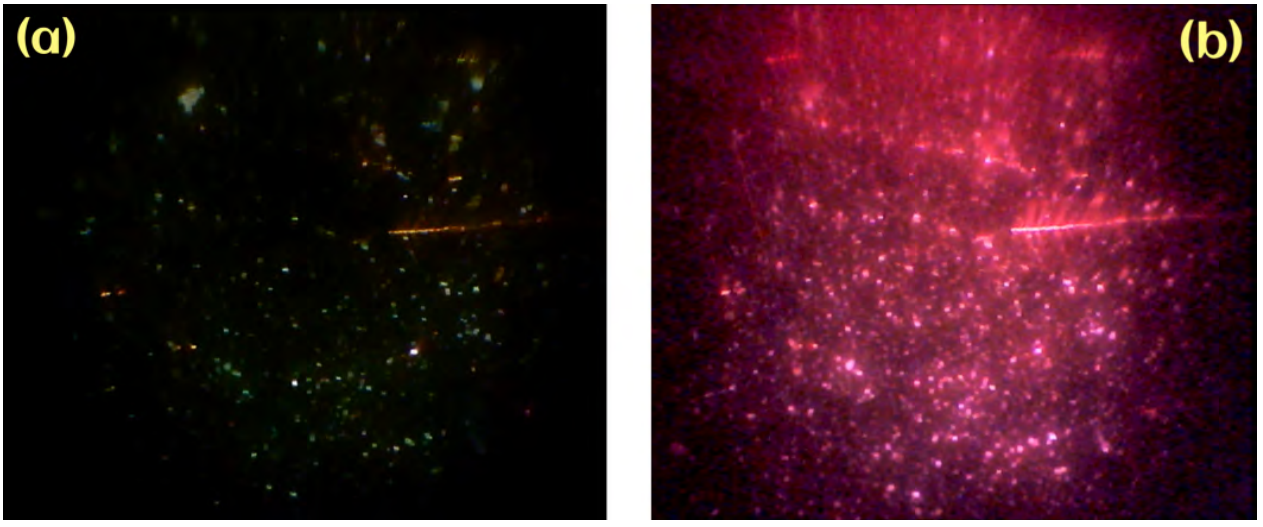

FIGURE 6.8: Microscopic images captured with the sensing chip functionalized with Nile Red. (a) without SPR condition (b) with SPR condition.

The absorption wavelength of Nile Red molecules is nearly 549 nm which emits nearly 628

nm in the excited state. At nearly 47°, the green light (549 nm) was absorbed in the metal-dielectric interface and produced the relevant evanescent wave, which is absorbed and amplified by the Nile Red molecules.

The Nile Red dye molecules remit the electromagnetic spectrum of light-red color (628 nm) in response to the absorption of the green wavelength which is satisfied with the red-shift of the electromagnetic spectrum with SPRIF. This experiment suggests that the imaging of plasmon waves is possible on a flat 2D metal surface.

6.2.3 NanoSPR (A handheld standalone lab prototype)

We are in the early stage of the development of a handheld, compact, and portable SPR device. The device may ensure SPR-based sensors are installed in the field and may be accessed remotely. The miniaturized version of the device is shown in Fig. 6.9. We are working on establishing the SPR phenomenon in the miniaturized optical setup followed by its calibration using some standards.

FIGURE 6.9: A miniaturized handheld version of the SPR device.

The upgraded SPR sensor with multi-channels and/or multi-parameters observations can enhance the sensing merits. The recorded data from the multi-parameters system can be processed by some advanced mathematical algorithms that robust the controls during sensing and make the outcomes reliable. Although extensive integrations are possible for various physical parameters (viz. luminescence, thermal, piezoelectric, electrochemical, etc.) for the SPR sensors, here we demonstrated the integration of our SPR sensor with the electrochemical and fluorescence microscopic setup separately and some of their application. The field of SPR is evolving tremendously due to its wider applications ranging from bio-medical, pharmaceutical, photonics, and fundamental research. This thesis presents a complete package by including the instrumentation, some traditional sensing, and non-traditional applications, computational techniques for data analysis, and the future scope. This thesis can provide crucial research and development opportunities for scientists working in this field.

References

[1] R. K. Gupta. "Sensing through surface plasmon resonance technique". In: *Reviews in Plasmonics*. Cham: Springer International Publishing, 2017, 39–53. ISBN: 9783319480800. DOI: 10.1007/978-3-319-48081-7_3.

[2] Hao Li and Lizhi Zhang. "Photocatalytic performance of different exposed crystal facets of BiOCl". en. In: *Current opinion in green and sustainable chemistry* 6 (2017), 48–56. ISSN: 2452-2236. DOI: 10.1016/j.cogsc.2017.05.005. URL: https://www.sciencedirect.com/science/article/pii/S2452223617300494.

[3] Andreas Otto. "Excitation of nonradiative surface plasma waves in silver by the method of frustrated total reflection". en. In: *Zeitschrift für Physik A Hadrons and Nuclei* 216.4 (1968), 398–410. ISSN: 0939-7922. DOI: 10.1007/bf01391532. URL: http://dx.doi.org/10.1007/bf01391532.

[4] I. Pockrand et al. "Surface plasmon spectroscopy of organic monolayer assemblies". en. In: *Surface science* 74.1 (1978), 237–244. ISSN: 0039-6028. DOI: 10.1016/0039-6028(78)90283-2. URL: https://www.sciencedirect.com/science/article/pii/0039602878902832.

[5] Richard B. M. Schasfoort and Anna J. Tudos. *Handbook of surface plasmon resonance*. Cambridge, England: Royal Society of Chemistry, 2008. ISBN: 9780854042678.

[6] E. Kretschmann and H. Raether. "Notizen: Radiative decay of non radiative surface plasmons excited by light". en. In: *Zeitschrift für Naturforschung A* 23.12 (1968), 2135–2136. ISSN: 0932-0784. DOI: 10.1515/zna-1968-1247. URL: https://www.degruyter.com/document/doi/10.1515/zna-1968-1247/pdf.

[7] T. Turbadar. "Complete absorption of light by thin metal films". In: *Proceedings of the Physical Society* 73.1 (1959), 40–44. ISSN: 0370-1328. DOI: 10.1088/0370-1328/73/1/307. URL: https://iopscience.iop.org/article/10.1088/0370-1328/73/1/307/meta.

[8] Jieyao Li et al. "Multi-channel surface plasmon resonance biosensor using prism-based wavelength interrogation". en. In: *Optics express* 28.9 (2020), p. 14007. ISSN: 1094-4087. DOI: 10.1364/oe.389226. URL: https://opg.optica.org/abstract.cfm?uri=oe-28-9-14007.

[9] J. Guo, Z. Zhu, and W. Deng. "Small-angle measurement based on surface-plasmon resonance and the use of magneto-optical modulation". en. In: *Applied optics* 38.31 (1999), 6550–6555. ISSN: 2155-3165. DOI: 10.1364/ao.38.006550. URL: https://opg.optica.org/abstract.cfm?uri=ao-38-31-6550.

[10] E. K. Akowuah, T. Gorman, and S. Haxha. "Design and optimization of a novel surface plasmon resonance biosensor based on Otto configuration". en. In: *Optics express* 17.26 (2009), 23511–23521. ISSN: 1094-4087. DOI: 10.1364/OE.17.023511. URL: https://opg.optica.org/abstract.cfm?uri=oe-17-26-23511.

[11] Hai-Sheng Leong et al. "Surface plasmon resonance in nanostructured metal films under the Kretschmann configuration". en. In: *Journal of applied physics* 106.12 (2009), p. 124314. ISSN: 0021-8979. DOI: 10.1063/1.3273359. URL: http://dx.doi.org/10.1063/1.3273359.

[12] Shuping Xu et al. "Surface-enhanced Raman scattering (SERS) based on surface plasmon resonance coupling techniques". en. In: *Frontiers of Chemistry in China* 6.4 (2011), 341–354. ISSN: 1673-3495. DOI: 10.1007/s11458-011-0258-1. URL: http://dx.doi.org/10.1007/s11458-011-0258-1.

[13] Huamin Liang et al. "Surface plasmon resonance instrument as a refractometer for liquids and ultrathin films". en. In: *Sensors and actuators. B, Chemical* 149.1 (2010), 212–220. ISSN: 0925-4005. DOI: 10.1016/j.snb.2010.05.048. URL: https://www.sciencedirect.com/science/article/pii/S0925400510004569.

[14] K. Sathiyamoorthy et al. "Modified two prism SPR sensor configurations to improve the sensitivity of measurement". en. In: *Sensors and actuators. A, Physical* 191 (2013), 73–77. ISSN: 0924-4247. DOI: 10.1016/j.sna.2012.11.029. URL: https://www.sciencedirect.com/science/article/pii/S0924424712007108.

[15] Shaode Yu et al. "A consistency evaluation of signal-to-noise ratio in the quality assessment of human brain magnetic resonance images". en. In: *BMC medical imaging* 18.1 (2018), p. 17. ISSN: 1471-2342. DOI: 10.1186/s12880-018-0256-6. URL: http://dx.doi.org/10.1186/s12880-018-0256-6.

[16] Marijke Welvaert and Yves Rosseel. "On the definition of signal-to-noise ratio and contrast-to-noise ratio for fMRI data". en. In: *PloS one* 8.11 (2013), e77089. ISSN: 1932-6203. DOI: 10.1371/journal.pone.0077089. URL: https://journals.plos.org/plosone/article/file?id=10.1371/journal.pone.0077089\&type=printable.

[17] Jacob Beal. "Signal-to-noise ratio measures efficacy of biological computing devices and circuits". en. In: *Frontiers in bioengineering and biotechnology* 3 (2015), p. 93. ISSN: 2296-4185. DOI: 10.3389/fbioe.2015.00093. URL: http://journal.frontiersin.org/Article/10.3389/fbioe.2015.00093/abstract.

[18] Muhammad Hameed Siddiqi and Yousef Alhwaiti. "Signal-to-noise ratio comparison of several filters against phantom image". en. In: *Journal of healthcare engineering* 2022 (2022), p. 4724342. ISSN: 2040-2295. DOI: 10.1155/2022/4724342. URL: https://www.hindawi.com/journals/jhe/2022/4724342/.

[19] Abhishek Vikas Parab. "Improving confidentiality of watermark image through image filtering techniques". en. PhD thesis. Dublin, National College of Ireland, 2019.

[20] Ammar Haouimi and J. Yeung. *Signal-to-noise ratio (MRI)*. 2011.

[21] T.H. Le. *"high-performance magnetic resonance: Technical challenges and clinical applications"*. 2004. URL: https://appliedradiology.com/articles/high-field-high-performance-magnetic-resonance-technical-challenges-and-clinical-applications.

[22] Li-Hsing Ho, Shu-Yun Feng, and Tieh-Min Yen. "A new methodology for customer satisfaction analysis: Taguchi's signal-to-noise ratio approach". In: *Journal of service science and management* 07.03 (2014), 235–244. ISSN: 1940-9893. DOI: 10.4236/jssm.2014.73021. URL: http://www.scirp.org/Journal/Paperabs.aspx?paperid=47258.

[23] A. R. Mohd Syaifudin, K. P. Jayasundera, and S. C. Mukhopadhyay. "Novel planar interdigital sensors for detection of domoic acid in seafood". In: *Lecture Notes in Electrical Engineering*. Berlin, Heidelberg: Springer Berlin Heidelberg, 2011, 253–278. ISBN: 9783642179426.

[24] Els H. Gillis et al. "Development and validation of a biosensor-based immunoassay for progesterone in bovine milk". en. In: *Journal of immunological methods* 267.2 (2002), 131–138. ISSN: 0022-1759. DOI: 10.1016/s0022-1759(02)00166-7. URL: https://www.sciencedirect.com/science/article/pii/S0022175902001667.

[25] David A. Edwards. "Convection effects in the BIAcore dextran layer: surface reaction model". en. In: *Bulletin of mathematical biology* 68.3 (2006), 627–654. ISSN: 0092-8240. DOI: 10.1007/s11538-005-9023-2. URL: http://dx.doi.org/10.1007/s11538-005-9023-2.

[26] Allen D. Taylor et al. "Surface plasmon resonance (SPR) sensors for the detection of bacterial pathogens". In: *Principles of Bacterial Detection: Biosensors, Recognition Receptors and Microsystems*. New York, NY: Springer New York, 2008, 83–108. ISBN: 9780387751122.

[27] D. Nedelkov, A. Rasooly, and R. W. Nelson. "Multitoxin biosensor-mass spectrometry analysis: a new approach for rapid, real-time, sensitive analysis of staphylococcal toxins in food". en. In: *International journal of food microbiology* 60.1 (2000), 1–13. ISSN: 0168-1605. DOI: 10.1016/s0168-1605(00)00328-7. URL: https://www.sciencedirect.com/science/article/pii/S0168160500003287.

[28] Dobrin Nedelkov and Randall W. Nelson. "Detection of Staphylococcal enterotoxin B via biomolecular interaction analysis mass spectrometry". en. In: *Applied and environmental*

microbiology 69.9 (2003), 5212–5215. ISSN: 0099-2240. DOI: 10.1128/AEM.69.9.5212-5215.2003. URL: http://dx.doi.org/10.1128/AEM.69.9.5212-5215.2003.

[29] Anna J. Tüdös, Elly R. Lucas-van den Bos, and Edwin C. A. Stigter. "Rapid surface plasmon resonance-based inhibition assay of deoxynivalenol". en. In: *Journal of agricultural and food chemistry* 51.20 (2003), 5843–5848. ISSN: 0021-8561. DOI: 10.1021/jf030244d. URL: http://dx.doi.org/10.1021/jf030244d.

[30] Isa Mohammed et al. "Is biosensor a viable method for food allergen detection?" en. In: *Analytica chimica acta* 444.1 (2001), 97–102. ISSN: 0003-2670. DOI: 10.1016/s0003-2670(01)01166-7. URL: https://www.sciencedirect.com/science/article/pii/S0003267001011667.

[31] W. Haasnoot et al. "Direct biosensor immunoassays for the detection of nonmilk proteins in milk powder". en. In: *Journal of agricultural and food chemistry* 49.11 (2001), 5201–5206. ISSN: 0021-8561. DOI: 10.1021/jf010440p. URL: http://dx.doi.org/10.1021/jf010440p.

[32] Norio Miura et al. "Highly sensitive and selective surface plasmon resonance sensor for detection of sub-ppb levels of benzo%[a]pyrene by indirect competitive immunoreaction method". en. In: *Biosensors & bioelectronics* 18.7 (2003), 953–959. ISSN: 0956-5663. DOI: 10.1016/s0956-5663(02)00242-7. URL: https://www.sciencedirect.com/science/article/pii/S0956566302002427.

[33] E. Mauriz et al. "Optical immunosensor for fast and sensitive detection of DDT and related compounds in river water samples". en. In: *Biosensors & bioelectronics* 22.7 (2007), 1410–1418. ISSN: 0956-5663. DOI: 10.1016/j.bios.2006.06.016. URL: https://www.sciencedirect.com/science/article/pii/S0956566306002867.

[34] Kyungsik Ock et al. "Optical detection of Cu2+ ion using a SQ-dye containing polymeric thin-film on Au surface". en. In: *Microchemical journal, devoted to the application of microtechniques in all branches of science* 70.3 (2001), 301–305. ISSN: 0026-265X. DOI: 10.1016/s0026-265x(01)00133-3. URL: https://www.sciencedirect.com/science/article/pii/S0026265X01001333.

[35] D. R. Shankaran et al. "A novel surface plasmon resonance immunosensor for 2,4,6-trinitrotoluene (TNT) based on indirect competitive immunoreaction: a promising approach for on-site landmine detection". In: *IEEE sensors journal* 5.4 (2005), 616–621. ISSN: 1530-437X. DOI: 10.1109/jsen.2005.848150. URL: https://ieeexplore.ieee.org/document/1468116.

[36] J. Svitel et al. "Surface plasmon resonance based pesticide assay on a renewable biosensing surface using the reversible concanavalin A monosaccharide interaction". en. In: *Biosensors & bioelectronics* 15.7–8 (2000), 411–415. ISSN: 0956-5663. DOI: 10.1016/s0956-5663(00)00099-3. URL: https://www.sciencedirect.com/science/article/pii/S0956566300000993.

[37] E. Mauriz et al. "Single and multi-analyte surface plasmon resonance assays for simultaneous detection of cholinesterase inhibiting pesticides". en. In: *Sensors and actuators. B, Chemical* 118.1–2 (2006), 399–407. ISSN: 0925-4005. DOI: 10.1016/j.snb.2006.04.085. URL: https://www.sciencedirect.com/science/article/pii/S0925400506003248.

[38] E. Mauriz et al. "Determination of carbaryl in natural water samples by a surface plasmon resonance flow-through immunosensor". en. In: *Biosensors & bioelectronics* 21.11 (2006), 2129–2136. ISSN: 0956-5663. DOI: 10.1016/j.bios.2005.10.013. URL: https://www.sciencedirect.com/science/article/pii/S0956566305003155.

[39] E. Mauriz et al. "Real-time detection of chlorpyrifos at part per trillion levels in ground, surface and drinking water samples by a portable surface plasmon resonance immunosensor". en. In: *Analytica chimica acta* 561.1–2 (2006), 40–47. ISSN: 0003-2670. DOI: 10.1016/j.aca.2005.12.069. URL: https://www.sciencedirect.com/science/article/pii/S0003267006000778.

[40] Li Ping Wu et al. "Visual detection of Sudan dyes based on the plasmon resonance light scattering signals of silver nanoparticles". en. In: *Analytical chemistry* 78.15 (2006), 5570–5577. ISSN: 0003-2700. DOI: 10.1021/ac0603577. URL: http://dx.doi.org/10.1021/ac0603577.

[41] Byung-Keun Oh et al. "Surface plasmon resonance immunosensor using self-assembled protein G for the detection of Salmonella paratyphi". en. In: *Journal of biotechnology* 111.1 (2004), 1–8. ISSN: 0168-1656. DOI: 10.1016/j.jbiotec.2004.02.010. URL: https://www.sciencedirect.com/science/article/pii/S0168165604001099.

[42] J. W. Chung, R. Bernhardt, and J. C. Pyun. "Additive assay of cancer marker CA 19-9 by SPR biosensor". en. In: *Sensors and actuators. B, Chemical* 118.1–2 (2006), 28–32. ISSN: 0925-4005. DOI: 10.1016/j.snb.2006.04.015. URL: https://www.sciencedirect.com/science/article/pii/S0925400506002632.

[43] Jon Ladd et al. "DNA-directed protein immobilization on mixed self-assembled monolayers via a streptavidin bridge". en. In: *Langmuir: the ACS journal of surfaces and colloids* 20.19 (2004), 8090–8095. ISSN: 0743-7463. DOI: 10.1021/la049867r. URL: http://dx.doi.org/10.1021/la049867r.

[44] Yuan Li, Hye Jin Lee, and Robert M. Corn. "Detection of protein biomarkers using RNA aptamer microarrays and enzymatically amplified surface plasmon resonance imaging". en. In: *Analytical chemistry* 79.3 (2007), 1082–1088. ISSN: 0003-2700. DOI: 10.1021/ac061849m. URL: http://dx.doi.org/10.1021/ac061849m.

[45] Geert A. J. Besselink et al. "Signal amplification on planar and gel-type sensor surfaces in surface plasmon resonance-based detection of prostate-specific antigen". en. In: *Analytical biochemistry* 333.1 (2004), 165–173. ISSN: 0003-2697. DOI: 10.1016/j.ab.2004.05.009. URL: https://www.sciencedirect.com/science/article/pii/S0003269704004154.

[46] V. P. Devanarayanan, V. Manjuladevi, and R. K. Gupta. "Surface plasmon resonance sensor based on a new opto-mechanical scanning mechanism". en. In: *Sensors and actuators. B, Chemical* 227 (2016), 643–648. ISSN: 0925-4005. DOI: 10.1016/j.snb.2016.01.027. URL: https://www.sciencedirect.com/science/article/pii/S0925400516300272.

[47] J. Arnoud Marquart. "Chapter 4. SPRpages – getting a feeling for the curves". In: *Handbook of Surface Plasmon Resonance*. Cambridge: Royal Society of Chemistry, 2017, 106–148. ISBN: 9781782627302.

[48] Stella M. Marinakos et al. "Gold particles as templates for the synthesis of hollow polymer capsules. Control of capsule dimensions and guest encapsulation". en. In: *Journal of the American Chemical Society* 121.37 (1999), 8518–8522. ISSN: 0002-7863. DOI: 10.1021/ja990945k. URL: http://dx.doi.org/10.1021/ja990945k.

[49] Jong Seol Yuk, Ernest F. Guignon, and Michael A. Lynes. "Highly sensitive grating coupler-based surface plasmon-coupled emission (SPCE) biosensor for immunoassay". en. In: *The Analyst* 138.9 (2013), 2576–2582. ISSN: 0003-2654. DOI: 10.1039/c3an00135k. URL: https://pubs.rsc.org/en/content/articlelanding/2013/an/c3an00135k.

[50] Jong Seol Yuk, Ernest F. Guignon, and Michael A. Lynes. "Sensitivity enhancement of a grating-based surface plasmon-coupled emission (SPCE) bionsor chip using gold thickness". en. In: *Chemical physics letters* 591 (2014), 5–9. ISSN: 0009-2614. DOI: 10.1016/j.cplett.2013.10.081. URL: https://www.sciencedirect.com/science/article/pii/S0009261413013614.

[51] Powered by Oz Robotics. *Comprehensive Guide for Nanocoatings Technology. Volume 1: Deposition and Mechanism – Nova Science Publishers*. URL: https://novapublishers.com/shop/comprehensive-guide-for-nanocoatings-technology-volume-1-deposition-and-mechanism/.

[52] V. Manjuladevi and Raj Kumar Gupta. "14 Ultrathin films of nanomaterials: a lyotropic liquid crystalline system and its sensing application". In: *Unconventional Liquid Crystals and Their Applications*. De Gruyter, 2021, 503–528. ISBN: 9783110584370.

[53] Ashutosh Joshi et al. "Modulating surface plasmon resonance response by an external electromagnetic wave". In: *EPL (Europhysics Letters)* 133.6 (2021), p. 67005. ISSN: 0295-5075. DOI: 10.1209/0295-5075/133/67005. URL: https://iopscience.iop.org/article/10.1209/0295-5075/133/67005/meta.

[54] Hun. Choi. *Advantages of Photodiode Array*. 2003. URL: https://zombiedoc.com/advantages-of-photodiode-array.html.

[55] David S. Kliger et al. "Polarized light in optics and spectroscopy". In: *Physics today* 44.10 (1991), 117–118. ISSN: 0031-9228. DOI: 10.1063/1.2810294. URL: http://dx.doi.org/10.1063/1.2810294.

[56] N. K. Quang, N. P. Q. Anh, and H. C. Hieu. "A simple simulation of surface plasmon resonance in the Kretschmann configuration using Google Sheets". In: *Jurnal pendidikan fisika Indonesia* 16.2 (2020), 83–91. ISSN: 1693-1246. DOI: 10.15294/jpfi.v16i2.24753. URL: https://journal.unnes.ac.id/nju/index.php/JPFI/article/view/24753.

[57] Caide Xiao. *Super Optical Biosensors*. London, England: Institute of Physics Publishing, 2019. ISBN: 9780750323840. DOI: 10.1088/2053-2563/ab0823. URL: https://iopscience.iop.org/book/mono/978-0-7503-2384-0.pdf.

[58] Yijun Tang, Xiangqun Zeng, and Jennifer Liang. "Surface plasmon resonance: An introduction to a surface spectroscopy technique". en. In: *Journal of chemical education* 87.7 (2010), 742–746. ISSN: 0021-9584. DOI: 10.1021/ed100186y. URL: http://dx.doi.org/10.1021/ed100186y.

[59] Carl F. Snyder and Albert T. Hattenburg. *Refractive Indices and Densities of Aqueous Solutions of Invert Sugar*. en. 1963.

[60] Yen-Liang Yeh. "Real-time measurement of glucose concentration and average refractive index using a laser interferometer". en. In: *Optics and lasers in engineering* 46.9 (2008), 666–670. ISSN: 0143-8166. DOI: 10.1016/j.optlaseng.2008.04.008. URL: https://www.sciencedirect.com/science/article/pii/S0143816608000742.

[61] Eiji Yashima et al. "Supramolecular helical systems: Helical assemblies of small molecules, foldamers, and polymers with chiral amplification and their functions". en. In: *Chemical reviews* 116.22 (2016), 13752–13990. ISSN: 0009-2665. DOI: 10.1021/acs.chemrev.6b00354. URL: http://dx.doi.org/10.1021/acs.chemrev.6b00354.

[62] J. V. Selinger and J. M. Schnur. "Theory of chiral lipid tubules". en. In: *Physical review letters* 71.24 (1993), 4091–4094. ISSN: 0031-9007. DOI: 10.1103/PhysRevLett.71.4091. URL: http://dx.doi.org/10.1103/PhysRevLett.71.4091.

[63] P. Terech et al. "Self-assembled monodisperse steroid nanotubes in water". en. In: *Advanced materials (Deerfield Beach, Fla.)* 14.7 (2002), 495–498. ISSN: 0935-9648. DOI: 10.1002/1521-4095(20020404)14:7<495::aid-adma495>3.0.co;2-9. URL: http://dx.doi.org/10.1002/1521-4095(20020404)14:7<495::aid-adma495>3.0.co;2-9.

[64] L. J. Prins et al. "Chiral exciton coupling of merocyanine dyes within a well defined hydrogen-bonded assembly". en. In: *Proceedings of the National Academy of Sciences of the United States of America* 98.18 (2001), 10042–10045. ISSN: 0027-8424. DOI: 10.1073/pnas.171131398. URL: http://dx.doi.org/10.1073/pnas.171131398.

[65] Thomas Gibaud et al. "Reconfigurable self-assembly through chiral control of interfacial tension". en. In: *Nature* 481.7381 (2012), 348–351. ISSN: 0028-0836. DOI: 10.1038/nature10769. URL: https://www.nature.com/articles/nature10769.

[66] A. B. Harris, Randall D. Kamien, and T. C. Lubensky. "Molecular chirality and chiral parameters". In: *Reviews of modern physics* 71.5 (1999), 1745–1757. ISSN: 0034-6861. DOI: 10.1103/revmodphys.71.1745. URL: http://dx.doi.org/10.1103/revmodphys.71.1745.

[67] R. Oda et al. "Tuning bilayer twist using chiral counterions". en. In: *Nature* 399.6736 (1999), 566–569. ISSN: 0028-0836. DOI: 10.1038/21154. URL: https://www.nature.com/articles/21154.

[68] Randall D. Kamien and Jonathan V. Selinger. "Order and frustration in chiral liquid crystals". In: *Journal of physics. Condensed matter: an Institute of Physics journal* 13.3 (2001), R1–R22. ISSN: 0953-8984. DOI: 10.1088/0953-8984/13/3/201. URL: https://iopscience.iop.org/article/10.1088/0953-8984/13/3/201/meta.

[69] Changjun Park et al. "Homochiral supramolecular thin film from self-assembly of achiral triarylamine molecules by circularly polarized light". en. In: *Molecules (Basel, Switzerland)* 25.2 (2020), p. 402. ISSN: 1420-3049. DOI: 10.3390/molecules25020402. URL: https://www.mdpi.com/1420-3049/25/2/402.

[70] Yusuke Hoshino et al. "Chirality induced by circularly polarized light in liquid crystalline twin dimers with azo linkages". In: *Molecular crystals and liquid crystals* 465.1 (2007), 153–163. ISSN: 1542-1406. DOI: 10.1080/15421400701205735. URL: http://dx.doi.org/10.1080/15421400701205735.

[71] S. G. Cloutier et al. "Measurement of permanent vectorial photoinduced anisotropy in azo-dye-doped photoresist using polarization holography". In: *Journal of Optics A Pure and Applied Optics* 4.6 (2002), S228–S234. ISSN: 1464-4258. DOI: 10.1088/1464-4258/4/6/358. URL: https://iopscience.iop.org/article/10.1088/1464-4258/4/6/358/meta.

[72] Gabriel Iftime et al. "Control of chirality of an azobenzene liquid crystalline polymer with circularly polarized light". en. In: *Journal of the American Chemical Society* 122.51 (2000), 12646–12650. ISSN: 0002-7863. DOI: 10.1021/ja001244m. URL: http://dx.doi.org/10.1021/ja001244m.

[73] Dganit Danino and Yeshayahu Talmon. "Direct-imaging and freeze-fracture cryo-transmission electron microscopy of molecular gels". In: *Molecular Gels*. Berlin/Heidelberg: Springer-Verlag, 2006, 253–274. ISBN: 9781402033520.

[74] Yoshio Shimbo et al. "Ideal liquid crystal display mode using achiral banana-shaped liquid crystals". en. In: *Japanese journal of applied physics (2008)* 45.10 (2006), L282–L284. ISSN: 0021-4922. DOI: 10.1143/jjap.45.l282. URL: https://iopscience.iop.org/article/10.1143/JJAP.45.L282/meta.

[75] Xin Huang et al. "Self-assembled spiral nanoarchitecture and supramolecular chirality in Langmuir-Blodgett films of an achiral amphiphilic barbituric acid". en. In: *Journal of the American Chemical Society* 126.5 (2004), 1322–1323. ISSN: 0002-7863. DOI: 10.1021/ja036878i. URL: http://dx.doi.org/10.1021/ja036878i.

[76] Gregory M. Grason. "Perspective: Geometrically frustrated assemblies". en. In: *The Journal of chemical physics* 145.11 (2016), p. 110901. ISSN: 0021-9606. DOI: 10.1063/1.4962629. URL: http://dx.doi.org/10.1063/1.4962629.

[77] Julien Chopin and Arshad Kudrolli. "Disclinations, e-cones, and their interactions in extensible sheets". en. In: *Soft matter* 12.19 (2016), 4457–4462. ISSN: 1744-683X. DOI: 10.1039/c6sm00187d. URL: https://pubs.rsc.org/en/content/articlelanding/2016/sm/c6sm00187d.

[78] John B. Matson and Samuel I. Stupp. "Self-assembling peptide scaffolds for regenerative medicine". en. In: *Chemical communications (Cambridge, England)* 48.1 (2012), 26–33. ISSN: 1359-7345. DOI: 10.1039/c1cc15551b. URL: https://pubs.rsc.org/en/content/articlelanding/2012/cc/c1cc15551b.

[79] Monika Poonia et al. "Supramolecular assembly of single-walled carbon nanotubes at air-solid interface". en. In: *Journal of nanoparticle research: an interdisciplinary forum for nanoscale science and technology* 16.8 (2014). ISSN: 1388-0764. DOI: 10.1007/s11051-014-2572-2. URL: http://dx.doi.org/10.1007/s11051-014-2572-2.

[80] Yutao Sang and Minghua Liu. "Nanoarchitectonics through supramolecular gelation: formation and switching of diverse nanostructures". en. In: *Molecular systems design & engineering* 4.1 (2019), 11–28. ISSN: 2058-9689. DOI: 10.1039/c8me00068a. URL: https://pubs.rsc.org/en/content/articlelanding/2019/me/c8me00068a.

[81] Sandeep Kumar. *Chemistry of discotic liquid crystals: From monomers to polymers*. Boca Raton, FL: CRC Press, 2010. ISBN: 9781439811450. DOI: 10.1201/b10457. URL: https://api.taylorfrancis.com/content/books/mono/download?identifierName=doi\&identifierValue=10.1201/b10457\&type=googlepdf.

[82] D. R. Vinayakumara, Sandeep Kumar, and Airody Vasudeva Adhikari. "Supramolecular columnar self-assembly of wedge-shaped rhodanine based dyes: Synthesis and optoelectronic properties". en. In: *Journal of molecular liquids* 274 (2019), 215–222. ISSN: 0167-7322. DOI: 10.1016/j.molliq.2018.10.139. URL: https://www.sciencedirect.com/science/article/pii/S0167732218335244.

[83] Balaji Rakesh et al. "Mechanistic understanding of the sensing process by analyzing response curves of TiO2 based humidity sensors". In: *Advances in Natural Sciences Nanoscience and Nanotechnology* 12.4 (2021), p. 045010. ISSN: 2043-6254. DOI: 10.

1088/2043-6262/ac4107. URL: https://iopscience.iop.org/article/10.1088/2043-6262/ac4107/meta.

[84] A. Hazra et al. "Room temperature alcohol sensing by oxygen vacancy controlled TiO2 nanotube array". In: *Applied physics letters* 105.8 (2014), p. 081604. ISSN: 0003-6951. DOI: 10.1063/1.4894008. URL: http://dx.doi.org/10.1063/1.4894008.

[85] Steven Cranford et al. "A single degree of freedom 'lollipop' model for carbon nanotube bundle formation". en. In: *Journal of the mechanics and physics of solids* 58.3 (2010), 409–427. ISSN: 0022-5096. DOI: 10.1016/j.jmps.2009.11.002. URL: https://www.sciencedirect.com/science/article/pii/S0022509609001677.

[86] David R. Nelson. *Defects and geometry in condensed matter physics*. en. Cambridge, England: Cambridge University Press, 2002. ISBN: 9780521004008.

[87] Vianney Gimenez-Pinto et al. "Modeling out-of-plane actuation in thin-film nematic polymer networks: From chiral ribbons to auto-origami boxes via twist and topology". en. In: *Scientific reports* 7.1 (2017), 1–7. ISSN: 2045-2322. DOI: 10.1038/srep45370. URL: https://www.nature.com/articles/srep45370.

[88] R. R. Guimarães et al. "Annihilation dynamics of stringlike topological defects in a nematic lyotropic liquid crystal". en. In: *Journal of physics. Condensed matter: an Institute of Physics journal* 25.40 (2013), p. 404203. ISSN: 0953-8984. DOI: 10.1088/0953-8984/25/40/404203. URL: https://iopscience.iop.org/article/10.1088/0953-8984/25/40/404203/meta.

[89] Dario Cortese, Jens Eggers, and Tanniemola B. Liverpool. "Pair creation, motion, and annihilation of topological defects in two-dimensional nematic liquid crystals". In: *Physical review. E* 97.2 (2018). ISSN: 2470-0053. DOI: 10.1103/physreve.97.022704. URL: http://dx.doi.org/10.1103/physreve.97.022704.

[90] V. P. Devanarayanan et al. "Measurement of optical anisotropy in ultrathin films using surface plasmon resonance". In: *Journal of molecular structure* 1103 (2016), 281–285. ISSN: 0022-2860. DOI: 10.1016/j.molstruc.2015.09.018. URL: https://www.sciencedirect.com/science/article/pii/S0022286015302829.

[91] J. Canning et al. "Water on Au sputtered films". en. In: *Chemical communications (Cambridge, England)* 50.65 (2014), 9172–9175. ISSN: 1359-7345. DOI: 10.1039/c4cc02492c. URL: https://pubs.rsc.org/en/content/articlelanding/2014/cc/c4cc02492c.

[92] F. Wu et al. "Layered material platform for surface plasmon resonance biosensing". en. In: *Scientific reports* 9.1 (2019), p. 20286. ISSN: 2045-2322. DOI: 10.1038/s41598-019-56105-7. URL: https://www.nature.com/articles/s41598-019-56105-7.

[93] Jirí Homola. "Surface plasmon resonance sensors for detection of chemical and biological species". en. In: *Chemical reviews* 108.2 (2008), 462–493. ISSN: 0009-2665. DOI: 10.1021/cr068107d. URL: http://dx.doi.org/10.1021/cr068107d.

[94] Ibrahim Abdulhalim, Mohammad Zourob, and Akhlesh Lakhtakia. "Surface Plasmon Resonance for Biosensing: A Mini-Review". In: *Electromagnetics* 28.3 (2008), 214–242. ISSN: 0272-6343. DOI: 10.1080/02726340801921650. URL: http://dx.doi.org/10.1080/02726340801921650.

[95] Dongping Wang et al. "Recent advances in surface plasmon resonance imaging sensors". en. In: *Sensors (Basel, Switzerland)* 19.6 (2019), p. 1266. ISSN: 1424-8220. DOI: 10.3390/s19061266. URL: https://www.mdpi.com/1424-8220/19/6/1266.

[96] Chi Lok Wong and Malini Olivo. "Surface plasmon resonance imaging sensors: A review". en. In: *Plasmonics (Norwell, Mass.)* 9.4 (2014), 809–824. ISSN: 1557-1955. DOI: 10.1007/s11468-013-9662-3. URL: http://dx.doi.org/10.1007/s11468-013-9662-3.

[97] Andy Chieng et al. "Recent progress in the studies of electrochemical interfaces by surface plasmon resonance spectroscopy and microscopy". en. In: *Current opinion in electrochemistry* 13 (2019), 94–99. ISSN: 2451-9103. DOI: 10.1016/j.coelec.2018.11.002. URL: https://www.sciencedirect.com/science/article/pii/S2451910318301509.

[98] Adrian Blidar et al. "Electrochemical surface plasmon resonance (EC-SPR) aptasensor for ampicillin detection". en. In: *Analytical and bioanalytical chemistry* 411.5 (2019),

1053–1065. ISSN: 1618-2642. DOI: 10.1007/s00216-018-1533-5. URL: http://dx.doi.org/10.1007/s00216-018-1533-5.

[99] Shaopeng Wang et al. "Electrochemical surface plasmon resonance: basic formalism and experimental validation". en. In: *Analytical chemistry* 82.3 (2010), 935–941. ISSN: 0003-2700. DOI: 10.1021/ac902178f. URL: http://dx.doi.org/10.1021/ac902178f.

[100] Amrit Kumar et al. "Surface plasmon resonance for in-plane birefringence measurement of anisotropic thin organic film". en. In: *Plasmonics (Norwell, Mass.)* 16.4 (2021), 1023–1028. ISSN: 1557-1955. DOI: 10.1007/s11468-021-01373-1. URL: http://dx.doi.org/10.1007/s11468-021-01373-1.

[101] Ashutosh Joshi et al. "Morphological transformation in the supramolecular assembly of discotic liquid crystal molecules using silver nanoparticles and its sensing application". en. In: *Nanotechnology* 31.36 (2020), p. 365605. ISSN: 0957-4484. DOI: 10.1088/1361-6528/ab93eb. URL: https://iopscience.iop.org/article/10.1088/1361-6528/ab93eb/meta.

[102] Raj Kumar Gupta and V. Manjuladevi. "Liquid crystals at interfaces". en. In: *Israel journal of chemistry* 52.10 (2012), 809–819. ISSN: 0021-2148. DOI: 10.1002/ijch.201200030. URL: http://dx.doi.org/10.1002/ijch.201200030.

[103] K. Inglot, T. Martyński, and D. Bauman. "Molecular organization and aggregation in Langmuir and Langmuir-Blodgett films of azo dye/liquid crystal mixtures". In: *Opto-Electronics Review* 17.2 (2009), 120–128. ISSN: 1230-3402. DOI: 10.2478/s11772-008-0053-9. URL: https://www.degruyter.com/document/doi/10.2478/s11772-008-0053-9/pdf.

[104] K. A. Suresh and A. Bhattacharyya. "Formation of liquid crystalline phases from a Langmuir monolayer". en. In: *Langmuir: the ACS journal of surfaces and colloids* 13.6 (1997), 1377–1380. ISSN: 0743-7463. DOI: 10.1021/la960574a. URL: http://dx.doi.org/10.1021/la960574a.

[105] Pingsheng He et al. "Elasticity of Langmuir monolayer detected by dynamic oscillation method". en. In: *Colloids and surfaces. A, Physicochemical and engineering aspects*

201.1–3 (2002), 265–273. ISSN: 0927-7757. DOI: 10.1016/s0927-7757(01)01031-7. URL: https://www.sciencedirect.com/science/article/pii/S0927775701010317.

[106] Dominique Langevin and Francisco Monroy. "Interfacial rheology of polyelectrolytes and polymer monolayers at the air–water interface". en. In: *Current opinion in colloid & interface science* 15.4 (2010), 283–293. ISSN: 1359-0294. DOI: 10.1016/j.cocis.2010.02.002. URL: https://www.sciencedirect.com/science/article/pii/S1359029410000282.

[107] Pamarti Viswanath and Masamichi Yoshimura. "Light-induced reversible phase transition in polyvinylidene fluoride-based nanocomposites". en. In: *SN applied sciences* 1.11 (2019). ISSN: 2523-3963. DOI: 10.1007/s42452-019-1564-3. URL: http://dx.doi.org/10.1007/s42452-019-1564-3.

[108] Mohammad Adnan et al. "Real-time dynamic evolution monitoring of laser-induced exciton phase flips in 2D hybrid semiconductor (C12H25NH3)2PbI4". en. In: *Journal of applied physics* 128.2 (2020), p. 023104. ISSN: 0021-8979. DOI: 10.1063/5.0011815. URL: http://dx.doi.org/10.1063/5.0011815.

[109] T. Schultz et al. "Azobenzene photoisomerization: Two states and two relaxation pathways explain the violation of Kasha's rule". In: *Femtochemistry and Femtobiology*. Ed. by Monique M. Martin and James T. Hynes. Elsevier, 2004, 45–48. ISBN: 9780444516565.

[110] Mihir Kumar Purkait et al. *Stimuli responsive polymeric membranes: Volume 25: Smart polymeric membranes*. San Diego, CA: Academic Press, 2018. ISBN: 9780128139615.

[111] Almeria Natansohn and Paul Rochon. "Photoinduced motions in azo-containing polymers". en. In: *Chemical reviews* 102.11 (2002), 4139–4175. ISSN: 0009-2665. DOI: 10.1021/cr970155y. URL: http://dx.doi.org/10.1021/cr970155y.

[112] E. Blasco et al. "Smart polymers for optical data storage". In: *Smart Polymers and their Applications*. Ed. by Maria Rosa Aguilar and Julio San Román. Elsevier, 2019, 567–606. ISBN: 9780081024164.

[113] Henning Menzel. "Photoisomerization in Langmuir-Blodgett-Kuhn Structures". In: *Photoreactive Organic Thin Films*. Ed. by Zouheir Sekkat and Wolfgang Knoll. Elsevier, 2002, 179–218. ISBN: 9780126354904.

[114] Takahiro Seki and Kunihiro Ichimura. "Dynamic photocontrols of molecular organization and motion of materials by two-dimensionally arranged azobenzene assemblies". In: *Photoreactive Organic Thin Films*. Ed. by Zouheir Sekkat and Wolfgang Knoll. Elsevier, 2002, 487–512. ISBN: 9780126354904.

[115] Q. Yu and H. Chen. "Interaction of switchable biomaterials surfaces with proteins". In: *Switchable and Responsive Surfaces and Materials for Biomedical Applications*. Ed. by Zheng Zhang. Elsevier, 2015, 167–188. ISBN: 9780857097132.

[116] Hermann Rau. "Photoisomerization of Azobenzenes". In: *Photoreactive Organic Thin Films*. Ed. by Zouheir Sekkat and Wolfgang Knoll. Elsevier, 2002, 3–47. ISBN: 9780126354904.

[117] Seung-Won Oh et al. "Optical and electrical switching of cholesteric liquid crystals containing azo dye". en. In: *RSC advances* 7.32 (2017), 19497–19501. ISSN: 2046-2069. DOI: 10.1039/c7ra01507k. URL: https://pubs.rsc.org/en/content/articlelanding/2017/ra/c7ra01507k.

[118] Jiaxin Hou et al. "Photo-responsive helical motion by light-driven molecular motors in a liquid-crystal network". en. In: *Angewandte Chemie (International ed. in English)* 60.15 (2021), 8251–8257. ISSN: 1433-7851. DOI: 10.1002/anie.202016254. URL: http://dx.doi.org/10.1002/anie.202016254.

[119] Hongying Liu et al. "Analysis of structural morphological changes from 3DOM V2O5 film to V2O5 nanorods film and its application in electrochromic device". en. In: *Solar energy materials and solar cells: an international journal devoted to photovoltaic, photothermal, and photochemical solar energy conversion* 238.111627 (2022), p. 111627. ISSN: 0927-0248. DOI: 10.1016/j.solmat.2022.111627. URL: https://www.sciencedirect.com/science/article/pii/S0927024822000502.

[120] Somnath S. Kundale et al. "Effects of switching layer morphology on resistive switching behavior: A case study of electrochemically synthesized mixed-phase copper oxide memristive devices". en. In: *Applied materials today* 27.101460 (2022), p. 101460. ISSN:

2352-9407. DOI: 10.1016/j.apmt.2022.101460. URL: https://www.sciencedirect.com/science/article/pii/S2352940722000993.

[121] Michael M. Skolnick. "Application of morphological transformations to the analysis of two-dimensional electrophoretic gels of biological materials". en. In: *Computer vision, graphics, and image processing* 35.3 (1986), 306–332. ISSN: 0734-189X. DOI: 10.1016/0734-189x(86)90003-4. URL: https://www.sciencedirect.com/science/article/pii/0734189X86900034.

[122] Dehui Han et al. "Cyclic azobenzene-containing side-chain liquid crystalline polymers: Synthesis and topological effect on mesophase transition, order, and photoinduced birefringence". en. In: *Macromolecules* 43.8 (2010), 3664–3671. ISSN: 0024-9297. DOI: 10.1021/ma100246c. URL: http://dx.doi.org/10.1021/ma100246c.

[123] B. T. Hogan et al. "2D material liquid crystals for optoelectronics and photonics". en. In: *Journal of materials chemistry. C, Materials for optical and electronic devices* 5.43 (2017), 11185–11195. ISSN: 2050-7526. DOI: 10.1039/c7tc02549a. URL: https://pubs.rsc.org/en/content/articlelanding/2017/tc/c7tc02549a.

[124] Jae Yoon Lee et al. "Two-Dimensional Semiconductor Optoelectronics Based on van der Waals Heterostructures". en. In: *Nanomaterials (Basel, Switzerland)* 6.11 (2016), p. 193. ISSN: 2079-4991. DOI: 10.3390/nano6110193. URL: https://www.mdpi.com/2079-4991/6/11/193.

[125] Xiwei Zhang et al. "A review on optoelectronic device applications of 2D transition metal carbides and nitrides". en. In: *Materials & design* 200.109452 (2021), p. 109452. ISSN: 0264-1275. DOI: 10.1016/j.matdes.2021.109452. URL: https://www.sciencedirect.com/science/article/pii/S0264127521000058.

[126] Zhixiang Gao et al. "An A-D-A type of thiophene derivative with morphology-determining luminescent performance: Synthesis and application in a light emitting device". en. In: *Journal of luminescence* 219.116919 (2020), p. 116919. ISSN: 0022-2313. DOI: 10.1016/j.jlumin.2019.116919. URL: https://www.sciencedirect.com/science/article/pii/S0022231319319453.

[127] Parul Taneja et al. "Heavy metal ion sensing using ultrathin Langmuir–Schaefer film of tetraphenylporphyrin molecule". In: *IEEE sensors journal* 20.7 (2020), 3442–3451. ISSN: 1530-437X. DOI: 10.1109/jsen.2019.2959488. URL: https://ieeexplore.ieee.org/document/8932539.

[128] Parul Taneja et al. "Facile ultrathin film of silver nanoparticles for bacteria sensing". en. In: *Colloids and surfaces. B, Biointerfaces* 196.111335 (2020), p. 111335. ISSN: 0927-7765. DOI: 10.1016/j.colsurfb.2020.111335. URL: https://www.sciencedirect.com/science/article/pii/S0927776520306913.

[129] *Langmuir-Blodgett Films*. Boston, MA: Springer US, 1990. ISBN: 9781489937186.

[130] Chen Fang et al. "Recent applications of Langmuir-Blodgett technique in battery research". en. In: *ACS applied materials & interfaces* 14.2 (2022), 2431–2439. ISSN: 1944-8244. DOI: 10.1021/acsami.1c19064. URL: http://dx.doi.org/10.1021/acsami.1c19064.

[131] Jr Oliveira Osvaldo N., Luciano Caseli, and Katsuhiko Ariga. "The past and the future of Langmuir and Langmuir-Blodgett films". en. In: *Chemical reviews* 122.6 (2022), 6459–6513. ISSN: 0009-2665. DOI: 10.1021/acs.chemrev.1c00754. URL: http://dx.doi.org/10.1021/acs.chemrev.1c00754.

[132] Amrit Kumar et al. "Surface plasmon resonance for in-plane birefringence measurement of anisotropic thin organic film". en. In: *Plasmonics (Norwell, Mass.)* 16.4 (2021), 1023–1028. ISSN: 1557-1955. DOI: 10.1007/s11468-021-01373-1. URL: http://dx.doi.org/10.1007/s11468-021-01373-1.

[133] Ashutosh Joshi et al. "Modulating surface plasmon resonance response by an external electromagnetic wave". In: *EPL (Europhysics Letters)* 133.6 (2021), p. 67005. ISSN: 0295-5075. DOI: 10.1209/0295-5075/133/67005. URL: https://iopscience.iop.org/article/10.1209/0295-5075/133/67005/meta.

[134] Anna Modlińska et al. "Influence of the molecular structure of thermotropic liquid crystals on their ability to form monolayers at interface". en. In: *Liquid crystals* 36.2 (2009), 197–208. ISSN: 0267-8292. DOI: 10.1080/02678290902759236. URL: http://dx.doi.org/10.1080/02678290902759236.

[135] R. K. Gupta et al. "Thin films of discotic liquid crystals and their applications". en. In: *Liquid crystals* 43.13–15 (2016), 2079–2091. ISSN: 0267-8292. DOI: 10.1080/02678292.2016.1195454. URL: http://dx.doi.org/10.1080/02678292.2016.1195454.

[136] Keerti Choudhary et al. "Alignment of liquid crystals using Langmuir–Blodgett films of unsymmetrical bent-core liquid crystals". en. In: *Liquid crystals* 46.10 (2019), 1494–1504. ISSN: 0267-8292. DOI: 10.1080/02678292.2019.1574035. URL: http://dx.doi.org/10.1080/02678292.2019.1574035.

[137] Atsushi Yoshizawa. "Unconventional liquid crystal oligomers with a hierarchical structure". In: *Journal of Materials Chemistry* 18.25 (2008), 2877–2889. ISSN: 1364-5501. DOI: 10.1039/B802712A. URL: https://pubs.rsc.org/en/content/articlelanding/2008/jm/b802712a.

[138] Masanari Okuno et al. "Correction to "symmetric Raman tensor contributes to chiral vibrational sum frequency generation from binaphthyl amphiphile monolayers on water: Study of electronic resonance amplitude and phase profiles"". en. In: *The journal of physical chemistry. C, Nanomaterials and interfaces* 125.45 (2021), 25356–25356. ISSN: 1932-7447. DOI: 10.1021/acs.jpcc.1c09228. URL: http://dx.doi.org/10.1021/acs.jpcc.1c09228.

[139] Jan Holec et al. "Chirality-controlled self-assembly of amphiphilic dibenzo[6]helicenes into Langmuir-Blodgett thin films". en. In: *Chemistry (Weinheim an der Bergstrasse, Germany)* 25.49 (2019), 11494–11502. ISSN: 0947-6539. DOI: 10.1002/chem.201901695. URL: http://dx.doi.org/10.1002/chem.201901695.

[140] J. A. Zasadzinski et al. "Langmuir-Blodgett films". en. In: *Science (New York, N.Y.)* 263.5154 (1994), 1726–1733. ISSN: 0036-8075. DOI: 10.1126/science.8134836. URL: https://www.science.org/doi/10.1126/science.8134836.

[141] V. P. Devanarayanan, V. Manjuladevi, and R. K. Gupta. "Surface plasmon resonance sensor based on a new opto-mechanical scanning mechanism". en. In: *Sensors and actuators. B, Chemical* 227 (2016), 643–648. ISSN: 0925-4005. DOI: 10.1016/j.snb.2016.01.027. URL: https://www.sciencedirect.com/science/article/pii/S0925400516300272.

[142] Jr Oliveira Osvaldo N., Maria Raposo, and Anantharaman Dhanabalan. "Langmuir-Blodgett and self-assembled polymeric films". In: *Handbook of Surfaces and Interfaces of Materials*. Ed. by Hari Singh Nalwa. Elsevier, 2001, 1–63. ISBN: 9780125139106.

[143] E. Heydari, E. Mohajerani, and A. Shams. "All optical switching in azo-polymer planar waveguide". en. In: *Optics communications* 284.5 (2011), 1208–1212. ISSN: 0030-4018. DOI: 10.1016/j.optcom.2010.10.096. URL: https://www.sciencedirect.com/science/article/pii/S0030401810012101.

[144] V. P. Devanarayanan et al. "Measurement of optical anisotropy in ultrathin films using surface plasmon resonance". In: *Journal of molecular structure* 1103 (2016), 281–285. ISSN: 0022-2860. DOI: 10.1016/j.molstruc.2015.09.018. URL: https://www.sciencedirect.com/science/article/pii/S0022286015302829.

[145] Kazuyoshi Kurihara, Kaori Nakamura, and Koji Suzuki. "Asymmetric SPR sensor response curve-fitting equation for the accurate determination of SPR resonance angle". en. In: *Sensors and actuators. B, Chemical* 86.1 (2002), 49–57. ISSN: 0925-4005. DOI: 10.1016/s0925-4005(02)00146-6. URL: https://www.sciencedirect.com/science/article/pii/S0925400502001466.

[146] L. Torsi et al. "Multi-parameter gas sensors based on organic thin-film-transistors". en. In: *Sensors and actuators. B, Chemical* 67.3 (2000), 312–316. ISSN: 0925-4005. DOI: 10.1016/s0925-4005(00)00541-4. URL: https://www.sciencedirect.com/science/article/pii/S0925400500005414.

[147] Bo Zhou et al. "Fabrication of a miniature multi-parameter sensor chip for water quality assessment". In: *Sensors (Basel, Switzerland)* 17.12 (2017), p. 157. ISSN: 1424-8220. DOI: 10.3390/s17010157. URL: https://www.mdpi.com/1424-8220/17/1/157.

[148] Diclehan Karakaya, Oguzhan Ulucan, and Mehmet Turkan. "Electronic nose and its applications: A survey". en. In: *International journal of automation and computing* 17.2 (2020), 179–209. ISSN: 1476-8186. DOI: 10.1007/s11633-019-1212-9. URL: http://dx.doi.org/10.1007/s11633-019-1212-9.

[149] Miquel-Angel Amer et al. "Multichannel QCM-based system for continuous monitoring of bacterial biofilm growth". In: *IEEE transactions on instrumentation and measurement* 69.6 (2020), 2982–2995. ISSN: 0018-9456. DOI: 10.1109/tim.2019.2929280. URL: https://ieeexplore.ieee.org/document/8765365.

[150] Liqiu Men, Ping Lu, and Qiying Chen. "Intelligent multiparameter sensing with fiber Bragg gratings". In: *Applied physics letters* 93.7 (2008), p. 071110. ISSN: 0003-6951. DOI: 10.1063/1.2975186. URL: http://dx.doi.org/10.1063/1.2975186.

List of Publications

International Journals

1. Joshi, Ashutosh, Akash Gayakwad, V. Manjuladevi, Mahesh C. Varia, S. Kumar, and R. K. Gupta. 2022. "Photoinduced Modulation of Refractive Index in Langmuir-Blodgett Films of Azo-Based H-Shaped Liquid Crystal Molecules." Journal of Molecular Liquids 364 (120071): 120071. https://doi.org/10.1016/j.molliq.2022.120071

2. Joshi, A., Kumar, A., Manjuladevi, & Gupta, R. K. (2021). Modulating surface plasmon resonance response by an external electromagnetic wave. EPL (Europhysics Letters), 133(6), 67005. https://doi.org/10.1209/0295-5075/133/67005

3. Kumar, A., Gupta, R. K., Manjuladevi, & Joshi, A. (2021). Surface plasmon resonance for in-plane birefringence measurement of anisotropic thin organic film. Plasmonics (Norwell, Mass.), 16(4), 1023–1028. https://doi.org/10.1007/s11468-021-01373-1

4. Joshi, A., Manjuladevi, V., Gupta, R. K., & Kumar, S. (2020). Morphological transformation in the supramolecular assembly of discotic liquid crystal molecules using silver nanoparticles and its sensing application. Nanotechnology, 31(36), 365605. https://doi.org/10.1088/1361-6528/ab93eb

International Conference Proceedings

1. Joshi, A., Manjuladevi, V., & Kumar Gupta, R. (2022). Facile layered structure of sensing chip of a prism–based surface plasmon resonance device. Materials Today: Proceedings, 63, 647–652. https://doi.org/10.1016/j.matpr.2022.04.723

2. Joshi, A., Manjuladevi, V., Gupta, R. K., & Kumar, S. (2021). Nanoribbons of discotic liquid crystal molecules. Materials Today: Proceedings, 46, 5866–5869. https://doi.org/10.1016/j.m

Book Chapter

1. "Electrochemical surface plasmon resonance for efficient sensing", CRC press, Taylor & Francis Group, 2022. (Under process)

List of Conferences/Workshop Participated

International Conferences

1. "Nanofibers Of Triphenylene Based Discotic Liquid Crystals", 3rd International Conference on Soft Materials, MNIT, Jaipur, 9-14 December 2018.

2. "Surface Plasmon Resonance of Ultrathin Films of Nematic Liquid Crystal Molecules", International Conference on Liquid Crystals, Liquid Crystalline Polymers and Nanosystems (ICLCPN-2019), MG univ., Kottayam, 13-15 December 2019.

3. "Nanoribbons of Discotic Liquid Crystal Molecules", 2nd International Conference on Advances in Materials Science, Communication, and Microelectronics (ICAMCM-2021), JECRC Univ., Jaipur, Feb. 19-20, 2021.

4. "Facile Layered Structure of Sensing Chip Of A Prism–Based Surface Plasmon Resonance Device", 4th International Conference on Advances In Mechanical Engineering And Nanotechnology, Manipal Univ., Jaipur, February 18-19, 2022.

Workshop Participated

1. One Day Workshop on Flexible Electronics Technology (WFET-2018), CSIR-Central Electronics Engineering Research Institute, Pilani, March 23, 2018.

2. The Group of Twenty (G20) International Meetings on Education Amritsar, Panjab, Organized by Indian Institute of Technology, Ropar, Mar. 15-17, 2023.

SPR Equipment Demonstrations & Website Designed

SPR Equipment Demonstrations

1. Demonstrated before the Scientific Committee of the Department of Science Technology - India at IIT-Delhi in 2018.

2. Demonstrated before the Scientific Committee of Raman Research Institute (RRI, Bangalore) in 2019.

3. Demonstrated before the Scientific Committee of Central Electronics Engineering Research Institute (CSIR - CEERI) in 2019.

Website Designed

1. A website "www.sprsensors.org" has been designed to commercialize the developed equipment.

Brief Biography of the Supervisor

Prof. Raj Kumar Gupta is Professor in the Department of Physics at Birla Institute of Technology & Science Pilani, Pilani Campus. He received his Ph.D. degree from Raman Research Institute, Bengaluru in soft condensed matter physics in the year of 2005. He joined Physics Department of BITS Pilani, Pilani Campus in August 2005. He was head of the physics department from 2018-2020. Currently, he is Associate Dean of sponsored research and Consultancy Division at BITS-Pilani campus.

Prof. R. K. Gupta is an experimental soft condensed matter physicist. He works in the field of thin films of mesogenic molecules, nanomaterials, and composites. Currently, his research interests are focused on understanding the change in properties of materials in the ultrathin film regime and their sensing application. He and his team have developed a low-cost portable surface plasmon resonance (SPR) instrument with the financial support from DST, India. An Indian patent application is in progress for this instrument. The developed SPR instrument is employed for exploring science at low-dimensional system and sensing applications. Prof. Gupta has published more than 60 research articles in international journals of repute. He has executed several sponsored research projects. He is an active reviewer for several high impact international journals of his research field.

Brief Biography of the Candidate

Ashutosh Joshi (B. Tech in Electronics and Communication) completed his Masters (M. Tech) in Nanotechnology (Electro-Mechanical) from Rajasthan Technical University in 2016 with a certified research work from IIT-Indore and joined BITS Pilani as junior research fellow in a DST sponsored project of Prof. R. K. Gupta. He joined the Ph. D. program of BITS-Pilani in 2017 under the supervision of Prof. R. K. Gupta.

Under the supervision of Prof. Raj Kumar Gupta, he has developed a low cost, highly sensitive, optoelectronic SPR sensor under an instrument development program sponsored by DST-India. It has strong potential as a sensor in research as well as in industries. This multipurpose tool has been demonstrated in some well-known scientific institutes and will be commercialized soon. He has published several research articles demonstrating the applications of the SPR equipment using nanofibers, liquid crystals, nanoparticles, quantum dots etc. in international journals of repute. Under the precious supervision of Prof. R. K. Gupta has developed a standalone handheld SPR instrument for sensing on-site applications.